2017

# Molecular Dynamics Studies on dynamic wetting, droplet rapid contact line advancement and nanosuspension drop self-pinning phenomenon

Baiou Shi
*Lehigh University*

# Molecular Dynamics Studies on dynamic wetting, droplet rapid contact line advancement and nanosuspension drop self-pinning phenomenon

by

Baiou Shi

A Dissertation

Presented to the Graduate and Research Committee

of Lehigh University

in Candidacy for the Degree of

Doctor of Philosophy

in

Mechanical Engineering

Lehigh University

May, 2017

# DISSERTATION SIGNATURE SHEET

Approved and recommended for acceptance as a dissertation in partial fulfillment of the requirements for the degree of Doctor of Philosophy

Baiou Shi
Molecular Dynamics Studies on dynamic wetting, droplet rapid contact line advancement and nanosuspension drop self-pinning phenomenon

_____

Date

_____
Edmund B. Webb III
Dissertation Director

_____

Approved Date

Committee Members:

_____
Edmund B. Webb III

_____
Jacob Y. Kazakia

_____
Philip A. Blythe

_____
John N. Dupont

ACKNOWLEDGEMENTS

First, I would like to express my appreciation to the faculty members and staff of the Department of Mechanical Engineering and Mechanics. The faculty members have given me the tools with which to pursue my career in engineering. I would also like to thank the staff in our department office, and all those who have offered me kind help during my study and living in Lehigh University.

My deepest appreciation goes to Dr. Edmund B. Webb III, my Ph.D. advisor, for introducing me to the field of my PhD study. None of my accomplishments could ever be made without his continuous support, inspiration, encouragement and guidance during my years at Lehigh.

Sincere thanks are extended to my committee members, Dr. Jacob Kazakia, Dr. Philip Blythe, and Dr. John DuPont. Thank you for your time, encouragement, valuable advices, and wonderful classes you gave. Any problems or difficulties I met, you were always there with thoughtful discussion, insightful comments and suggestions.

There are many special people I wish I could be able to put their names in here. Those are Lehigh HPC staffs, who trained me how to run parallel computing on the clusters; Professor Charles Smith and Arkady Voloshin, who shared with me lots of teaching experience when I served as a teaching assistant; my colleagues in the laboratory including Dr. Murat Al, Dr. Christopher Shumeyko, Dr. Nipun Goel, Mr. Yibo Wang, Mr. Wei Wei, Mr. Michael Morabito, Mr. Weizhou Zhou, Ms. Chuqiao Dong, whom I have been fortunate to work with and my research would not have been so smooth without their helps. And of course, all my dear friends I met at Lehigh, with whom I had many unforgettable memories.

I would also like to thank my parents for having brought me up. They were

always supporting me and encouraging me with their unconditional love.

TABLE OF CONTENTS

# LIST OF FIGURES

# ABSTRACT

Droplet wetting and spreading across a solid substrate is a fascinating fluid mechanics phenomenon. Recently, the behavior of nano-fluids, or fluid suspensions containing nanoparticles, has garnered tremendous attention for applications in advanced manufacturing. Despite previous contributions, much remains to be understood about the wetting and spreading of nano-suspension drops especially on the fundamental mechanisms involved in the spreading process. However, due to the rapid contact line advancement and nano-scale droplet size, both experiments and continuum scale simulations could not provide ways to resolve the problem. Here, we use the fundamental time and length scale classical molecular dynamics to reveal the atomistic scale details about interfacial thermodynamics and associated forces during droplet wetting and spreading, i.e. to explore the related thermo-physical phenomena associated with capillary flow.

The first interest in my dissertation is to study the mechanisms of rapid contact line advance during the early stage of droplet spreading, i.e. the inertial regime spreading. Inertial regime spreading occurs at the earliest moment immediately following contact between a droplet and solid surface. It is at this point when a drop is most out of equilibrium and therefore experiences the highest capillary forces. For low viscosity

liquids with high wettability, high contact line velocities are observed during this stage. Meanwhile, much remains unknown about mechanisms governing such rapid capillary flow during this stage; additionally, because the very leading edge of an advancing contact line is of vanishing physical size, it is expected that phenomena controlling wetting kinetics are atomic scale in nature. In my work, molecular dynamics simulations on metallic Pb-Cu systems were performed to study the early stage spreading. A counterintuitive result from our MD simulations is that even nanometer scale metallic drops exhibit a regime of wetting that is dictated by inertial effects. Therefore, mechanisms observed in atomic simulations may provide insight to corresponding mechanisms for inertial regime spreading of macro-scale droplets. We introduce a Tolman length corrected surface tension to account for liquid/vapor interface curvature effects that manifest in small drops. In addition, for inertial spreading on low advancing contact angle surface, a second nanoscale effect is observed which is unique to this surface and related to curvature gradients along a significant portion of the liquid/vapor interface. After accounting for all the nanoscale size effects, data from inertial spreading of nanodrops could be well described by continuum inertial wetting theory.

Additionally, we explore the fundamental mechanisms in controlling the rapid contact line advancement during the inertial spreading. It is demonstrated that high contact line velocity is abetted by structural ordering of a liquid layer adjacent to the solid. Meanwhile, a tensile strain in this layer, which is most pronounced nearest to the contact line, may also play a role.

For the second interest of my dissertation, wetting and spreading of nano-suspension drops are investigated using the same metallic system. The concept of assembling ordered arrays of nanoparticles on a substrate surface via suspension droplet wetting and subsequent evaporation has fueled a large body of research in this area. Self-pinning is a phenomenon intrinsic to the advancement or retraction of liquid/solid/vapor three-phase contact lines for nano-fluid droplets; in such cases, particles entrained to the contact line halt its motion, preventing the system from reaching equilibrium. Depending on the desired application, this can be either detrimental (e.g. preventing complete coating of a substrate by the suspension) or beneficial (e.g. stabilizing non-equilibrium droplet morphologies). Another relevant phenomenon is de-pinning, where an initially halted contact line is able to separate from the pinning particle and continue its advance (or retraction) across the surface. While deterministic engineering of nanoparticle distribution requires thorough understanding of the thermodynamics and associated wetting kinetics of nanosuspension droplets, quantitative understanding of forces acting on suspended nanoparticles is needed; however, such measurements remain experimentally inaccessible. Herein, we present results from molecular dynamics simulations of nanosuspension droplets spreading on solid surfaces, with emphasis on revealing forces on suspended particles.

For a wetting system of identical liquid, solid and particle chemistry yet significant difference in advancing contact angles, self-pinning is observed for low $\theta_{adv}$ Cu(111) whereas de-pinning occurs at high $\theta_{adv}$ Cu(001). The role of contact angle in determining likelihood for self-pinning is investigated on fundamental time and length

scales. Meanwhile, relations between contact line velocity and advancing contact angle are discussed from atomic scale computation results. For the pinning case, the precursor film is observed to be continually advance across the surface even when the droplet is pinned. However a single layer of liquid on the outer facet of the particle surfaces is observed which manifests a rate limiting step for the precursor film advance. For the de-pinning case, we examine the contact line region carefully during de-pinning, especially the fluid flow profile, advancing contact angle and droplet morphology. Furthermore, forces associated with such behaviors are presented. We found that significant forces in the direction normal to the substrate surface due to liquid atoms confined between the particles and substrate dominate the forces on nanoparticles such that forces are interface dominated.

To advance this work, the roles of particle size, particle loading and interaction strength between particle and substrate are examined. Results presented illustrate how particle size and loading affect spreading kinetics and how this connects to dynamic droplet morphology and relevant forces that exist nearby the contact line region. Increased particle size in simulations permits a more detailed investigation of particle/substrate interfacial contributions to behavior observed at the advancing contact line. A transition from de-pinning to pinning is observed and interpreted in terms of the increasing capillary force between suspended nanoparticles and the solid/liquid/vapor interfaces. At higher nanoparticle concentrations, particle pile up occurs and particle/particle interactions become relevant, leading to pinning and non-equilibrium droplet morphology. By tuning down the interaction strength between particle and

substrate, particle is not able to form strong bonds with the underlying substrate, thus contact line pinning does not occur in this case.

In concluding, MD simulations reveal fundamental mechanisms of inertial spreading related to particle-free drops as well as suspension droplet behavior. Thermodynamic parameters controlling observed kinetics are elucidated. The implications of results presented are discussed. We also address those features in LAMMPS that permit relatively straightforward extraction of forces on suspended particles during suspension droplet wetting simulations. We finally highlight how results such as those herein can help improve the predictive capability of continuum-scale computational methods typically used to model particle suspension droplet behavior and thus ultimately benefit related engineering practices.

# 1 Introduction

## 1.1 Motivation and Justification

Capillary flow as embodied by droplet wetting and spreading is very common in our nature. One may be curious about how do those large trees such as the redwoods in California get water from? It is actually capillary which drives sap all the way up to the top and provides nutrients which are necessary to the redwoods. In a rainy day, when rainwater strikes a puddle, we could usually observe a so-called cat's paws patterns (i.e. the small ripples on the puddle surface); those small ripples are capillary waves, their dynamics are dominated by the effects of surface tension. Capillary is also beneficial for desert animals. For example, the thorny devil, a tiny highly specialized lizard found on the central Australian desert, uses a fascinating application of capillary rise to stay alive in extremely dry conditions. It is covered by grooved thorns, somewhat like rose thorns. During cold nights, dew condenses on the grooves and is drawn by capillary action along the grooves and eventually down to the tiny creature's mouth from where it's able to drink.

Capillary fluid flow is also ubiquitous in technological and industrial fields. Many practical processes require the spreading of a liquid on a solid. The liquid may be a paint, a lubricant, an ink, or a dye. The solid may either show a simple surface or be finely divided (suspensions, porous media, fibers). [1] Indeed, wetting and spreading are of key importance for many applications. At large scales, wetting plays an important role in oil recovery and the efficient deposition of pesticides on plant leaves and the cooling of

industrial reactors. On a smaller scale, wetting solutions have been proposed to solve technological problems in microfluidics, surface cleansing, inkjet printing, and particle self-assembly on surfaces via deposition/evaporation techniques, etc. [2]

There are industry interests in solid/liquid metal systems. Metallic droplet spreading is a process germane to multiple technological pursuits including high temperature joining processes (welding, soldering, and brazing), thermal spray coating deposition, adhesive coating application [3]; furthermore, metallurgists pay lots of attention on capillary effect in such systems, including liquid metal with solid metal particles. For instance, they try to examine incomplete melting and impurities which can lead to solid particles suspended in spreading liquids [4].

Liquid drops on solid surfaces have garnered tremendous attention for over two centuries as shown by those applications above, owing to their ubiquity in both nature and technology. While studies has been done during the later stage of spreading, much remains unknown about mechanisms governing capillary flow rate during the earliest stages of wetting when a drop first contacts a solid surface; furthermore, if solid particles are introduced to a spreading drop, underlying physics would become more complex. Therefore, I'm interested to examine capillary flow phenomenon during my PhD study. I believe that if we could know more about the physics and underlying mechanism of capillary flow, it will not only help us understand nature but also be beneficial on making personal care products and amazing devices in manufacturing industry.

Let us consider a droplet spreads on a solid surface at the earliest time. Because the very leading edge of an advancing contact line is of vanishing physical size, it is

expected that phenomena controlling wetting kinetics are atomic scale in nature. Thus, revealing governing mechanisms for capillary flow of wetting and spreading droplets is an activity well suited to the atomic scale simulations.

In my research, I focus on utilizing fundamental length and time scale atomistic simulations (molecular dynamics) to explore thermo-physical phenomena associated with capillary driven fluid flow, or droplet wetting and spreading in high melting temperature materials (Pb/Cu metallic systems). Through investigating the pure liquid metal inertial spreading process and the nano-droplet wetting process with suspended nanoparticles, the goal is to reveal the underlying mechanisms of spreading kinetics during the spreading process. In my dissertation, illustrations are shown to tell the difference of spreading behaviors between spreading substrates with distinct crystallographic structures. Results are discussed by analyzing droplet morphology, droplet spreading rate, contact angle, precursor film advancement, nanoparticle transport, flow velocity profile, liquid atomic structure at the s/l interface and some other effects during the inertial regime of spreading. Furthermore, self-pinning and depinning phenomena of advancing contact lines in nanosuspension drop are compared and capillary forces on nanoparticles are computed. Meanwhile, some other effects which could impact the wetting process are also studied, e.g. particle loading, particle size, interaction strengths, etc.

Regarding to droplet wetting and spreading simulations, prior studies have revealed important information about rapid contact line advancement during the inertial regime; however they have not revealed fundamental mechanisms controlling the rate of advance. Additionally, prior work using continuum scale models lacked resolution to

reveal fundamental mechanisms. An alternate path to consider in the modeling of droplet spreading is the use of atomic scale molecular dynamics (MD) simulations. Similar to continuum scale models, the starting (input) atomic configuration in a MD simulation must be specified to mimic a drop of liquid in contact with an underlying solid substrate. In MD simulations, the starting atomic velocities are specified to model the desired system temperature $T$ according to Boltzmann statistics; that is, the average of the velocity distribution is zero and the standard deviation is dictated by $T$. On top of the random velocity distribution, one can apply an impact velocity to the drop if so desired. Lastly, MD simulations require a material model that is description of the atomic interactions (i.e. the potential energy as a function of atomic ensemble).

The fundamental description for atomic interactions is given by the time-dependent Schrödinger equation. Based on how electron wave functions are handled and the approximation methods are employed, various theories to describe the atomic forces and system energy have been developed. For example, Density Function Theory (DFT) approximates the Schrodinger equation from first principles. Thus, it is limited to smaller simulation size and much more computationally intensive than molecule dynamics (MD). In classical MD, electrons are not present explicitly such that they are introduced through the potential energy surface. The potential energy surface is a function of atomic positions only based on the Born-Oppenheimer approximation, where nuclei and electrons are treated separately in a molecule. Then, the potential energy surface (solutions of time-dependent Schrödinger equation within the Born Oppenheimer approximation), in turn, is approximated by an analytic function that gives potential

energy, U, as a function of coordinates. Indeed, identifying a potential function that approximates the actual solution of the Schrödinger equation is a difficult task. Design of the potential function and choice of the parameters in MD is often based on fitting to available experimental data (e.g. equilibrium geometry of stable phases, cohesive energy, elastic moduli, vibrational frequencies, temperatures of the phase transitions, etc). Here, we are using classical molecular dynamics and therefore we must select pre-existing material models (i.e. potentials) or develop our own. An advantage to studying the Pb/Cu system is that potentials describing interactions in this system already exist and, as discussed below, they give very good agreement with experimental observations. The class of interatomic potentials we are using belong to the embedded-atom-method (EAM), which is notable due to the usage of a multi-body interaction, reflective of metallic atomic interactions. Once a set of interatomic potentials is selected, the force is readily computed as a gradient of the potential with respect to the atomic coordinates only and subsequent motion of the atoms is computed by applying Newton's second law to the atomic coordinates, i.e., by treating them classically.

Mentioned earlier, potential validation is necessary against experimental results since experiments are usually relevant to engineering applications. As were predicted from the EAM interatomic potentials shown below, the material properties of our model justified robust comparison with experimental data, which helps validate the simulation models. Pb liquid spreading on Cu solid was modeled in our MD simulations. This system is not technologically relevant to manufacturing industry currently due to recently imposed environmental restriction; however it was used for decades in microelectronic

applications as a component of solder materials. As such, significant experimental data for Pb(l) wetting Cu exists, providing opportunities to validate the chosen material interaction model.

For example, we can consider properties of Pb(l) as predicted by the model and see how well they compare to experiment. **Table 1-1** compares predicted thermodynamic properties of Pb(l) to data from experiments. Note that this atomic interaction model for Pb was not fit to any of the properties tabulated. Given this, the level of agreement is quite satisfactory. The most relevant properties for Cu(s) are $T_m$ and the surface energies for the (001) and (111) surfaces. Though not tabulated, $T = 0$ surface energies are $25 - 30\%$ below experiment and $T_m$ is $\sim 10\%$ below experiment. Finally, the dilute limit enthalpy of mixing predicted by the Pb-Cu atomic interaction model is 4.3% below experiment. Therefore, we have a validated model for a real metallic system (i.e. a simple liquid with relatively high $\gamma$ and low $\mu$) that manifests negligible vapor pressure.

| | **Predicted** | **Experiment** |
|---|---|---|
| **Melting temperature $T_m$** | $623\ K$ | $600.7\ K$ |
| **Liquid/vapor surface tension $\gamma$** | $0.574 \pm 0.038\ J/m^2$ | $0.446\ J/m^2$ [5] |
| **Viscosity $\mu$** | $2 \pm 0.2\ mPa \cdot s$ | $2.697\ mPa \cdot s$ [6] |
| **Density $\rho$** | $10688 \pm 220\ kg/m^3$ | $10672.5\ kg/m^3$ [7] |
| **Equilibrium contact angle $\theta_{eq}$** | $30^\circ$ on Cu(001) @ 700K<br>$20^\circ$ on Cu(111) @ 700K | $40^\circ$ @ 700K |

**Table 1-1:** Predicted versus experimental thermodynamic parameters for Pb liquid phase.

Further validation of our proposed model can be made by comparing to experiments for cases where Pb is deposited on and/or wets Cu surfaces. In agreement with recent experiments, our models show that wetting kinetics differ significantly for Pb(l) drops on Cu(001) versus Cu(111) during the inertial regime. Our model also agrees with experiments in that precursor films of atomic thickness are observed to evolve and spread ahead of the main drop with diffusive-like kinetics ($R(t)\sim t^{1/2}$) on both Cu(001) and Cu(111). Note that $t^{1/2}$ dependence for precursor film advancement is distinct from the $t^{1/2}$ dependence for droplet radius during inertial regime (i.e. early stage) spreading. Mathematically, the coefficients – or prefactors – on the $t^{1/2}$ power laws are different for inertial wetting and precursor film advancement. In fact, precursor films do not become evident until near the end of the inertial regime. As to the wetting geometry, final equilibrium contact angles observed are near $20^{\circ}$ in experiments on polycrystalline Cu samples versus ~ $20^{\circ}$ on Cu(111) and ~ $30^{\circ}$ on Cu(001) in our models.

This material system is quite robust particularly germane to wetting and spreading, which means significantly different inertial spreading kinetics are exhibited for two systems with identical chemistry, providing a unique opportunity to observe the role played by atomic structures at a solid surface in determining wetting kinetics. Additionally, since the driving force for Cu to dissolve into liquid Pb is relatively very small, we could use this model system to examine spreading behaviors in the absence of significant substrate dissolution; this is advantageous because it maintains a fairly planar interface between solid and liquid, simplifying geometric considerations during kinetic analysis.

Additionally, the Pb/Cu system has also been used to explore questions associated with surface self-assembly for one material on top of a dissimilar material. For instance, using scanning tunneling microscopy (STM) measurements, Nagl et al. [14] found the formation of a surface alloy on Cu(001) in the sub-monolayer coverage range although Pb and Cu are immiscible in bulk. In 2001, Plass et al. [15] used time sequential atomic scale imaging via low energy electron microscopy (LEEM) to observe Pb at sub-monolayer coverage on Cu(001) and Cu(111). For Pb on Cu(001), they found that a disordered Pb/Cu surface alloy formed on Cu(001). For Pb on Cu(111), they observed a lead overlayer structure grows during lead deposition at a temperature of 673 K. Our model predictions are in agreement with these experimental observations in that our model predicts an overlayer phase forms on Cu(111) whereas a surface alloy forms on Cu(001). As were summarized above, with a validated material model combined with a robust EAM interatomic potential, MD simulations could then be established by utilizing the MD simulator LAMMPS, which was developed by Sandia National Laboratories at 1995. We thus have a validated fundamental method (classical MD), a validated material model (EAM potentials), and a validated implementation of method and model (LAMMPS).

The Pb/Cu material system exhibits interesting behavior, particularly germane to wetting and spreading; that is, significantly different inertial spreading kinetics are exhibited for two systems with identical chemistry, differing only in the crystallographic surface structure. This provides a unique opportunity to observe the role played by atomic structures at a solid surface in determining wetting kinetics. Additionally, since

the driving force for Cu to dissolve into liquid Pb is relatively very small, we could use this model system to examine spreading behaviors in the absence of significant substrate dissolution; this is advantageous because it maintains a fairly planar interface between solid and liquid, simplifying geometric considerations during kinetic analysis.

It was mentioned above that, in addition to a robust material model and proper implementation of the method, we must establish the correct simulation geometry (i.e. drop on solid surface at time zero) and thermodynamic state point (i.e. pressure P and temperature T). Other than these fundamental ingredients, we do not need to control any other parameters for our simulations. With these inputs, wetting simulations can be performed and, from these, many relevant properties can be directly computed. For example, the full liquid/vapor interface profile can be revealed as a function of time; this means the extent of liquid spread on the surface and the dynamic contact angle can be directly computed. Time dependent flow velocity fields inside a spreading drop, as well as pressure fields and capillary forces, can also be directly computed, and those could not be directly achieved from either continuum scale models or by experimental methods. Fluid properties such as viscosity and surface tension naturally arise from the input atomic interaction models; thus, realistic material models can be used. The unique power of MD simulations is the ability to directly reflect the real magnitude and material properties, observe atomic scale processes associated with contact line advancement and the associated growth of the solid/liquid interface.

In previous studies where atomic scale models were used, results were confounded because simulations were for liquids with high vapor pressure; as such,

significant deposition occurred ahead of the advancing contact line. Such simulations were thus exploring wetting on a surface that was pre-wet by the liquid due to adsorption from the vapor, convoluting mechanisms of rapid capillary flow. High vapor pressure is relevant in some systems so it is surprising that authors of prior atomic scale modeling work did not attempt to extract mechanisms from their data. For example, they did not compute pressure fields inside drops and correlate them to flow velocity fields nor was any attempt made to compute capillary forces in the vicinity of the contact line and associate those forces to the structure of the contact line region (e.g. the advancing contact angle, fluid structure adjacent to the solid surface, and how that structure depends on proximity to the contact line).

For atomic scale MD simulations of droplet wetting, some benefits have been identified for using metallic material models such as the embedded atom method (EAM) [8]. The multibody nature of such atomic interaction models means that simple (monoatomic) liquids can be studied and that they will exhibit negligible vapor pressure. With no vapor phase present (and the corresponding absence of a re-adsorbed wetting layer on the substrate), analyzing mechanisms of contact line advancement and characterizing the morphology of the contact line region are somewhat simplified. Additionally, embedded atom method potentials have been advanced that describe certain metallic systems with very good accuracy, compared to experimental data and density functional theory based calculations. Ideally, results so obtained will help elucidate not only metallic system behavior but also provide generalizations to other material systems.

## 1.2 Early stage spreading

Pioneering work on the behavior of liquid drops on solid surfaces can be traced back more than 200 years to the seminal work of Thomas Young, who established an expression for the equilibrium contact angle θ of a liquid drop on a solid surface based on interfacial energy of the three constituent phases: solid, liquid, and vapor,

$$\gamma_{sg} = \gamma_{sl} + \gamma_{lg}\cos\theta \tag{1-1}$$

where $\gamma_{\alpha\beta}$ means the interfacial energy between phases α and β [18]. Because these terms have units of force per length, it is appropriate to consider them as exerting competing forces on the three phase contact line; thus, a more historic term for liquid/vapor interfacial energy is liquid/vapor surface tension.

Over more than 200 years, much has been revealed about capillary flow and droplet wetting and spreading. Work by Nobel laureate Pierre DeGennes established the role of viscosity in dictating wetting kinetics for drops during later stages of spreading and forged the hydrodynamic capillary theory. This predicts that a droplet's radius grows with time as $R(t) \sim t^{1/10}$ and indeed significant experimental work, particularly on higher viscosity polymer drops, has confirmed this power law kinetic dependence during later stages of droplet spreading.

A liquid droplet spreading across a solid substrate is a fascinating fluid mechanics phenomenon involving the motion of a three phase contact line; indeed, the richness of observed behavior for dynamic contact lines was recently reviewed [9]. When a drop contacts a solid surface, it spontaneously spreads on the surface to achieve the equilibrium contact angle $\theta_0$ for the given liquid/solid/vapor system under exploration. It

has been over 200 years since the seminal work of Young established that $\theta_0$ can be understood in terms of a balance of various surface energy contributions, $\cos\theta_0 = \frac{\gamma_{sv}-\gamma_{sl}}{\gamma_{lv}}$ [10]. Subscripts on interface energy $\gamma$ refer to liquid/vapor, solid/vapor, and solid/liquid interfaces that impinge on the contact line. Much has been revealed about processes associated with contact line motion and morphology, including the driving forces that determine the rate at which a droplet spreads across a surface [1], [2]. Despite a body of research that spans multiple centuries, phenomena germane to capillary fluid flow continue to be revealed while new questions continue to emerge.

One regime that has eluded exploration for many systems is the earliest moments immediately following contact between the drop and solid. It is at this point, regardless of $\theta_0$, when a drop is most out of equilibrium and therefore experiences the highest capillary driving forces. Accordingly, very high contact line velocities often manifest as a drop rapidly distorts from an initially spherical shape with 180 °contact angle to a shape with a significantly reduced contact angle. The most rapid contact line advancement rates during this initial stage are typically observed for low viscosity liquids with $\theta_0$ much less than 90 ° (e.g. water droplets wetting hydrophilic surfaces, metal liquids wetting metallic solids). Dynamics for many liquids during the earliest stage of wetting are sufficiently rapid that, until recently, they have eluded resolution via experiment. However, advances in the temporal resolution available to optical cameras have made possible the exploration of the earliest moments when a liquid drop contacts a solid substrate [11]. Coupled with experiment, advanced simulation capabilities have been valuable in elucidating details of wetting kinetics for rapidly advancing contact lines.

Here, we review recent experimental and computational investigations into the dynamics and mechanisms of contact line motion during the earliest stage of wetting. For many systems, it has been advanced that the dominant dissipation mechanism during this stage of spreading is due to inertia. While other droplet phenomena also involve effects due to inertia (e.g. droplet impact on a surface, forced solid body penetration into a liquid [9]), focus here is on drops contacting solid surfaces with negligible approach velocity and the highly rapid contact line advancement that occurs immediately after contact. An attempt is made to thoroughly review germane experimental and theoretical findings; however, some emphasis is placed on recent atomic scale simulation studies, their agreement with experiments, and the properties of rapid contact line advancement that can be directly computed from such methods. Drops studied via atomic scale methods are necessarily very small (typical maximum droplet sizes in current literature are a few tens of nanometers in starting radius) while experiments typically study millimeter size drops. Thus, a goal here is to advance the premise that mechanisms and properties derived from atomic scale simulation studies of rapid contact line advancement can be usefully extrapolated to help understand kinetics of macroscopic droplets. To augment this, a collection of new atomic scale simulation results are also presented. These are used to emphasize the extensibility of theory describing rapid contact line kinetics across a vast span of droplet length scales; in addition, for situations where deviations are observed, newly presented results elucidate their origin.

In cases where a low viscosity drop rapidly spreads to a final contact angle well below 90◦, experiments, theory, and numerical simulations have demonstrated a regime

at the earliest times of droplet spreading where the extent of the droplet's spread across the surface, R, exhibits a 1/2 power law dependence on time, $R \sim t^{1/2}$ [11]–[19]. This early spreading regime is often followed by a decrease in spreading rate such that $R \sim t^{1/10}$, which is in accord with dynamics governed by viscous effects near the wedge shaped moving contact line (i.e. hydrodynamic wetting theory) [1], [20]–[22]. However, some systems show kinetics during later time spreading that are better described by $R \sim t^{1/7}$; such systems are theorized to reflect spreading controlled by molecular detachment and re-adsorption at the advancing contact line (i.e. molecular-kinetic wetting theory) [23]. Still other systems exhibit later stage wetting behavior that is best described by models that combine hydrodynamic and molecular-kinetic descriptions. Kinetics exhibited at the earliest times after contact between liquid and solid depart significantly from either of these power law descriptions and the corresponding contact line velocities are much higher. The Reynolds number $R_e = \rho v R_0/\mu$ (where $\rho$ is density, $v$ is contact line velocity, $R_0$ is starting drop radius, and $\mu$ is viscosity) for millimeter size drops exhibiting high contact line velocity is sufficiently large to conclude that inertial effects dominate observed kinetics during this regime. Indeed, throughout the literature, descriptions can be found of the inertial regime of spreading. However, it is unclear at first whether early time wetting dynamics for nanoscale drops (e.g. as modeled in atomic scale simulations) can be considered to be subject to inertial effects. This is further addressed below; however, for now, discussion will refer to early stage or early regime kinetics.

For non-reactive wetting systems, an early spreading regime with $R \sim t^{1/2}$ dependence has been seen for relatively low temperature spreading liquids [11]–[19] as well as high temperature spreading [15], [24]. Even for reactive wetting cases where significant substrate dissolution into the spreading liquid occurs, there exists a regime at the earliest times during which chemical reactions are largely suppressed and wetting kinetics exhibit $R \sim t^{1/2}$, independent of spreading behavior at later time [23], [25]. This kinetic law has also been observed for early stage wetting on patterned substrates [18] as well as sufficiently rigid soft substrates [26]. Systems that exhibit early stage wetting kinetics governed by $R \sim t^{1/2}$seem fairly ubiquitous and it has been observed that this power law is reminiscent of wetting kinetics in imbibition geometries [27], [28]. Despite evidence of an universality to this early time spreading power law, experimental and numerical investigations have demonstrated that different power law dependency can be observed based on details about the drop viscosity, substrate wettability, droplet shape and ionicity [13], [18], [27], [29]–[31]. The picture has been more clearly rendered by recognition of the similarity between early regime spreading and droplet coalescence; this results from consideration of the geometry of flow in the two situations, as well as the underlying driving forces for contact line advancement [11], [13], [18], [32]. Recent findings have further clarified that all systems show a very early time regime where spreading kinetics are highly akin to what is observed in liquid drop coalescence: relatively low viscosity drops exhibit $R \sim t^{1/2}$, while, for higher viscosity drops, no single power law is applicable since the computed exponent varies with time [21], [35]. Given that an early stage $R \sim t^{1/2}$ spreading regime is observed for essentially all low

viscosity liquids, understanding fundamental mechanisms that manifest observed behavior during this regime can advance capillary flow theory while also guiding efforts to control spreading kinetics in applications.

Experimental insight has been invaluable in pursuit of understanding early regime spreading dynamics and underlying driving forces; however, experiments and numerical simulations have been a synergistic combination in illuminating how macroscale observed behavior connects to micro and even molecular level phenomena. Modeling efforts to explore early time wetting can be broadly classified into those that do not resolve molecular scale entities of matter, such as level-set and diffuse interface methods [33], as well as phase field [16] and volume of fluid methods [19]. Contrasted to these meso- or macro-scale methods are early stage spreading simulations employing molecular dynamics (MD) methods, which do resolve atomic and/or molecular scale entities [15], [18], [34]–[36]. Indeed, MD simulations illustrating $R \sim t^{1/2}$ kinetics have been presented for a number of molecular systems [37]–[41]; however, it is important to distinguish kinetics of bulk droplets spreading at early times from kinetics of spreading for molecular thickness precursor films that have been observed experimentally [42]–[44] and in simulations [37]–[41]. Though both may be characterized by $R \sim t^{1/2}$ kinetics, associated fluid transport geometries are significantly different such that underlying physical driving forces may be quite distinct. For many systems, the precursor film does not become clearly distinguished from the bulk drop until near the end of the early stage of rapid wetting.

The first class of simulation methods (i.e. meso- or macro-scale models) are capable of simulating droplets with size scales similar to what are explored in experiments, making them very well suited to enhance experimental data interpretation and understand connections to underlying thermodynamic theory. For example, phase field models were advanced to address the earliest time dynamics for rapid spreading systems and it was demonstrated that it is necessary to discard the assumption of local equilibrium at the contact line during regimes of rapid spreading. This manifested inclusion in the phase field formalism of a non-equilibrium term to represent a dissipative process near the contact line [16], [17]. Authors of those works describe the dissipative process as diffusive molecular phenomena necessary for advancement of the contact line; inclusion of the non-equilibrium term permits very satisfactory agreement between phase field models and experiment [29], [30]. Furthermore, it was predicted that molecular diffusion processes near the contact line dominate wetting kinetics during early rapid spreading regimes [17] and that dominance of contact line dissipation over both inertial and viscous dissipation is more pronounced for lower wettability surfaces [29], [30]. Note, though, that these phase field simulations are incapable of elucidating specific mechanisms behind the proposed contact line friction term. It is also notable from that body of work that data for pure water systems collapsed for different drop sizes by assuming only inertial scaling. Indeed, the authors noted a 'non-monotonicity' in the trend of their contact line friction parameter with decreasing wettability for the pure water system that they could not explain [30]. A possible explanation for deviations from theory exhibited by the pure

liquid system is that the contact line friction term may be most relevant for liquid mixtures wherein might exist a molecular scale competition to occupy the contact line during spreading. Physical mechanisms associated with the friction term remain unclear, challenging explanations of observed deviations from theory.

Models that do resolve atomic entities in a spreading liquid (i.e. MD simulations) permit direct observation of molecular scale mechanisms driving contact line advancement and its associated rate. An obvious limitation of such simulations is that the largest droplet sizes typically studied are of order of tens of nanometers. Nonetheless, spreading times are similarly small such that MD simulations are able to track wetting far enough in time to observe vanishing contact angles and late time, slow regime spreading. By exploring early regime wetting via such methods, intimate contact line details have been revealed. For systems that exhibit significant substrate dissolution into the spreading drop, MD simulations revealed that dissolution during the early spreading regime was minimal such that the contact line remained relatively pure in composition while exhibiting $R \sim t^{1/2}$ kinetics [15]. Molecular dynamics simulations for non-reactive systems show that high contact line velocity and concomitant emergence of diffusive contact line motion (i.e. $R \sim t^{1/2}$) can be achieved by reducing the energy barrier between adjacent adsorption sites on a solid surface to of order the thermal energy ($kT$) [35]. Though this was achieved in Ref. [35] by reducing the solid/liquid interaction, it has been shown in separate MD simulations that a sufficient increase in the strength of a long-range solid/liquid interaction drives a transition to spreading with $R \sim t^{1/2}$ [34]. These results, at first seemingly contrary, can be rectified by acknowledging that the

transition observed in Ref. [34] coincided with the emergence of a precursor film that spread ahead of the liquid drop. Thus, the drop was spreading on a liquid film of the droplet material and this decreased the energy barrier for contact line advancement. MD simulations have been advanced along with experimental observations in Ref. [18] and it was shown that, while the power law exponent did not depend upon equilibrium contact angle, the prefactor in the $R^2 \sim Dt$ relation did.

Perhaps one of the most illustrative examples of the power of atomic scale simulations to inform larger scale descriptions of early stage wetting can be found in recent work where MD results were used to optimize parameters in a continuum phase field model [36]. Specifically, the role of liquid slip at the solid surface was directly elucidated by fitting the slip length in the continuum description to capture atomistic simulation results. With the continuum model so parameterized, the authors were able to demonstrate the relative magnitude of energy dissipation due to liquid slip as compared to viscous effects and inertial effects; for more wettable surfaces, liquid slip was the dominant mechanism and, for all cases examined, it was comparable in magnitude to the other contributions [36]. Despite such a success, a question remains as to the applicability of atomic scale simulations of nanometer scale droplets to understanding regimes where inertial effects dominate wetting. As discussed in Ref. [36], this seeming contradiction is readily eliminated by computing $v = \gamma/\mu$ using a capillary velocity such that $Re_c = \rho\gamma R_0/\mu^2$ ($\gamma$ is the liquid/vapor surface tension). For atomic scale models of fluids that use the common Lennard-Jones description of atomic interaction (e.g. this was used in both Ref. [18] and Ref. [36]) and for typical modeled droplet sizes, the smallest values

of Rec are a bit larger than 1 and the largest are near 10. For simulation results on metallic drops, an embedded atom method theory of atomic interaction is used that accurately describes metallic bonding [8], [41]. Simulations for nanometer scale metallic drops involve liquids with higher ρ and γ but relatively low μ; as such, prior simulations of metallic droplet spreading investigated situations where $Re_C$ is of order 5 to 40. This is also true for new simulation results presented here. While these numbers are such that viscous effects should not be neglected, particularly for Lennard-Jones systems [36], a regime dominated by inertial effects can be anticipated, especially for the largest metallic drops simulated. An equivalent argument can be made using the Ohnesorge number $Oh = \mu/\sqrt{\gamma\rho R_0}$. For many metallic liquids, the droplet radius for which $Oh = 1$ is less than 1 nm. Since this dimensionless number typically distinguishes viscous from inertial regimes [45], this means that even nanometer scale metallic droplets should exhibit an inertial regime observable within MD simulation time scales.

Experiments and simulations have clarified a great deal about spreading during the moments immediately following contact between a droplet and a surface; nonetheless, even very recent work concluded that mechanistic details remain unclear about how rapid contact line advancement during inertial spreading is achieved [32]. The recent work combining MD with phase field descriptions provided a direct computation of the relevant slip length and demonstrated the importance of liquid slip during rapid contact line advancement [36]; nonetheless, questions remain about atomic scale mechanisms inherent in rapid contact line advancement. This knowledge gap

motivates additional molecular scale inertial spreading studies. An additional feature of recent atomic scale simulations is a greater deviation from inertial wetting theory for the smallest drops simulated. For example, in Ref. [36], $R(t)$ data collapse is presented for three droplet sizes where collapse is achieved by invoking a time scaling based on inertial considerations; while collapse is essentially perfect for the two larger drop sizes, deviation is observed for the smallest drop explored ($R_0 = 6.1\,nm$). It is natural to conclude that this is due to lower $Re_c$; however, kinetics exhibited by the system remain well described by $R \sim t^{1/2}$. This too motivates further studies to better explore origins of deviations for very small drops and how they relate to mechanisms of rapid contact line advancement. It is well accepted that many continuum features of fluid flow persist for systems with nanometer scale dimensions; a goal in the discussion below is to explore the droplet length scale at which continuum inertial wetting theory breaks down.

In the remainder of my dissertation, an attempt is made to further illustrate the power of atomic scale simulations for exploring early stage, inertial wetting by investigating the extensibility of continuum derived theory to very small drop sizes. An example is also provided of the mechanistic detail of contact line advancement available from such methods. A system is explored where liquid metal drops wet solid metal substrates; the liquid is Pb and the solid is Cu. The model used to describe metallic interactions properly predicts a very low vapor pressure; the result is that no vapor phase exists in the simulations presented. This is quite different from results presented for liquids described by Lennard-Jones models, which exhibit significant vapor pressure [18],

[36]. Using metallic material models, inertial regime spreading can thus be studied at the atomic scale for a relatively simple liquid (monoatomic liquid entities) and in the absence of any contribution to contact line behavior from vapor phase entities. Though vapor phase effects are important in some spreading scenarios (particularly droplet impact [46]), results presented here permit an idealized focus on liquid phase transport mechanisms - along with solid/liquid interface details - near a rapidly advancing contact line.

## 1.3 Nano-particle Suspension

Liquid drops on solid surfaces have garnered tremendous attention for over two centuries [10], owing to their ubiquity in nature and technology. Much has been learned about driving forces dictating the rate at which a drop spreads across a surface [1], [2]; nonetheless, studies continue to demonstrate rich physical complexity inherent in capillary systems [9]. If solid particles are introduced into a spreading drop, underlying driving forces become more complex, challenging our understanding even further. Research in this area has been invigorated by possibilities for advanced materials fabrication through selective deposition of particle suspension drops and subsequent solvent evaporation. In this manner, potential exists to generate ordered arrays of solid particles on surfaces from a relatively inexpensive, large-scale process and this concept has fueled a large body of research in this area. Applications for such structures exist in the photonic, microelectronic, and biotechnology industries [47]–[50].

Much of the initial attention on suspension drops arose, however, from a more commonplace question: why do coffee drops form ring shaped stains upon evaporation instead of circles [51], [52]? It has been shown that, as a suspension drop evaporates, it does so most rapidly from its edges. As the contact line initially retracts, outward flow develops to carry solvent to the region of highest evaporation; this flow also carries suspended particles to the outer edge, leading to contact line pinning by the particles, or self-pinning. Subsequent evaporation and flow causes particle pile-up at the pinned drop edge, leading to a ring-shaped stain, rather than a circle [52]. Contact line pinning has been extensively considered during contact line retreat due to solvent evaporation [53]–[60]; this is partly because self-pinning is a phenomenon that is highly relevant to manufacturing efforts based on deposition and subsequent evaporation. Suspended particles can also influence advancing contact lines; competing observations have been made with some suspension systems showing increased spreading kinetics and others showing decreased kinetics [61], [62]. The former observation was attributed to a disjoining pressure induced by particle ordering near the contact line; the latter observation was associated with increased surface tension and fluid/solid friction. It is clear that more must be learned to enable accurate predictions of what specific behavior will be observed for varying suspension droplet wetting scenarios.

Self-pinning is a phenomenon intrinsic to the advancement or retraction of liquid/solid/vapor three-phase contact lines for nano-fluid droplets; in such cases, particles entrained to the contact line halt its motion, preventing the system from reaching equilibrium. Depending on the desired application, this can be either detrimental (e.g.

preventing complete coating of a substrate by the suspension) or beneficial (e.g. stabilizing non-equilibrium droplet morphologies). Another relevant phenomenon is de-pinning, where an initially halted contact line is able to separate from the pinning particle and continue its advance (or retraction) across the surface. While experiments have recently revealed quantitative relationships between capillary driving forces, particle-substrate interactions, and observed pinning behavior, much remains unknown about the underlying driving forces dictating nano-fluid droplet spreading behavior. In my dissertation, results from molecular dynamics simulations will be presented to explore directly the forces on nano-particles entrained to advancing contact lines during both pinning and de-pinning events. In cases of constant particle size, the role of the advancing contact angle will be presented, showing that lower advancing contact angle promotes self-pinning. For constant advancing contact angle, a transition with increasing particle size – from de-pinning to pinning – will be explored. Forces associated with this transition will be presented and interpreted in terms of existing analytical expressions for such forces. Later chapter will also address those features in LAMMPS that permit relatively straightforward extraction of forces on suspended particles during suspension droplet wetting simulations.

Self-pinning was recently explored experimentally and a mechanism was advanced based on capillary force due to particle confinement at the contact line [63]. Two relevant forces on a potentially pinning particle were identified: a spreading force $F_S$ and a capillary force $F_C$.The spreading force acts to move particles outward in the radial (spreading) direction and is $F_S = 2\pi RS$, where $R$ is the droplet radius and $S = \gamma_{sg} -$

$\gamma_{sl} - \gamma_{lg}$ ; $\gamma_{sg}$ , $\gamma_{sl}$ , and $\gamma_{lg}$ are the solid/gas, solid/liquid, and liquid/gas interfacial tensions, respectively. When the contact angle is greater than the equilibrium value, a dynamic S can be considered that is greater than zero and drives both droplet and particle spreading. During evaporation and concomitant contact line retraction, the capillary force acts inward in the radial direction; $F_C$ between N pinning particles and the liquid front was given as $F_C = 2\pi r N \gamma_{lg} (\cos\theta)^2$ , where $r$ is the pinning particle radius. The drag force (like $F_S$) acts outward in the radial direction and is given by $F_D = 6\pi r \eta \mu$ , where η is dynamic fluid viscosity and $\mu$ is radial flow velocity; for evaporation driven flow velocities explored in Ref. 21, $F_D$ was demonstrated to be negligible compared to $F_C$. By equating $F_S$ and $F_C$ a critical contact line particle packing for self-pinning was predicted and verified in experiments [63]. Similar approaches have been advanced by other authors. For example, in addition to considering forces due to viscous drag and capillary interaction between the liquid front and particle, one prior study also advanced expressions for the force exerted on potentially pinning particles by an underlying substrate [64]. Again by establishing a force balance, authors were able to predict conditions for contact line pinning. In both of these cited works it was hypothesized that nanometer scale particles can get closer to contact lines, facilitating easier self-pinning. It is clear that predicting the behavior of particles entrained into advancing contact lines requires thorough understanding of constitutive forces in such wetting systems.

Recent studies have shown the capability of atomic scale molecular dynamics (MD) simulations to reveal underlying driving forces dictating changes in surface tension and viscosity for nano particle suspensions [65]. MD simulations have been used to study

particle ordering during suspension evaporation in liquid film geometries [66]. In separate work, MD simulations were used to explore particle ordering during evaporation of suspension droplets [58]. Droplet spreading (i.e. contact line advance) was also recently explored for nano particle suspension drops via MD simulations [62]. While these works have clearly demonstrated the important role that atomic scale modeling plays in studying suspension behavior, no results have been advanced using such simulations to directly examine suspended particles entrained into advancing contact lines during successful versus failed self-pinning attempts.

Here, self-pinning of advancing contact lines by nano particles is explored using MD simulations. The model material system used for liquid, particles, and substrate is such that, for identical solid/liquid chemistry, different spreading kinetics and advancing contact angle $\theta_{adv}$ are observed depending on the crystal structure of the substrate surface. In cases of identical particle loading and initial configuration in the drop, self-pinning is observed for low $\theta_{adv}$ whereas it is not for high $\theta_{adv}$. Mechanisms leading to pinning in the low case are compared to those that manifest liquid front separation from the entrained particle (i.e. de-pinning) in the high case. Forces on particles are computed during pinning and de-pinning to provide further interpretation of mechanisms controlling contact line behavior. Results demonstrate that, for nanometer size particles explored here, forces due to liquid flow are small relative to those manifesting from interactions at the particle/substrate interface.

# 2 Theory and Computational Methods

## 2.1 Atomistic Simulations

Some problems in statistical mechanics are exactly solvable while some problems are not. While not being exactly solvable, those problems succumb to analysis based on some straightforward approximation schemes. However, for some problems, it may not even be clear how to begin constructing an approximate theory in a reasonable way. In this sense, the idea of computer simulations is developed. Computer simulations have a valuable role to play in providing essentially exact results for problems in statistical mechanics which would otherwise only be solvable by approximate methods, or might be quite intractable. Meanwhile, computer simulations also act as a bridge between microscopic length and time scales and the macroscopic world of the laboratory.

Regarding to a computer simulation, a specific model should be built at the very beginning. Then the computer model is basically to be used in two ways: 1. Computational simulations may be carried out and compared to experimental results so as to verify the accuracy of previous model. 2. We may test a theory by conducting a simulation using the same model. Figure 2-1 shows the connecting role made by computer simulations between theory, model, and experiment. For example, the goal of my simulation model presented here is to test the relevant capillary flow theory and then used to improve the existing analytical description of forces during suspension droplet wetting and spreading.

The study of atomic motion and interactions has garnered tremendous interest as it provides much insight to scientists. The field of computer simulation has enjoyed rapid

advances in the last fifty years since the first atomistic simulation of a liquid was carried out at the Los Alamos National Laboratories in the United States by Metropolis et al. in 1953. This work also laid the foundations of modern 'Monte Carlo' simulation. The original models were highly idealized representations of molecules, such as hard spheres and disks, but then MC simulations were carried out on the Lennard-Jones interaction potential which made it possible to compare data between experiments and simulations. It helps scientists to explore and gain new insights into new technology and to estimate the performance of systems too complex for analytical solutions. Atomistic simulation provides a direct route from the microscopic details of a system to macroscopic properties of experimental interest. Figure 2-2 details current theoretical and computational methods as a function of different time and length scales.

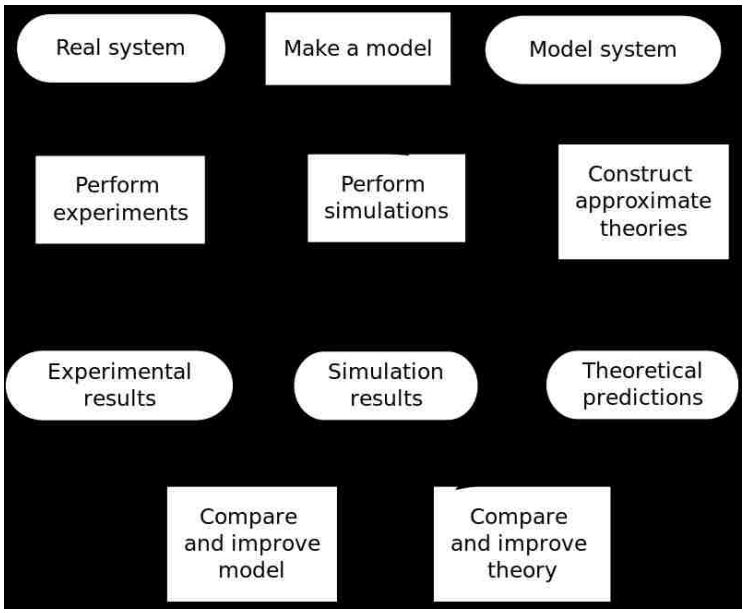


**Figure 2-1:** Process of building a computer model, and the interplay between experiment, simulation, and theory.

Molecular dynamics is another simulation technique which is used to study the physical and chemical processes for computer simulations of complex systems, modelled at the atomic level. The obvious advantage of MD over MC is that it gives a route to dynamical properties of the system: transport coefficients, time-dependent responses to perturbations, etc. MD simulations have important and interesting roles and give us an additional degree of freedom to increase our understanding of nature. The first Molecular dynamics (MD) simulation was accomplished for a system of hard spheres by Alder and Wainwright in the late 1950s and. Due to the revolutionary advances in computer technology and algorithmic improvements, MD has subsequently become a valuable tool in many areas of physics and chemistry.

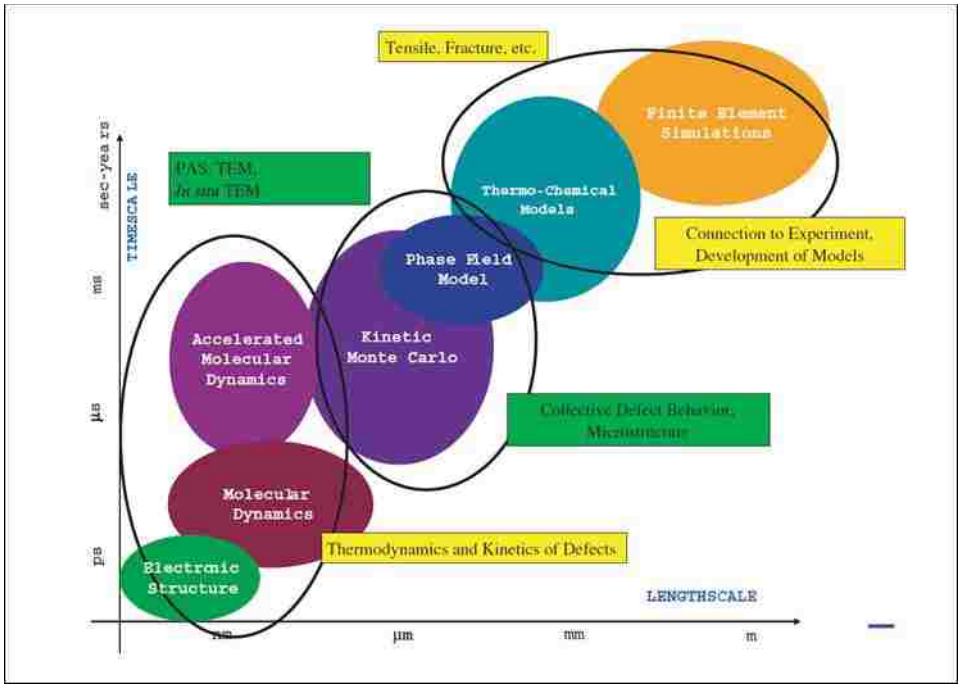


**Figure 2-2:** Theoretical and computational methods used in advanced modeling and simulation along multiple time and length scales.

MD requires the evaluation of the total potential energy of a system of N atoms. The total potential energy is usually the sum of various interactions among the atoms in the system. These terms are functions of atomic coordinate differences, such as the interatomic distances between two atoms, bond angles among three atoms, or torsional angles among four atoms. The realism of the simulation depends on the potential model's ability to reproduce the behavior of the material being simulated. With an appropriate potential selected, then Newton's equations of motion are solved numerically to follow the time evolution of the system, allowing the derivation of kinetic and thermodynamic properties of interest by means of 'computer experiments'.

An MD simulation usually consists of the following steps:

a) Construction of an interaction potential model that defines the microscopic description of the system with a Hamiltonian or Lagrangian.

(Note that: Hamiltonian and Lagrangian formalisms are two reformulations of Newton's equation of motion. they describe the same physics for a system of $N$ particles, and produce same results but only differ in the viewpoints. Lagrangian is naturally associated with an $N$-dim configuration space of independent variables $q_i$ and $\dot{q}_i$, extended by time. While Hamiltonian is the natural description for working in a $2N$-dim phase space of independent variables $q_i$ and $p_i$. Lagrangian function defines as $L = K - V$ and Hamiltonian is given by $H = K + V$, where $K$ and $V$ stands for the kinetic and potential energy of the system.[67])

b) Initialization of positions and velocities.

c) Calculation of force and molecular trajectories by using finite difference methods.

d) Analysis of these trajectories to obtain macroscopic properties of the system.

The MD simulation method is based on the numerical integration of Newton's second law to compute the positions and velocities of each individual atom in the system as they change with time.

## 2.2 Molecular Interactions

Molecular dynamics simulation consists of the numerical solution of the classical equation of motion. If we consider a simple system of atoms, with Cartesian coordinates $\boldsymbol{r}_i$

$$m_i \ddot{\boldsymbol{r}}_i = \boldsymbol{f}_i \tag{2-1}$$

$$\boldsymbol{f}_i = -\frac{\partial}{\partial \boldsymbol{r}_i} \mathcal{V} \tag{2-2}$$

In this manner, $m_i$ stands for the mass of atom $i$ and $\boldsymbol{f}_i$ is the force on that atom derived from a potential energy $\mathcal{V}$. By considering a system containing N atoms, interatomic potentials can be written as a series expansion of functional terms that depend on the coordinates of individual atoms, pairs, triplets, etc. at a time:

$$\mathcal{V} = \sum_i v_1(\boldsymbol{r}_i) + \sum_i \sum_{j>i} v_2(\boldsymbol{r}_i, \boldsymbol{r}_j) + \sum_i \sum_{j>i} \sum_{k>j>i} v_3(\boldsymbol{r}_i, \boldsymbol{r}_j, \boldsymbol{r}_k) + \cdots \tag{2-3}$$

The first term in the above equation represents the effects of an external field on the system and the remaining terms represent particle interactions. The choice of the

interatomic potential is very important before establishing a MD model. Since the atomic force field defines the physical model of the simulated system, the results of simulations will be realistic only if the potential energy function mimics the forces experienced by the real atoms. Proper interatomic potentials should be able to capture some important parameters for given material systems. A summary of some common used interatomic potentials will be shown below.

### 2.2.1 Classes of Interatomic Potentials

**Pair potentials**

The total potential energy of the system of N atoms interacting via pair potential is:

$$U(\vec{r}_1, \vec{r}_2, \ldots, \vec{r}_N) = \sum_i \sum_{j>i} U_2(r_{ij}) \text{ where } r_{ij} = |\vec{r}_j - \vec{r}_i| \quad (2\text{-}4)$$

Commonly used examples of pair potentials:

Lennard-Jones – describes van der Walls interaction in inert gases and molecular systems and is often used to model general effects rather than properties of a specific material.

$$U(r_{ij}) = 4\varepsilon \left[ \left( \frac{\sigma}{r_{ij}} \right)^{12} - \left( \frac{\sigma}{r_{ij}} \right)^{6} \right] \quad (2\text{-}5)$$

Hard/soft spheres – is the simplest potential without any cohesive interaction. Useful in theoretical investigations of some idealized problems.

$$U(r_{ij}) = \begin{cases} \infty & for \quad r_{ij} \le r_0 \\ 0 & for \quad r_{ij} > r_0 \end{cases} \text{ (hard)} \quad (2\text{-}6)$$

$$U(r_{ij}) = \left(\frac{r_{ij}}{r_0}\right)^{-n} \text{ (soft)} \tag{2-7}$$

Ionic – describes Coulomb interaction of charges, strong, long range repulsion or attraction and is often added to other functional forms to account for charge-charge interaction of polarization.

$$U(r_{ij}) = \frac{q_i q_j}{r_{ij}} \tag{2-8}$$

**Potentials for metallic systems**

Since pair potentials cannot provide an adequate description of metallic systems, an alternative simple but rather realistic approach to the description of bonding in metallic systems is based on the concept of local density that is considered as the key variable. This allows one to account for the dependence of the strength of individual bonds on the local environment which is especially important for simulation of surfaces and defects.

Many methods, that have been proposed since early 1980s, have different names (e.g. embedded-atom method - EAM, effective medium theory, Finnis-Sinclair potential, the glue model, corrected effective medium potential - CEM, etc.) and are based on different physical arguments (e.g. tight-binding model, effective-medium theory), but result in a similar expression for the potential energy of an atom $i$:

$$E_i = \sum_i F_i(\rho_{h,i}) + \frac{1}{2}\sum_i \sum_{j(\neq i)} \emptyset_{ij}(R_{ij}) \; where \; \rho_{h,i} = \sum_{j(\neq i)} \rho_j(R_{ij}) \tag{2-9}$$

From the point of view of effective medium theory or the embedded-atom method, the total energy of the atom $i$ is determined by the combination of the embedding energy and the pair-wise interaction. In this expression, $\rho_{h,i}$ is the host electron density at atom $i$ due

to the remaining atoms of the system, $F_i(\rho)$ is the energy to embed atom $i$ into the background electron density $\rho$, and $\emptyset_{ij}(R_{ij})$ is the pair repulsion between atoms $i$ and $j$ separated by the distance $R_{ij}$. The general form of the potential can be considered as a generalization of the basic idea of the Density Functional Theory – the local electron density can be used to calculate the energy.

**Potentials for covalently bounded systems**

There exists some other types of multi-body potential but they are considered more suitable for materials that exhibit covalency in their bonding, such as semi-conductors. Some popular potentials with consideration of the intramolecular bonding interactions are angular-dependent many-body potential for Si (Stillinger-Weber); bond order potential by Tersoff for Si, GaAs, Ge; reactive potential for different forms of carbon and hydrocarbons by Brenner; molecular mechanics potentials (force-field methods), etc. These potentials describe several different bonding states of an atom, and thus to some extent may be able to describe chemical reactions correctly. They were developed partly independently of each other, but share the common idea that the strength of a chemical bond depends on the bonding environment, including the number of bonds and possibly also angles and bond length.

### 2.2.2 Periodic Boundary Conditions

Considering if we want to run computer simulation programs to predict and study the properties of a system in bulk, the system size would have to be extremely large to ensure that the surface has only a small influence on the bulk properties, but this system

would be too large to simulate. In MD simulations, to eliminate surface effect from the computation we use periodic boundary conditions.

In periodic boundary conditions, the simulation box is replicated throughout space to form an infinite lattice shown in a 2-D representation in Figure 2-3. Here the central box is the actual simulation box contains all the atoms (1-4) in the current simulation and atoms can enter and leave each box across each of the four edges. If an atom moves in the central box, then its periodic image in every one of the other boxes moves with exactly the same orientation in exactly the same way. Thus, as an atom leaves the central box, one of its images will enter through the opposite face and replace it (e.g. atom #4 in the Figure 2-3), so the number of particles in the central box stays constant. There are no walls at the boundary of the central box, and the system has no surface. During the simulation, only the properties of the original simulation box need to be recorded and propagated.

Despite the widespread use of periodic boundary conditions in MD simulations, there are still some limitations that should be considered in some particular cases. When doing a MD simulation, it's important to ask if the properties of a small, infinitely periodic system and the macroscopic system which it represents are the same. This will depends on the range of the interatomic potential and the phenomenon being studied. For example, if the potential is long-ranged, another words, the interactions between atoms do not drop to zero even when they are infinitely far away (e.g. in the simulation of charged ions and dipolar molecules), the periodic boundary conditions will induce anisotropy on the fluid structures. There exist methods to split off the long range part of

the fields when dealing with the long-ranged potentials, such as Ewald summation [68]. However even in this case the physical interpretation and consequences of the artificial infinite periodicity is unclear. Another limitation is that the symmetry of the central cell, which is almost always a cube, can be problematic for crystalline solids of non-cubic symmetry. In such cases non-cubic central cells may be employed [69], albeit at the cost of a more complicated code for determining the distance between molecules and their images.

The common experience people gained so far is that periodic boundary conditions have little effect on the equilibrium thermodynamic properties and structures of fluids away from phase transitions and where the interactions are short-ranged.

There are some criteria need to be considered when applying periodic boundary condition. For instance, the size of the computational cell should be larger than $2R_{cut}$, where $R_{cut}$ is the cutoff distance of the interaction potential. In this case any atom $i$ interacts with only one image of any atom $j$. And it does not interact with its own image. This condition is called "minimum image criterion" [68]. Another criterion is that the characteristic size of any structural feature in the system of interest or the characteristic length-scale of any important effect should be smaller than the size of the computational cell. For example, low-frequency parts of the phonon spectrum can be affected, stress fields of different images of the same dislocation can interact, etc. Usually, it's necessary to check if there are any artifacts due to the size of the computational cell by performing simulations with different sizes to check if the result converges.

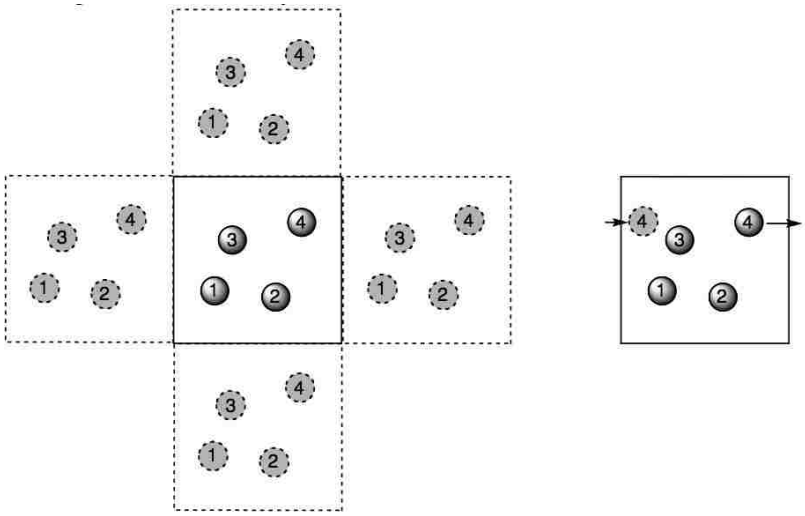

**Figure 2-3**: Periodic boundary conditions for a 2D atomistic simulation. The central box is the actual simulation box where the dashed boxes represent the periodic images of atoms.

### 2.2.3 Neighbor Lists

When we compute the non-bonded contributing to the interatomic forces in a MD simulation, it generally involves a large number of pairwise calculations. In another words, we need to consider each atom i and loop over all other atoms j to calculate the minimum image separations $r_{ij}$. Let us assume that the interaction potentials are of short range, $v(r_{ij}) = 0$ if $r_{ij} > r_{cut}$. In this case, if atoms are separated by distances greater than the potential cutoff, the program skips to the end of the inner loop, avoiding expensive calculations and considers the next candidate j. Nonetheless, the time to examine all pair separations in an N-atom system is proportional to $N^2$; this still consumes a lot of time.

Economies could be achieved by the use of lists of nearby pairs of atoms. Verlet [70] suggested a technique for improving the speed of a program by maintaining a list of the neighbors of a particular atom, which is updated by intervals. Between updates of the

neighbor list, the program does not check through all the j atoms, but just those appearing on the list. For instance, the potential cutoff sphere, of radius $r_{cut}$ around a particular atom is surrounded by a 'skin', to give a larger sphere of radius $r_{list}$ as shown in Figure 2-4. At the first step in a simulation, a list is constructed of all the neighbors of each atom, for which the pair separation is within $r_{list}$. Over the next few MD time steps, only pairs appearing in the list are checked in the force routine. From time to time the list is reconstructed: it is important to do this before any unlisted pairs have crossed the safety zone and come within interaction range. A dynamic way of determining when to update the neighbor list is to keep track of the two largest atom displacement $r_{max,1}$and $r_{max,2}$ from the time when the neighbor list was updated the last time. The list should be updated when $r_{max,1} + r_{max,2} > r_{list} - r_{cut}$. The choice of list cutoff distance $r_{list}$ is a compromise: larger lists will need to be reconstructed less frequently, but will not give as much of a saving on cpu time as smaller lists. This choice can easily be made by experimentation.

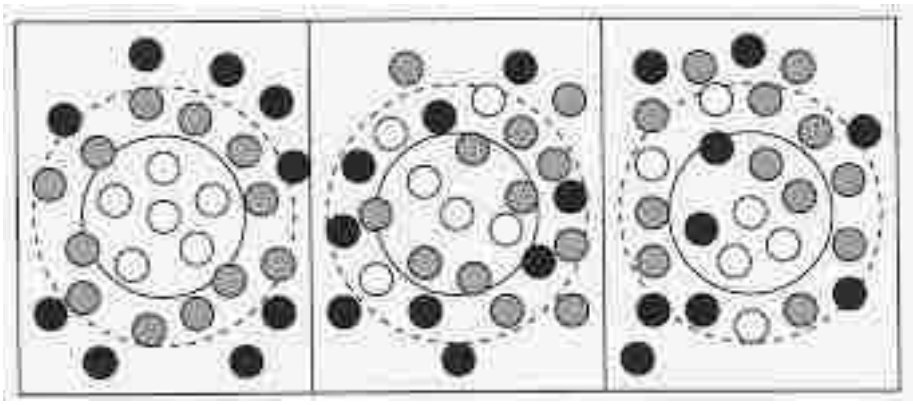

**Figure 2-4:** The Verlet neighbor list on its construction, later, and too late. The potential cutoff range (solid circle), and the list range (dashed circle) are indicated. The list must be reconstructed before particles originally outside the list range (black) have penetrated the potential cutoff sphere.

## 2.3 The MD Algorithm

As we stated earlier, in MD simulations the time evolution of a set of interacting particles is followed via the solution of Newton's equations of motion. Continuing to discuss, for simplicity, a system composed of atoms with coordinates $(q_1, q_2, \dots, q_N)$ and potential energy $\mathcal{V}(q)$, we introduce the atomic momenta $(p_1, p_2, \dots, p_N)$, in terms of which the kinetic energy for a system of N atoms with masses $m_i$ may be written as

$$\mathcal{K} = \sum_{i=1}^{N} \sum_{\alpha} {p_{i\alpha}}^2 / 2m_i \tag{2-10}$$

Here, the index $\alpha$ runs over the different $(x, y, z)$ components of the momentum of atom $i$. Then the total energy of the system, or Hamiltonian, $\mathcal{H}$, could be described as a sum of kinetic and potential energies, as shown below

$$\mathcal{H}(q, p) = \mathcal{K}(p) + \mathcal{V}(q) \tag{2-11}$$

To integrate the Newton's equation of motion, the instantaneous forces acting on the atoms and their initial position and velocities need to be specified. Due to the many body nature of the problem, the equations of motion are discretized and solved numerically. The MD trajectories are defined by both position and velocity vectors and they describe the time evolution of the system in phase space. Accordingly, the positions and velocities are propagated with a finite time interval using numerical integrators, for example the Verlet algorithm.

### 2.3.1 Verlet Algorithm

The most widely used method of integrating the equations of motion was initially adopted by Verlet [70]. This method comes from the direct solution of the second-order equations (2-1). The method is derived from two Taylor expansions about $\boldsymbol{r}(t)$:

$$\begin{aligned} \boldsymbol{r}(t+\delta t) &= \boldsymbol{r}(t) + \delta t \boldsymbol{v}(t) + \left(\frac{1}{2}\right)(\delta t)^2 \boldsymbol{a}(t) + \cdots \\ \boldsymbol{r}(t-\delta t) &= \boldsymbol{r}(t) - \delta t \boldsymbol{v}(t) + \left(\frac{1}{2}\right)(\delta t)^2 \boldsymbol{a}(t) - \cdots \end{aligned} \tag{2-12}$$

By adding these two equations together, one could obtain the equation for advancing the positions at next step $\boldsymbol{r}(t+\delta t)$:

$$\boldsymbol{r}(t+\delta t) = 2\boldsymbol{r}(t) - \boldsymbol{r}(t-\delta t) + (\delta t)^2 \boldsymbol{a}(t) \tag{2-13}$$

Here, the velocity terms have been eliminated by addition of the equations (2-12), however, they would be useful for estimating the kinetic energy from the formula

$$v(t) = \frac{\boldsymbol{r}(t+\delta t) - \boldsymbol{r}(t-\delta t)}{2\delta t} \tag{2-14}$$

Hence, the velocities are not explicitly solved as they are calculated typically from first order central difference. The global error in position and velocity is of order $\delta t^2$.

Standard Verlet algorithm provides simplicity and good numerical stability as well as other properties such as time-reversibility and excellent energy-conserving properties even with long time steps. Nonetheless, the weakness comes from the global error induced accuracy. To overcome this difficulty, some variants of the Verlet algorithm have been developed. They give rise to exactly the same trajectory, and differ in what variables are stored in memory and at what times.

### 2.3.2 Velocity Verlet Algorithm

Comparing to the standard Verlet algorithm, velocity Verlet scheme provides a better implementation and improves accuracy, where positions, velocities at time $t + \delta t$ are obtained from the same quantities at time $t$. It starts with position and velocity expansions:

$$\begin{aligned} \boldsymbol{r}(t+\delta t) &= \boldsymbol{r}(t) + \delta t \boldsymbol{v}(t) + \left(\frac{1}{2}\right)(\delta t)^2 \boldsymbol{a}(t) + \cdots \\ \boldsymbol{v}(t+\delta t) &= \boldsymbol{v}(t) + \left(\frac{1}{2}\right)\delta t[\boldsymbol{a}(t) + \boldsymbol{a}(t+\delta t) \ldots \end{aligned} \tag{2-15}$$

Within each integration cycle, velocities are calculated at mid-step:

$$\boldsymbol{v}(t+\delta t/2) = \boldsymbol{v}(t) + \left(\frac{1}{2}\right)\delta t \boldsymbol{a}(t) \tag{2-16}$$

Then from this, we could get positions at the next step:

$$\boldsymbol{r}(t+\delta t) = \boldsymbol{r}(t) + \boldsymbol{v}(t+\delta t/2)\delta t \tag{2-17}$$

Finally, after calculating accelerations at next step from the potential, velocities are updated such that:

$$\boldsymbol{v}(t+\delta t) = \boldsymbol{v}(t+\delta t/2) + \left(\frac{1}{2}\right)\delta t \boldsymbol{a}(t+\delta t) \tag{2-18}$$

There are also some other popular integration algorithms, such as Leap-Frog, Beeman, predictor-corrector, etc. However, I'll not describe them all here since they are in a similar manner as the velocity Verlet integrator.

## 2.4 Simulation Ensembles and Statistical Averages

### 2.4.1 Different Ensembles in MD

In a molecular dynamics simulation, we often wish to explore the macroscopic properties of a system through microscopic simulations. The connection between microscopic simulations and macroscopic properties is made via statistical mechanics which provides the rigorous mathematical expressions that relate macroscopic properties to the distribution and motion of the atoms and molecules of the N-body system; molecular dynamics simulations provide the means to solve the equation of motion and evaluate these mathematical formulas. With molecular dynamics simulations, we could study both thermodynamic properties and/or time dependent (kinetic) phenomenon. Statistical mechanics is the branch of physical sciences that studies macroscopic systems from a molecular point of view. The goal is to understand and to predict macroscopic phenomena from the global properties of individual molecules making up the system.

The thermodynamic state of a system is usually defined by a small set of parameters, for example, the temperature, T, the pressure, P, and the number of particles, N. Other thermodynamic properties may be derived from the equations of state and other fundamental thermodynamic equations. The mechanical or microscopic state of a system is defined by the atomic positions, q, and momenta, p; these can also be considered as coordinates in a multidimensional space called phase space. For a system of N particles, this space has 6N dimensions. A single point in phase space, denoted by G, describes the state of the system.

An ensemble is a collection of points in phase space satisfying the conditions of a particular thermodynamic state. A molecular dynamics simulation generates a sequence of points in phase space as a function of time; these points belong to the same ensemble, and they correspond to the different conformations of the system and their respective momenta. Several different ensembles are described below.

- Microcanonical ensemble (NVE): The thermodynamic state characterized by a fixed number of atoms, N, a fixed volume, V, and a fixed energy, E. This corresponds to an isolated system.
- Canonical Ensemble (NVT): This is a collection of all systems whose thermodynamic state is characterized by a fixed number of atoms, N, a fixed volume, V, and a fixed temperature, T.
- Isobaric-Isothermal Ensemble (NPT): This ensemble is characterized by a fixed number of atoms, N, a fixed pressure, P, and a fixed temperature, T.
- Grand canonical Ensemble (μVT): The thermodynamic state for this ensemble is characterized by a fixed chemical potential, μ, a fixed volume, V, and a fixed temperature, T.

For those thermodynamic quantities which are not fixed in the ensemble, they are computed via ensemble averaging for particular state points using the appropriate probability density and relevant partition functions; these will be described below.

### 2.4.2 Ensemble Averaging

An experiment is usually made on a macroscopic sample that contains an extremely large number of atoms or molecules sampling an enormous number of

conformations. In statistical mechanics, averages corresponding to experimental observables are defined in terms of ensemble averages; one justification for this is that there has been good agreement with experiment. An ensemble average is average taken over a large number of replicas of the system considered simultaneously.

In order to connect the macroscopic system to the microscopic system, the ensemble average is given by

$$\langle A \rangle_{ensemble} = \iint dp^N dr^N A(p^N, r^N) \rho(p^N, r^N) \tag{2-19}$$

where $A(p^N, r^N)$ is the observable of interest and it is expressed as a function of the momenta, p, and the positions, r, of the system. The integration is over all possible variables of r and p.

In the canonical ensemble NVT, where the temperature is the thermodynamic property kept fixed, the probability density corresponds to the Boltzmann function and is given by

$$\rho(p^N, r^N) = \frac{1}{Q} exp[-H(p^N, r^N)/k_B T] \tag{2-20}$$

where H is the Hamiltonian, T is the temperature, $k_B$ is Boltzmann's constant and Q is the partition function

$$Q = \iint dp^N dr^N \, exp[-H(p^N, r^N)/k_B T] \tag{2-21}$$

This integral is generally extremely difficult to calculate because one must calculate all possible states of the system. In a molecular dynamics simulation, the points in the ensemble are calculated sequentially in time, so to calculate an ensemble average, the

molecular dynamics simulations must pass through all possible states corresponding to the particular thermodynamic constraints.

Another way, as done in an MD simulation, is to determine a time average of A, which is expressed as

$$\langle A \rangle_{time} = \lim_{\tau \to \infty} \frac{1}{\tau} \int_{t=0}^{\tau} A(p^N(t), r^N(t)) dt \approx \frac{1}{M} \sum_{t=1}^{M} A(p^N, r^N) \tag{2-22}$$

where τ is the simulation time, M is the number of time steps in the simulation and $A(p^N, r^N)$ is the instantaneous value of A.

The dilemma appears to be that one can calculate time averages by molecular dynamics simulation, but the experimental observables are assumed to be ensemble averages. Resolving this leads us to one of the most fundamental axioms of statistical mechanics, the ergodic hypothesis, which states that the time average equals the ensemble average.

The Ergodic hypothesis states

$$\langle A \rangle_{ensemble} = \langle A \rangle_{time} \tag{2-23}$$

The basic idea is that if one allows the system to evolve in time indefinitely, that system will eventually pass through all possible states. One goal, therefore, of a molecular dynamics simulation is to generate enough representative conformations such that this equality is satisfied. If this is the case, experimentally relevant information concerning structural, dynamic and thermodynamic properties may then be calculated using a feasible amount of computer resources. Because the simulations are of fixed duration, one must be certain to sample a sufficient amount of phase space.

## 2.5 Limitations of Molecular Dynamics

Typical MD simulations can nowadays be performed on systems containing hundred thousands, or, perhaps, millions of atoms, and for simulation times ranging from a few nanoseconds to more than one microsecond. While these numbers are certainly respectable, it may happen to run into conditions where time and/or size limitations become important.

The maximum timestep of integration in MD simulation is defined by the fastest motion in the system. Vibrational frequencies in a molecular system are up to 3000 $cm^{-1}$ which corresponds to a period of ~10 fs. Optical phonon frequencies are ~10 THz - period of ~100 fs. Therefore, a typical timestep in MD simulation is on the order of a femtosecond.

Using modern computers it is possible to calculate $10^8 \sim 10^9$ timesteps. Therefore, we can only simulate processes that occur within 100 $ns$ - 1 $\mu s$. This is a serious limitation for many problems that involve thermally-activated processes, cluster/vapor film deposition, annealing of irradiation damage, etc.

The size of the computational cell is limited by the number of atoms that can be included in the simulation, typically $10^8 \sim 10^9$. This corresponds to the size of the computational cell on the order of tens of nm to micron. Any structural features of interest and spatial correlation lengths in the simulation should be smaller than the size of the computational cell. To make sure that the finite simulations size of the computational cell does not introduce any artifacts into the simulation results, one can perform simulations for systems of different size and compare the predicted properties.

## 2.6 Other computational simulation methods

### 2.6.1 Monte Carlo

Besides molecular dynamics simulations, there exists another approach to perform molecular simulations, which is called Monte Carlo method. As I already discussed above, molecular dynamics is a deterministic approach, which actually simulates the time evolution of the molecular system and provides us with the actual trajectory of the system. The information generated from MD simulations can in principle be used to characterize fully the thermodynamic state of the system. However, Monte Carlo is a stochastic approach, and is based on exploring the energy surface by randomly probing the geometry of the molecular system (or, in a statistical mechanics language, its configuration space). The most popular realization of the Monte Carlo method for molecular systems is the Metropolis sampling method. It is essentially composed of the following steps:

1. Specify the initial atom coordinates (e.g. from molecular mechanics geometry optimization).
2. Select some atom $i$ randomly and move it by random displacement: $\Delta X_i, \Delta Y_i, \Delta Z_i$.
3. Calculate the change of potential energy $\Delta V$ corresponding to this displacement.
4. If $\Delta V < 0$ accept the new coordinates and go to step 2.

5. Otherwise, if $\Delta V \geq 0$, select a random number $R$ in the range [0,1] and if $e^{-\Delta V/kT} < R$ accept the new coordinates and go to step 2; if $e^{-\Delta V/kT} \geq R$ keep the original coordinates and go to step 2.
6. Repeat steps 2-5 to obtain a final estimation $\bar{A} = \langle A \rangle + \delta A$, where $\bar{A}$ is an average of observable $\hat{A}$.

The choice between Monte Carlo and molecular dynamics is largely determined by the phenomenon under investigation. For a simulation of a gas or other low density systems, Monte Carlo simulations are preferable [71]. There can be large energy barriers to torsional rotations in molecules which can lead to molecules being trapped in a few low energy conformations in a MD simulation, leading to poor conformational sampling. In contrast, the random moves in a MC simulation can easily lead to barrier crossings. For a liquid simulation, MD becomes favorable since molecular collisions exchange energy between molecules, enabling barrier crossings, improving the ability of MD to sample conformations. For a MC simulation, there is a large probability of selecting random moves for which two or more molecules overlap (especially for rotations near the center of molecules with long tails such as liquid crystals), leading to large number of rejected moves and a decrease in efficiency of sampling. However, the ability of MC to make unphysical moves, for example to flip a molecule around, can in some cases compensate for this. MD also handles collective motions better than MC. MD also handles collective motions better than MC. However, recently methods such as Configurational Bias Monte Carlo and Hybrid Monte Carlo have been developed to improve the performance of MC simulations [72]. There are some situations where only

one method is appropriate. Determination of transport properties such as viscosity coefficients is largely only possible using MD as MC lacks an objective definition of time (except in some special cases such as the bond fluctuation model for polymers). On the other hand MC can be used for simulations with varying particle numbers (Grand Canonical Monte Carlo) by adding moves for the creation and destruction of particles.

### 2.6.2 Ab initio DFT

Density functional theory provides a powerful tool for computations of the quantum state of atoms, molecules and solids, and of ab-initio molecular dynamics. It was conceived in its initial naive and approximate version by Thomas and Fermi immediately after the foundation of quantum mechanics, in 1927.

In 1964, Hohenberg and Kohn published a paper, and made the foundation of the DFT mansion firm. The core spirit of DFT is to substitute the complicated and thus hard-to-compute many-electron wavefunction, which contains 3N variables (N is the number of electrons, and each electron has 3 spatial variables), with the functional (functional is the function of another function, which map a number to a function) of electron density, which contains only 3 variables. So in the new system, we don't need to be worried about the huge amount of 3N variables, instead, we only deal with 3 variables, which is far easier to handle. Hohenberg and Kohn proposed their first theorem, which points out the ground state energy uniquely depends on the electron density, which means it is a functional of electron density. Their second theorem proved that by minimizing the

energy of the system according to the electron density, ground state energy can be obtained.

H-K theorems only provide the truth that there exists one-to-one mapping relations between electron density functional and system properties, but they don't give anything exactly about what these relations are. Thus, the most general used methods, instead of the "minimizing the system energy", is the Kohn-Sham method. Kohn and Sham published a paper in 1965, only one year later than the publishing of Hohenberg and Kohn's important paper, and in this paper they simplified the multi-electron problem into a problem of non-interaction electrons in an effective potential. This potential includes the external potential and the effects of the Coulomb interactions between the electrons, e.g., the exchange and correlation interactions. Dealing with the exchange and correlation interaction is the difficulty within KS-DFT. So far, there still doesn't exist a rigorous way to solve the exchange and correlation energy. However, the simplest approximation is the Local-Density Approximation (LDA). LDA is based upon using the uniform electron gas model to get the exchange energy (which exact value can be got from the Thomas-Fermi model), and to get the correlation energy from fits to the uniform electron gas. By transforming the problem into the non-interacting system in an effective potential, wavefunction can be easily represented by a Slater determinant of orbitals, the kinetic energy functional of this system is exactly known. But the exchange-correlation part of the total energy functional remains unknown.

DFT has become very popular for calculations in solid state physics since 1970s. Compare to other methods dealing with the quantum mechanical multi-body problems,

LDA give satisfactory results with experimental data. But in quantum Chemistry area, DFT was still not accurate until 1990s, when the approximation methods were greatly refined to better model the exchange-correlation interaction. DFT is now a leading method for electronic structure calculations in many areas. However, it's still difficult to use DFT to treat the strongly correlated systems, band gap in semiconductors, and strong dispersion systems. So the development of DFT is going on.

The quantum mechanical wave function contains in principle, all the information about a given system. For the case of a simple 2-D square potential or even a hydrogen atom we can solve the Schrödinger equation exactly in order to get the wave function of the system. We can then determine the allowed energy states of the system. Unfortunately it is impossible to solve the Schrödinger equation for an N-body system. Evidently, we must involve some approximations to render the problem solvable albeit tricky. Here Density Functional Theory can be simply defined as a method of obtaining an approximate solution to the Schrödinger equation of a many-body system.

A functional is a function of a function. In DFT the functional is the electron density which is a function of space and time. The electron density is used in DFT as the fundamental property unlike Hartree-Fock theory which deals directly with the many-body wavefunction. Using the electron density significantly speeds up the calculation. Whereas the many-body electronic wavefunction is a function of 3N variables (the coordinates of all N atoms in the system) the electron density is only a function of x, y, z -only three variables. Of course simply doing any old calculation fast is not good enough - we also need to be sure that we can derive something significant from it. It was

Hohenburg and Kohn who stated a theorem which tells us that the electron density is very useful. The Hohenburg-Kohn theorem asserts that the density of any system determines all ground-state properties of the system. In this case the total ground state energy of a many-electron system is a functional of the density. So, if we know the electron density functional, we know the total energy of our system.

From that time on, density functional theory has grown vastly in popularity, and a flood of computational work in molecular and solid state physics has been the result. Motivated by its success, there has been always a tendency to widen the fields of application of density functional theory.

### 2.6.3 VOF Level Set

Molecular dynamics (MD) and computational fluid dynamics (CFD) allow researchers to study fluid dynamics from two very different standpoints. From a microscopic standpoint, molecular dynamics uses Newton's second law of motion to simulate the interatomic behavior of individual atoms, using statistical mechanics as a tool for analysis. In contrast, CFD describes the motion of a fluid from a macroscopic level using the transport of mass, momentum, and energy of a system as a model. Here, I will address some key points of CFD and especially introduce two computational models being used in modern CFD simulations, which are Volume of Fluid (VOF) method and Level Set Method (LSM).

Computational Fluid Dynamics (CFD) is a computational technique of fluid dynamics providing a cost-effective means of simulating real flows by the numerical solution of the governing equations. The governing equations for Newtonian fluid dynamics, namely the Navier-Stokes equations, have been known for over 150 years. However, the development of reduced forms of these equations is still an active area of research, in particular, the turbulent closure problem of the Reynolds-averaged Navier-Stokes equations. For non-Newtonian fluid dynamics, chemically reacting flows and two phase flows, the theoretical development is at less advanced stage.

Even though experimental methods has played an important role in validating and exploring the limits of the various approximations to the governing equations, particularly wind tunnel and rig tests that provide a cost-effective alternative to full-scale testing. The governing equations of flow are extremely complicated such that analytic solutions cannot be obtained for most practical applications.

Computational techniques replace the governing partial differential equations with systems of algebraic equations that are much easier to solve using computers. The steady improvement in computing power, since the 1950's, thus has led to the emergence of CFD. This branch of fluid dynamics complements experimental and theoretical fluid dynamics by providing alternative potentially cheaper means of testing fluid flow systems. It also can allow for the testing of conditions which are not possible or extremely difficult to measure experimentally and are not amenable to analytic solutions.

VOF

In computational fluid dynamics, the 'volume of fluid (VOF) method' is a free-surface modelling technique, i.e. a numerical technique for tracking and locating the free surface (or fluid-fluid interface). It belongs to the class of Eulerian methods which are characterized by a mesh that is either stationary or is moving in a certain prescribed manner to accommodate the evolving shape of the interface. As such, VOF is an advection scheme—a numerical recipe that allows the programmer to track the shape and position of the interface, but it is not a standalone flow solving algorithm. The Navier–Stokes equations describing the motion of the flow have to be solved separately.

In each cell of a mesh it is customary to use only one value for each dependent variable defining the fluid state. The use of several points in a cell to define the region occupied by fluid, therefore, seems unnecessarily excessive. Suppose, however, that we define a function F whose value is unity at any point occupied by fluid and zero otherwise. The average value of F in a cell would then represent the fractional volume of the cell occupied by fluid. In particular, a unit value of F would correspond to a cell full of fluid, while a zero value would indicate that the cell contained no fluid. Cells with F values between zero and one must then contain a free surface. Thus, the fractional volume of fluid (VOF) method [73] provides the same coarse interface information available to the marker particle method. Yet the VOF method requires only one storage word for each mesh cell, which is consistent with the storage requirements for all other dependent variables.

In addition to defining which cells contain a boundary, marker particles also define where fluid is located in a boundary cell. Similar information can be obtained in

the VOF method. The normal direction to the boundary lies in the direction in which the value of F changes most rapidly. Because F is a step function, however, its derivatives must be computed in a special way, as described below. When properly computed, the derivatives can then be used to determine the boundary normal. Finally, when both the normal direction and the value of F in a boundary cell are known, a line cutting the cell can be constructed that approximates the interface there. This boundary location can then be used in the setting of boundary conditions.

Although the VOF technique can locate free boundaries nearly as well as a distribution of marker particles, and with a minimum of stored information, the method is worthless unless an algorithm can be devised for accurately computing the evolution of the F field. The time dependence of F is governed by the equation,

$$\frac{\partial F}{\partial t} + u\frac{\partial F}{\partial x} + v\frac{\partial F}{\partial y} = 0 \qquad (2\text{-}24)$$

This equation states that F moves with the fluid, and is the partial differential equation analog of marker particles. In a Lagrangian mesh, Eq.(2-24) reduces to the statement that F remains constant in each cell. In this case, F serves solely as a flag identifying cells that contain fluid. In an Arbitrary Lagrangian-Eulerian mesh, the flux of F moving with the fluid through a cell must be computed, but standard finite-difference approximations would lead to a smearing of the F function and interfaces would lose their definition. When Eq.(2-24) is integrated over a computational cell, the changes in F in a cell reduce to fluxes of F across the cell faces. As previously noted, special care must be taken in computing these fluxes to preserve the sharp definition of free surfaces. Fortunately, the fact that F is a step function with values of zero or one permits the use of

a flux approximation that preserves its discontinuous nature. This approximation, referred to as a donor-acceptor flux approximation [74]. The essential idea is to use information about F downstream as well as upstream of a flux boundary to establish a crude interface shape, and then to use this shape in computing the flux.

In summary, the VOF method offers a region-following scheme with minimum storage requirements. Furthermore, because it follows regions rather than surfaces, all logic problems associated with intersecting surfaces are avoided with the VOF technique. The method is also applicable to three-dimensional computations, where its conservative use of stored information is highly advantageous.

Thus, the VOF method provides a simple and economical way to track free boundaries in two- or three-dimensional meshes. In principle, the method could be used to track surfaces of discontinuity in material properties, in tangential velocity, or any other property. The particular case being represented determines the specific boundary condition that must be applied at the location of the boundary. For situations where the surface does not remain fixed in the fluid, but has some additional relative motion, the equation of motion must be modified. Examples of such applications are shock waves, chemical reaction fronts, and boundaries between single-phase and two-phase fluid regions.

Level Set

Evolving boundaries or interfaces are part of many problems in science and engineering. In 1988, James A. Sethian and Stanley Osher proposed to represent these boundaries implicitly and model their propagation using appropriate partial differential

equations. The boundary is given by level sets of a function $\emptyset(x)$, and they named their technique the Level Set Method.

The level set method is a simple and versatile method for computing and analyzing the motion of an interface Γ in two or three dimensions. Γ bounds a (possibly multiply connected) region Ω. The goal is to compute and analyze the subsequent motion of Γ under a velocity field ~v. This velocity can depend on position, time, the geometry of the interface and the external physics.

First the initial level set grid is calculated as the signed distance function from a given initial surface. In the main loop the surface is extracted and a time step in the physical model is performed. In our applications this means a radiosity of diffusion time step. Thus the speed function at the surface is found. In the next combined step, a temporary signed distance function is constructed, the speed function is extended, and the new active grid points in a narrow band around the zero level set are determined. Then the values of the speed function in the active narrow band are used to update the level set grid using a finite difference scheme.

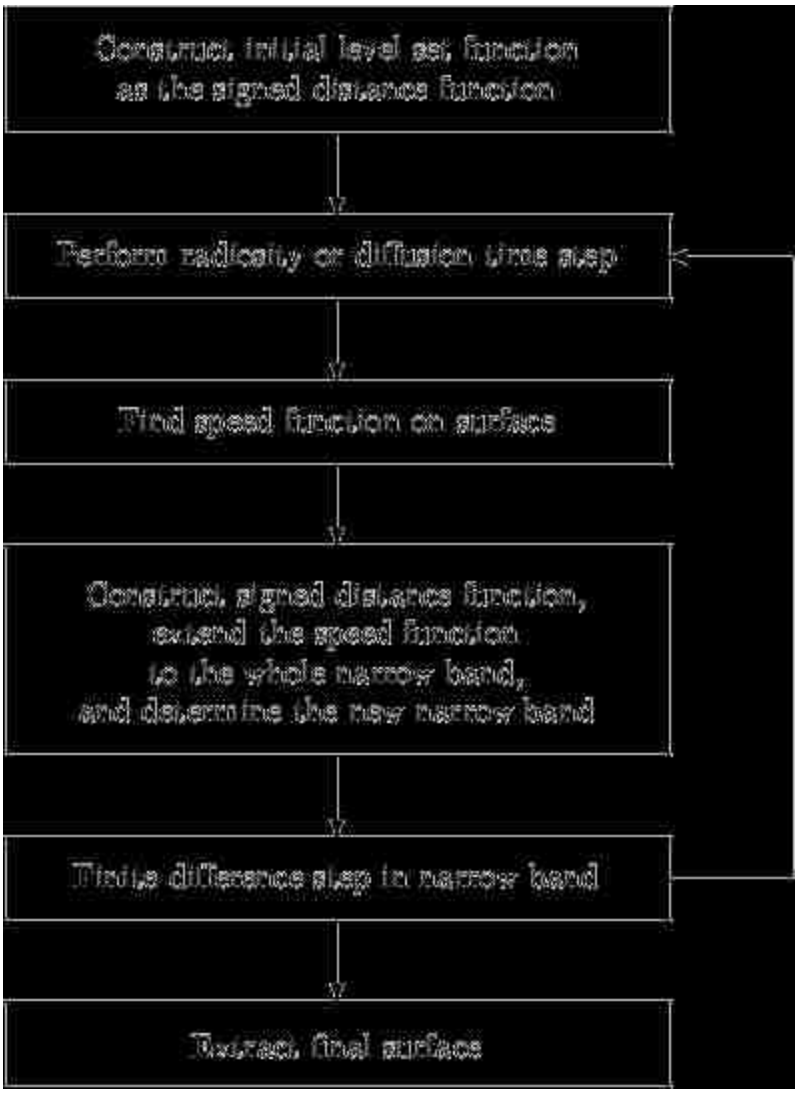


**Figure 2-5:** Overview of the simulation flow combining transport by physical models and surface evolution using the level set method. The simulation stops when a prescribed time is reached or when a layer of prescribed thickness has been deposited.

# 3 Literature Survey

This section begins with the review of the previous works relevant to the general wetting and spreading behavior. There are different mechanisms and conditions that play

a considerable role on various wetting and spreading phenomena. The static state when droplets have already reached to the equilibrium will be discussed.

Subsequently, more specific studies related to the basic concepts of spreading and those different theories being revealed in dynamic spreading are also elucidated.

## 3.1 Droplet wetting and spreading

### 3.1.1 Statics

If we consider a liquid drop on a solid substrate, there are three different phases present; see Figure 3-1. Therefore, there are three surface tensions that need to be considered: solid-liquid, liquid-gas, and solid-gas. Young's equation Eq.(2-1) gives the relation between the equilibrium contact angle and the three surface tensions.

Here the surface tensions are defined when the three phases, solid, liquid, and gas, are at least in mechanical equilibrium (force balance) with each other. In addition, we consider chemical equilibrium (chemical potential matching for each component present) and thermal equilibrium (temperature matching) between liquid and gas. Mechanical, chemical, and thermal equilibrium together are referred to as thermodynamic equilibrium. Meanwhile, the equilibrium contact angle is understood to be measured macroscopically, on a scale above that of long-ranged intermolecular forces.

If the three tensions are known, the wetting state of the fluid follows directly. If $\gamma_{sg} < \gamma_{sl} + \gamma_{lg}$ , a droplet with a finite contact angle minimizes the free energy of the system; we speak of partial wetting. On the other hand, if $\gamma_{sg} = \gamma_{sl} + \gamma_{lg}$, the contact

angle is zero. The system will consequently be in equilibrium when a macroscopic uniform liquid layer covers the whole solid surface, and we speak of complete wetting. The distinction between the different wetting states is usually made by considering the equilibrium spreading coefficient $S_{eq} \leq 0$, which represents the surface free energy $\gamma_{sg}$ relative to its value for complete wetting:

$$S_{eq} \equiv \gamma_{sg} - (\gamma_{sl} + \gamma_{lg}) = \gamma_{lg}(\cos\theta - 1) \qquad (3\text{-}1)$$

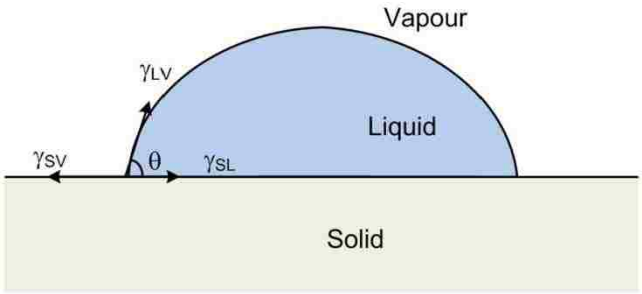


**Figure 3-1:** Young's equation can also be interpreted as a mechanical force balance on the three-phase contact line; the surface tension is an energy per unit area, equivalent to a force per unit length acting on the contact line.

### 3.1.2 Basic concepts of spreading

If a drop is placed on a solid surface, it will in general be far from its equilibrium state, which means the initial spreading coefficient $S_{in} \neq S_{eq}$. Hence a flow is set in

motion until the equilibrium contact angle is reached. The hydrodynamics of this problem has been studied extensively. For complete wetting, the drop spreads almost forever, presumably until it reaches a thickness set by the van der Waals forces. If the static contact angle is finite but small, the initial stages are similar, followed by relaxation toward a static shape.

Now let us consider the simplest case of a small viscous droplet spreading on a surface which it wets completely. By small we mean that the drop radius is smaller than the capillary length $l_c = \sqrt{\gamma/\rho g}$, so that gravity is negligible. The drop is well approximated by a spherical cap, corresponding to an equilibrium liquid-vapor surface of the drop. This is to be expected since the ratio of viscous to surface tension forces, as measured by the capillary number

$$Ca = U\eta/\gamma, \tag{3-2}$$

is very small, as is the case for most spreading experiments. Here $U = \dot{R}$ is the contact line speed and η is the viscosity of the liquid.

### 3.1.3 The Dynamics of spreading

The dynamic wetting phenomenon is important in numerous industrial and natural processes. When a fluid is displacing another immiscible fluid on a solid surface, the point at which the three phases meet is known as three phase boundary. If the three phase contact line is in continuous motion, it is called dynamic wetting. The angle between the moving contact line and solid surface is defined as the dynamic contact angle; depending upon the direction of the contact line movement, it is classified either as the advancing

contact angle or as the receding contact angle. Because the complete mechanism of dynamic wetting is not understood, it is important to understand the basic controlling mechanism of the wetting process and to develop models to predict the behavior of the system beyond the experimental limitations.

In the modeling of dynamic wetting, the main challenge is that the real wetting process usually takes place at submicroscopic length scales, however, the typical experimental observations are made at macroscopic scales. There are two widely recognized dynamic wetting models in the literature: hydrodynamic and molecular - kinetic. The hydrodynamic model describes the dynamic wetting in terms of bulk viscous dissipation and does not take the solid surface into account, whereas the molecular kinetic model describes the dynamic wetting as a rate process of molecular "jumps" on a solid surface. Recently, a combined molecular-hydrodynamic model has been proposed. There are controversies over the applicability of these theories to the dynamic wetting behavior of liquids on solid surfaces and the relationship between the models' parameters and physicochemical properties of solids and/or liquids.

# 4 Computational Procedure and Simulation Geometry

## 4.1 Preparation of Pb Droplets on Cu(001) and Cu(111) Substrates

Classical MD simulations employing the embedded atom method (EAM) [8] are used to model the metallic system of Pb(l) drops spreading on Cu solid substrates. The interatomic potential functions describing Cu-Cu, Pb-Pb, and Pb-Cu interactions

were presented previously; they were fit to numerous bulk properties and the cross-term was fit, among other things, to reproduce the liquid phase miscibility gap observed for this system [8], [75], [76]. Experiments have shown that Pb wets polycrystalline Cu surfaces with negligible substrate dissolution into the spreading liquid and with drops forming final contact angles $\theta_0 = 45°$ to $20°$ for T = 600 K to 1000 K; additionally, an atomically thick layer of Pb is observed to wet the Cu surface between discrete droplets [2], [77]. Wetting for Pb(l) on Cu has been explored in MD simulations previously [41] and it was found that the classical interatomic potentials used for this system gave good agreement with experimental observations. Specifically, the model predicts that wetting occurs in the absence of substrate dissolution into the spreading liquid and final contact angles for T = 700 K are $\theta_0 \sim 30°$ on Cu(001) and $\theta_0 \sim 20°$ on Cu(111); drops adopt these final contact angles on a precursor wetting film that eventually fully wets the substrate. Thus, in both experiment and simulations, the final wetting state has finite $\theta_0$ atop a fully wetting, atomically thick film. Furthermore, in agreement with more recent experiments [78], [79], the model predicts that spreading on (111) is more rapid than on (001) and this is at least partly associated with very rapid precursor film formation on (111) as well as formation of a surface alloy phase on the Cu(001) surface [41].

All simulations were performed with LAMMPS [80] and isothermal wetting simulations for T = 700 K were explored in all cases. This T is to be compared to the predicted melting point for the model of Pb used here ($T_m = 618\,K$) [76], which is in good agreement with the experimentally observed melting point ($T_m^{expt} = 601\,K$).

Atomic equations of motion were integrated using time step $\delta t = 1$ fs. Initially, the equilibrium lattice constant for model Cu at T = 700 K was determined from simulations on a small fully periodic perfect Cu crystal in the NPT ensemble, where N is the number of atoms in the system and pressure p = 0. Substrates were then formed with either the (001) or (111) crystallographic direction along z and approximate dimensions as given in the preceding paragraph; these were equilibrated as fully periodic crystals in NVT ensembles with volume V determined by the previously determined equilibrium lattice constant. After the bulk equilibration runs, periodicity along z was removed, revealing two free surfaces for each substrate; in both cases, the lower surface (in z) was constrained against relaxation by holding 6 layers of atoms at that surface rigid for all subsequent calculations. This prevents substrate translation while also modeling a transition to bulk crystal with increasing depth into the substrate. Given this constraint of the lower free surface, the rest of the substrate atoms were then allowed to relax in response to the upper free surface formation in an isothermal T = 700 K simulation; during this and all following simulations, the dimensions in x and y were fixed to values given by the bulk equilibrium lattice constant. After equilibrating the free surface substrate systems, they were merged with drops for wetting simulations as described below.

Cylindrical drops were formed by first determining the equilibrium liquid Pb density in the NPT ensemble with T = 700 K and p = 0. Subsequent to this, two Pb bulk liquid systems were formed as follows. The dimensions of each liquid in y ( i.e. $l_y$ , what will be the length along the cylinder axis direction) are held fixed at values determined

by the corresponding substrate dimension in y. The x and z dimensions are made equal to each other and are determined by the equilibrium density; however, N was made large enough to ensure that the systems are sufficiently large at equilibrium to permit extraction of the largest drop desired, $R_0 = 22.6\,nm$. The bulk liquids so formed are relaxed in NVT simulations; following these, a cylinder of chosen $R_0$ is extracted from the liquid and run with T = 700 K to permit relaxation after free surface formation ($R_0$ values reported here were determined after this step to account for any surface relaxation upon free surface formation). Each drop is then merged with its corresponding substrate in a common simulation space. To eliminate the influence of impact velocity, drops are inserted into the simulation space above the substrate free surface such that the closest Cu/Pb interatomic distance at time $t = 0$ is equal to the Cu/Pb layer spacing observed in planar solid/liquid interface simulations. [81] The starting velocity distribution for atoms in drops were such that T = 700 K but the center of mass linear and angular momentum were zero for all drops upon merging. Substrate atoms were also given an initial velocity distribution corresponding to T = 700 K.

All subsequent behavior between drop and substrate was dictated by the MD equations of motion in conjunction with the utilized interatomic potential. However, the isothermal ensemble utilized was implemented so as to avoid any influence on atomic velocities for droplet atoms as well as atoms in the near surface region of the substrate. Because thermostat algorithms directly affect atomic velocities during MD simulations, it is important to ensure the algorithm does not influence fluid mechanics inherent to spreading. To achieve this, only substrate atoms more than 0.5 nm away

from the free surface were subject to the temperature control algorithm; the time constant used in the thermostat algorithm was equal to $1000\delta t$ to achieve aggressive temperature control for those atoms. In this way, the droplet temperature did not deviate from T =700 K by more than $\sim$ 7% during spreading simulations.

Liquid layering near the solid surface in this model of the Pb/Cu system has been presented previously for both a spreading geometry as well as for planar solid/liquid interfaces [41], [81]. Density analysis along the solid free surface normal showed that, during spreading on both (001) and (111), three Pb(l) layers are distinct with a fourth less distinct; the layer spacing normal to the solid free surface was 0.29 nm [41]. Because of this, when computing x(t) for simulations presented here, the systems were divided into analysis slabs along the z direction where the analysis slab thickness was equal to the liquid layer spacing near the solid free surface. The analysis slabs, or layers, were defined such that the lowest three (in z) each contained one of the three liquid layers near the solid surface; seven additional analysis layers were defined for increasing distance from the solid surface (up to ~ 3 nm above the surface). At any instant in time and for each analysis layer, x(t) was determined from a number density analysis in the x direction over atoms in the given layer. While it is intuitive to define x(t) based on the spatial (i.e. x direction) extent of 100% of the atoms in a layer, this can manifest outlier data points if, for example, a single atom detaches from the wetting front and diffuses ahead on its own. Thus, it is numerically advisable to consider the maximum extent in x of, say, 99% of atoms in a given layer; though this is somewhat heuristic, it does not influence conclusions reached here.

To establish some familiarity with the execution of atomic scale simulations of inertial wetting, the procedure used here is discussed. However, in this section, an attempt is made to minimize provided detail to only information necessary to interpret presented results. Despite using a different model of atomic interactions here as compared to, e.g., Ref. [39], most of the presented methodology is quite similar to what has been done in other studies.

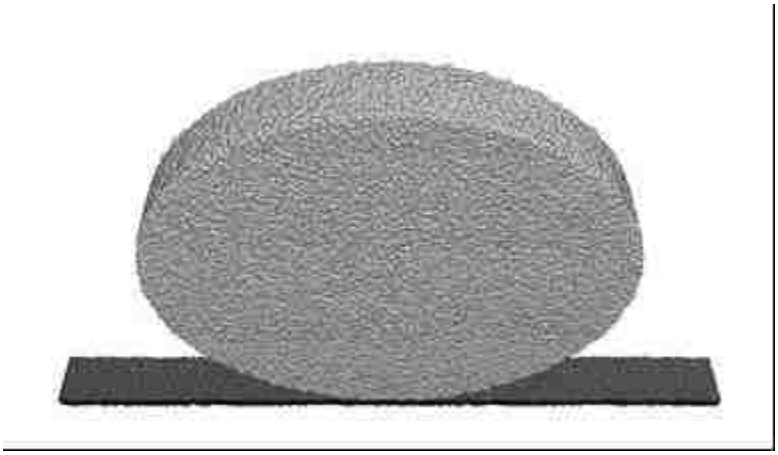

**Figure 4-1:** A perspective view of one of the simulations at time $t = 0$ (Pb droplet atoms are light; Cu substrate atoms are dark). The image is for a $R_0 = 20.8\,nm$ drop in contact with the (001) surface of Cu. The spreading direction is x, the free surface normal direction is z, and the droplet cylindrical axis is along y. Only substrate atoms within 1 nm of the free surface are rendered; in addition, only a portion of the substrate in x is rendered.

While fully 3D simulations are utilized throughout the current work, the geometry explored is wetting of a Pb(l) cylinder on low crystallographic index surfaces of a face centered cubic single crystal Cu substrate; the free Cu surfaces studied are (001) and (111) and the free surface normal is along z (see Figure 4-1). Periodic boundary conditions are applied in the cylinder axis direction (y) as well as the spreading direction (x). Periodicity is enforced along x to avoid free surface relaxation effects at the edge of the substrates (in x). Herein, the liquid cylinder is often called a drop for brevity; starting

drop radii in the range $R_0 = 2.6\,nm$ ($Re_c = 4$) to 22.6 nm ($Re_c = 35$) are studied. Typical dimensions for substrates modeled here are $\sim 120$ nm in x, $\sim 5$ nm in y, and $\sim 5$ nm in z; the two largest drop sizes studied required substrates with larger dimension in x ($\sim 240$ nm). Because substrate dissolution into the spreading liquid is negligible, a small dimension in z can be used; additionally, the use of a liquid cylinder geometry permits a relatively small dimension in y. These attributes of our simulation geometry combine to constrain simulation sizes to a maximum of order one million atoms, making them amenable to relatively commonplace computational resources. This same geometry has been used in prior simulations of inertial wetting [18], [36].

Relevant properties of the bulk liquid state as predicted by this model were calculated. For the simulated $T = 700$ K, the interaction model used gives a liquid with viscosity $\mu = 2 \pm 0.2$ mPa · s, surface tension $\gamma = 0.574 \pm 0.038\ J/m^2$, and density $\rho = 10688 \pm 220\ kg/m^3$. Note that all quantity ranges and error bars provided in the present work represent 95% confidence intervals as defined via standard statistical sampling practices. The viscosity and density were determined from equilibrium MD simulations of a three dimensional periodic (i.e. bulk) liquid in the NVE ensemble using a simulated Pb(l) system that had been previously equilibrated to p = 0 density for T = 700 K. Viscosity was computed via Green-Kubo relations with sufficient ensemble averaging to achieve an acceptable error in the predicted quantity [68]. Surface tension was computed from a simulation on a Pb(l) slab (i.e. two free surfaces in z) using the difference between the normal and transverse components of the pressure tensor [82].

Given the wetting geometry simulated, the distance that the liquid front advances across the substrate is designated $x(t)$; an alternate way to characterize wetting kinetics is through the time evolution of the contact angle $\theta(t)$ and this was computed via the slope of a linear fit to data for $x(t)$ versus height above the solid surface. Because two distinct contact lines advance across the surface in each simulation, results for $x(t)$ and $\theta(t)$ are averaged over both contact lines. Droplet flow velocity profiles were computed during inertial spreading simulations; because of the flow geometry, this analysis was performed by collapsing data for all atoms into the $x/z$ plane. At any instant in time, all droplet atoms were assigned to analysis bins according to their simulation x and z coordinates; the size of analysis bins in the $x/z$ plane could be changed to alter spatial resolution. The smallest bin edge dimension used was equal to the spacing between liquid layers that were observed to form near the solid surface. The lower bound for all analyses (in z) was defined to coincide with the lower bound of the liquid layer closest to the solid; in this way, transport in individual liquid layers nearest the substrate could be isolated from transport in other regions of the drops. In other cases, more coarse grained flow data were generated using analysis bins with edge dimension equal to eight times the minimum size. Velocity for material in a given bin was computed by first calculating the center of mass in the bin. After a short subsequent period of simulation (0.01 ns), all atoms that were in a given bin were again located and that group of atoms' new center of mass was computed. This provided the average displacement (and velocity) of fluid in a given bin.

## 4.2 Particle Suspension Models and Force Computation Method

MD simulations employed embedded atom method [8] interatomic potentials for describing interactions between liquid Pb and solid Cu (both suspended particles and substrate surfaces were modeled to be Cu); specific potentials used to describe Cu-Cu, Pb-Pb, and Cu-Pb interactions were previously advanced and have been demonstrated to describe this material system with very good accuracy [8], [41], [75], [76]. Nonetheless, rather than to connect with a specific material composition, the Cu-Pb system was chosen here based on more general attributes of metallic systems, as described in the preceding section. Liquid metals modeled via EAM potentials typically exhibit relatively high surface tension $\gamma_{lg}$and low viscosity η, in accord with experimental observations on these materials. These quantities were previously computed for the model of Pb(l) used here and at the same T = 700 K as is modeled here; they are $\gamma_{lg} = 0.574 \pm 0.038\, J/m^2$ and $\eta = 2 \pm 0.2\, mPa \cdot s$ [83].

This system was additionally chosen as prior studies have revealed interesting wetting behavior for Pb(l) drops on Cu. Despite identical chemistry, both the advancing contact line morphology (i.e. $\theta_{adv}$ ) and the advancing contact line velocity differ significantly for Pb(l) wetting Cu(001) versus Cu(111). Lower and higher spread velocity are observed on Cu(111) and this is most evident during inertial stage wetting [41], [83]. Thus, this system provides an opportunity to examine the role of on determining likelihood for self-pinning. Experimentally, this system has been found to be partially wetting; on polycrystalline Cu surfaces the equilibrium contact angle was observed to vary with T from $\theta_0 = 45°$ at T = 600 K to $\theta_0 = 20°$ at T = 1000 K [83]. Prior

simulation studies using the Pb/Cu model used here showed that, for T = 700 K, $\theta_0 = 30°$ on Cu(001) and $\theta_0 = 20°$ on Cu(111) [41]. In both experiments and simulations, an atomically thick precursor film was observed to spread ahead of advancing droplet contact lines. A potential drawback to studying wetting in metal systems is that many such chemical combinations exhibit some form of reactive wetting where the chemistry and/or morphology of the solid/liquid interface change with time. However, in agreement with experiment, Pb and Cu in this model are relatively immiscible; thus, solid/liquid interfaces in the model remain relatively sharp.

Figure 4-2 shows two views of a typical simulation configuration at time t = 0. Fully three dimensional simulations were employed throughout; however, to reduce the spreading geometry to two dimensions, liquid cylinders were brought into contact with solid surfaces where the length of the cylinder along its axis (i.e. in the y direction) was identical to the periodic dimension of the simulation cell along y (the same was true for the solid surface). Thus, two independent contact lines advanced in positive/negative x and results were averaged along y to collapse spreading analyses into the xz plane. Despite this being a model of an infinite length liquid cylinder, the relatively small periodic dimension of the simulation cell along y suppressed Rayleigh instabilities in the liquid while also reducing computational cost and permitting study of relatively larger drops. Suspended nano particles were also cylinders, akin to what was done with the liquid drop (see below). Note this is different from recent simulations that also employed cylindrical drops but spherical particles [62]. Here, both spreading and pinning were effectively reduced to 2D processes, explored via 3D simulation ensembles.

All results presented here were from isothermal ensembles with $T = 700$ K, which is $\sim 10\%$ greater than the liquid melting point and just over half the solid melting point. Simulation time step throughout was 1 fs and the MD code LAMMPS was used for all simulations [80]. Cu substrates modeled were subject to periodic boundary conditions in x and y with the periodic repeat length of the simulation cells $L_x \sim 300$ nm and $L_y \sim 5$ nm. Solids were initially equilibrated in fully three dimensional periodic ensembles at the zero pressure lattice constant and with appropriate unit cell rotation to have either the Cu(001) or Cu(111) direction along z. For all equilibration runs, the system was identified to be at equilibrium via temporal analysis of potential energy, pressure, and other system properties. Following the initial bulk solid equilibration, periodic boundary conditions were removed along the z direction, forming two free surfaces for each Cu substrate. Substrates had thickness in z equal to 5 nm, with ~1 nm of thickness at the free surface in negative z held rigid for all subsequent calculations. Since $L_y$ was dictated by the solid substrate lattice constant and the crystallographic surface orientation, this dimension differed a small amount for (001) versus (111) substrates.

Three dimensional periodic slabs of liquid were equilibrated at the zero pressure density for the desired T. To reach proper liquid density during equilibration runs, $L_x$ and $L_z$ were allowed to vary while $L_y$ was constant as given by the corresponding substrate's $L_y$. After liquid slab equilibration, cylinders (with cylindrical axis along y) were extracted from the atomic ensembles and re-equilibrated in free space. Two separate drops were thus formed with nominally identical properties but slightly different $L_y$.

Following liquid drop equilibration in free space, the radius of cylindrical drops was determined from plots of number density as a function of radial distance from the cylindrical axis, averaging all data along the cylinder axis in y ; the radius was defined as the point on the radial density profile where the plot decreased to half the average density in the bulk liquid. The initial droplet radius was $R_0 = 42$ nm in all cases studied here; particle insertion into the drops and subsequent re-equilibration (described below) did not change $R_0$ for particle concentration explored here.

To maintain a three dimensional simulation geometry but with both spreading and pinning effectively reduced to two dimensional processes in the xz plane, cylindrical particles were inserted into cylindrical drops. A feature unique to studying self-pinning in an effectively 2D geometry is that a single particle entrained into the contact line has the capability to drive self-pinning. A cylindrical 'particle' was initially extracted from a solid slab used to form a Cu substrate. The nominal extraction radius was $\leq 3$ nm; copies of this model particle were then inserted into the drop in multiple, random locations. Insertion was done so as to ensure that all atoms in a given inserted particle were outside the interaction range of atoms in other particles at $t = 0$ ; furthermore, particles inserted near the drop edge were required to be at least $75\%$ inside the drop. To insert a particle, a cylinder of liquid atoms was extracted from the drop using a radial cut-off around the determined insertion point; the cut-off was chosen to ensure that, upon merging a copy of the particle into the drop, the closest separation distance between a drop atom and a solid particle atom was equal to the equilibrium separation distance observed at planar solid/liquid interfaces for this system. After the desired number of particles was inserted,

nanosuspension drops were re-equilibrated in free space. Within a few tens of ps after starting these simulations, a very small number of particle atoms dissolved into the liquid as initially cylindrical particles rapidly developed facets on low index crystallographic planes. Equilibration of nanosuspension drops was thus relatively quick, relative to simulation time scales. After faceting, following equilibration, particle radius was $r \leq 3$ nm. For results here, either 10 or 20 particles were inserted giving volume percent loadings $\emptyset \sim 4\%$ and $\emptyset \sim 8\%$, respectively. For each case studied, the same (pseudo) random positions were used for particle insertion in both drops. Thus, nominally identical, equilibrated nano suspension drops were prepared for joining with either a Cu(001) or Cu(111) substrate. Spreading simulations were also run for drops with no suspended particles.

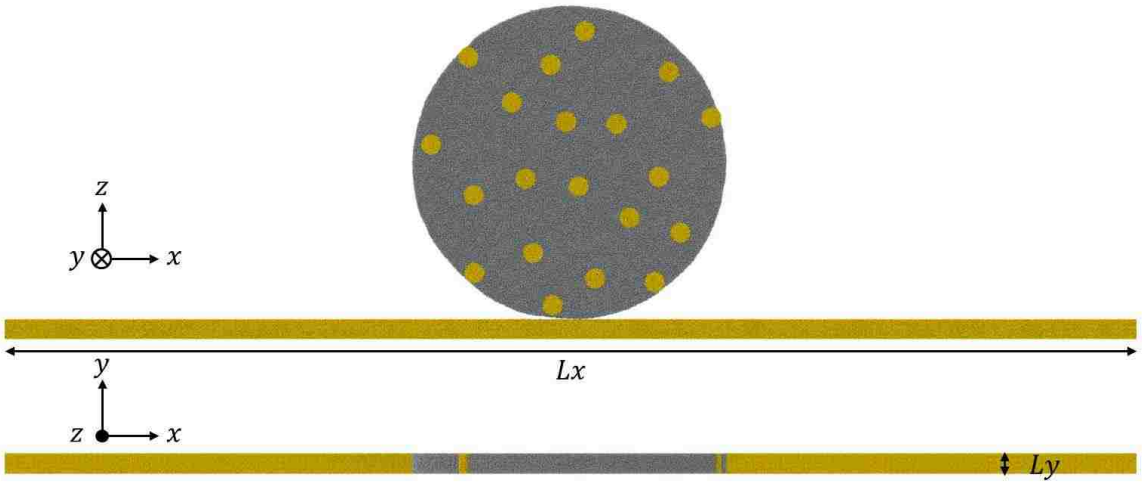


**Figure 4-2:** Two orthographic projection views of a simulation configuration at time t=0 (Pb atoms are in dark grey; Cu atoms are in yellow). The image is for a $R_0 = 42$ nm drop with 20 Cu particles in contact with the (001) surface of Cu. The spreading direction is x, the free surface normal direction is z, and the droplet cylindrical axis is along y. The periodic repeat lengths of the simulation cells shown are $L_x = 300$ nm and $L_y = 5$ nm.

Following a drop's equilibration, it was merged into a simulation cell with the desired substrate for subsequent wetting simulations. Drops were inserted adjacent to substrates in positive z such that the closest distance between a drop atom and a substrate atom at $t = 0$ was equal to the equilibrium separation distance observed in planar solid/liquid interface simulations. To maintain isothermal spreading, substrate atoms at least 1 nm from the wetted surface were subject to a thermostat algorithm (excluding rigid substrate atoms at the inactive free surface); all other dynamic atoms were integrated in a constant energy ensemble. This prevented the thermostat algorithm from altering flow behavior in the spreading drops. It was verified that T throughout the drop and substrate (and for all time simulated) did not deviate from $T = 700$ K by more than $\sim 15$ K.

To characterize wetting kinetics the extent of drop spread in x was computed for both advancing contact lines, averaging all data along y . This was done also as a function of distance from the solid free surface into the drop so that kinetics of precursor wetting films were distinguished from droplet wetting kinetics. The specific method for computing droplet $x(t)$ for varying height above the substrate has been presented previously [83]; in the absence of particles, this method also permits straightforward computation of dynamic contact angle $\theta(t)$. The presence of particles entrained to the contact line complicates the computation of both $x(t)$ and $\theta(t)$ because it is more challenging to define the edge of the liquid front; this will be discussed further below. To characterize flow in drops, velocity vector profiles were computed by assigning atoms to bins according to an atom's xz coordinates at a given t ; bins were 1 nm on edge and

spanned the system in y . After 10 ps, the xz coordinates of all atoms that were in a given bin were used to compute the aggregate center of mass displacement (and velocity) for that bin; this analysis time was chosen somewhat heuristically and it balanced a desire for high temporal resolution with a need for sufficient time passage to give definitive results for flow velocity.

## 4.3 Justification on Simulation Geometry

In both pure droplet spreading and nano-suspension simulations, cylindrical geometry has been utilized on Pb droplets and Cu nanoparticles. Notably, I performed fully 3D simulations here i.e., we explored via 3D simulation ensembles since using realistic material models in atomic scale MD simulations requires 3D simulations; however, the droplet and particle geometry maintained all analyses of spreading to two dimensional activities. Therefore, we have a pseudo 2D geometry and those extracted atomistic details of spreading data are analyzed in the x/z plane.

A feature unique to analyzing self-pinning in an effectively 2D geometry is that a single particle entrained into the contact line has the capability to drive self-pinning. However, by using cylindrical geometry which is different from the realistic case involving spherical geometry, particle patterning and packing effect at contact lines could not be examined by using this pseudo 2D geometry. Meanwhile, droplets spread in the absence of vapor pressure throughout all the wetting simulations, which is different in some real systems where there exists significant vapor pressure.

# 5 Mechanism of Rapid Contact Line Advance

The choice to model wetting of Pb(l) on different crystallographic surfaces of Cu permits exploration of inertial wetting for a system where the solid and liquid chemistry remain unchanged; yet, the inertial spreading rate and droplet morphology are quite different based on whether spreading occurs on the Cu(001) or Cu(111) surface. This is clearly exhibited in Figure 5-1 and Figure 5-2, which show a droplet ($R_0 = 20.8\,nm$) spreading during the inertial regime on Cu(001) and Cu(111), respectively.

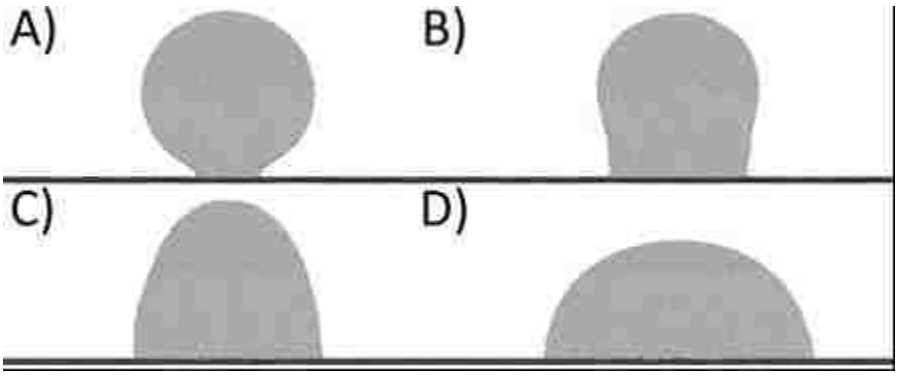


**Figure 5-1:** Images of wetting simulations for a Pb(l) drop ($R_0 = 20.8\,nm$) on Cu(001) at varying time; a) t = 40 ps, b) t = 200 ps, c) t = 400 ps, and d) t = 800 ps. Light (dark) atoms are Pb (Cu). Note the times shown are 0.1, 0.5, 1, and 2 times the inertial/capillary scale (see text).

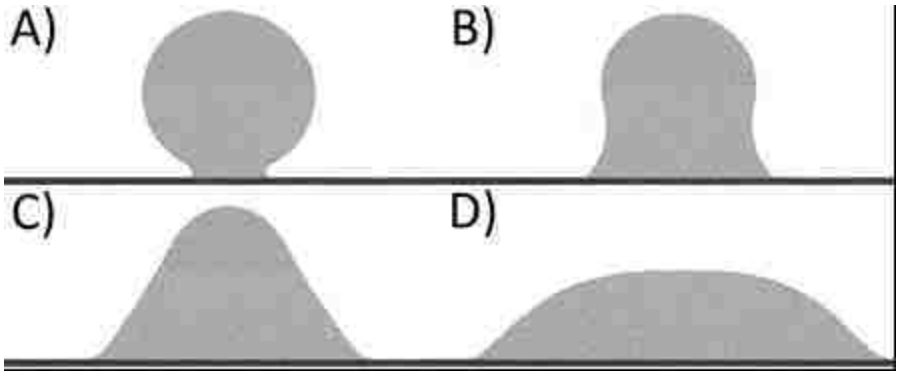


**Figure 5-2:** Images of wetting simulations for a Pb(l) drop ($R_0 = 20.8\,nm$) on Cu(111) at varying time; a) t = 40 ps, b) t = 200 ps, c) t = 400 ps, and d) t = 800 ps. Light (dark) atoms are Pb (Cu).

Images in Figure 5-1 and Figure 5-2 illustrate that the droplet morphology changes dramatically during the inertial stage of spreading; furthermore, inertial spreading manifests differently on the Cu(001) surface, compared to the Cu(111) surface. For the former, the drop reaches a contact angle $\theta \sim 90°$ after $0.2 - 0.4$ ns; following this, $\theta$ decreases relatively slowly through the remaining duration of inertial spreading. The contact angle on Cu(111) decreases more significantly in the first 0.4 ns, $\theta \sim 50°$; beyond that point in time, $\theta$ decreases relatively slowly, as it did on Cu(001). For both systems, the droplet height above the substrate changes relatively little during the first 0.4 ns, which results in morphologies quite distinct from a cylindrical cap. Between 0.4 ns and 0.8 ns the height decreases and the final images in both cases show liquid/vapor interfaces that are well described via a cylindrical cap approximation (but with different contact angles). For the earliest moments of inertial wetting on Cu(111), the maximum contact line velocity observed for this $R_0$ is $v \sim 150$ m/s; the total extent of spread during the inertial regime divided by the inertial regime

duration gives $v_{avg} \sim 50\, m/s$ on Cu(111). For inertial spreading on Cu(001), the velocities obtained were consistently ~ 60% of those on Cu(111).

To collapse inertial regime spreading data for varying droplet size, it is common practice to scale time by the inertial/capillary time scale T; for a spherical drop, $T \sim \sqrt{\rho R_0^3/\gamma}$. This results from treating the drop as a mass proportional to the numerator in the radical; dynamics of this mass are governed by a spring with stiffness γ, giving the relevant time scale T. [84] Under this approach, the relevant mass for a cylindrical drop scales as $\rho R_0^2 l_y$, where $l_y$ is the length of the cylinder along its axis (i.e. the length of the periodic y dimension in our simulations); thus, one might expect the inertial/capillary scale for a cylindrical drop to be $T_{cyl} \sim \sqrt{\rho R_0^2 l_y/\gamma}$. For one value of $R_0$ simulated here, a wetting simulation was repeated with $l_y$ four times the original case. In that case, x(t) data were nearly identical in the inertial regime to the original case, showing no dependence on $l_y$ for either the duration of the inertial regime or the rate of spreading during this regime. This is reasonable given that the mass of a cylindrical drop scales linearly with $l_y$ but so too does the driving force for inertial spreading (i.e. capillary pressure manifests along the entirety of the contact line). We thus disregard any disconnect between the cylindrical drops studied here and the mass term in the numerator of $T \sim \sqrt{\rho R_0^3/\gamma}$ and compute T for drops simulated here. For $R_0 = 20.8\, nm$, T = 0.41 ns; thus, images presented in Figure 5-1 and Figure 5-2 are for $t_s = \frac{t}{T} = 0.1, 0.5, 1\ and\ 2$.

From the earliest moments of solid/liquid interface formation, atoms in the liquid nearest the solid free surface form well defined layers as they spread across the solid surface. Prior research examining spreading of Pb(l) on Cu revealed that on both Cu(001) and Cu(111) the first two layers of Pb(l) atoms form a precursor wetting film that fully wets the surface; in addition, kinetics of the precursor advancement on Cu(111) are much more rapid than on Cu(001) [41]. In the final time image in Figure 5-2, the two layer precursor film on Cu(111) is just beginning to distinguish itself from the bulk drop; this is not so for the final time image on Cu(001) in Figure 5-2. During inertial spreading on Cu(001), the precursor film is indistinguishable from the bulk drop; the same is approximately true for inertial spreading on Cu(111).

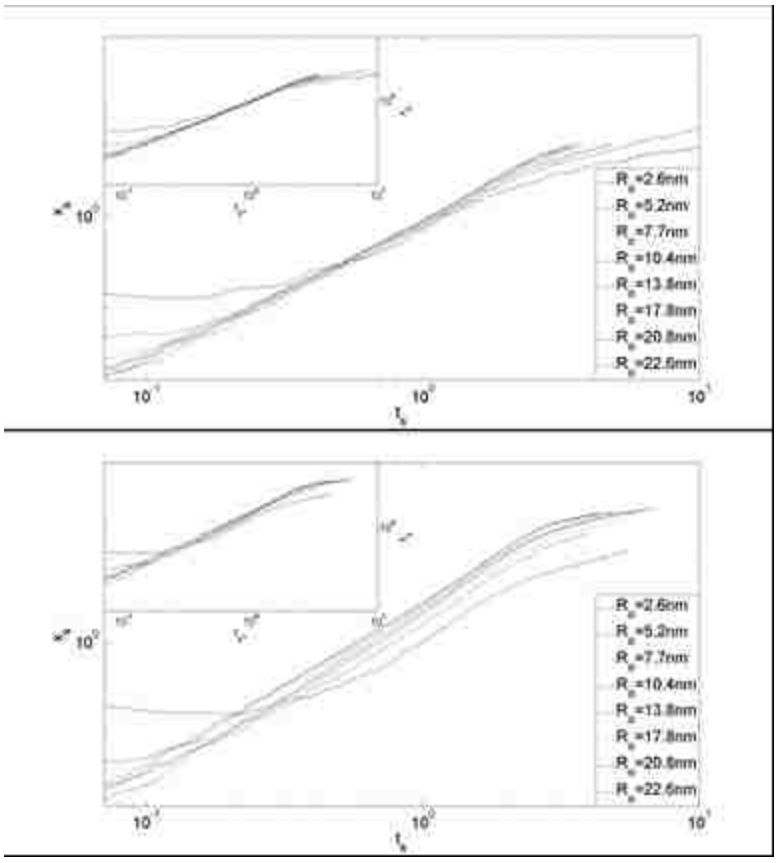


**Figure 5-3:** Extent of spread in x scaled by starting droplet radius $R_0$ versus time scaled by $\sqrt{\rho R_0^3/\gamma}$ (main panels); data are presented for Pb(l) drops on (top) Cu(001) and (bottom) Cu(111). Data from simulations for varying $R_0$ are presented. The inset to each panel contains the same data except that time has been scaled by $\sqrt{\rho R_0^3/\gamma^*}$ (see text).

Figure 5-3 shows x(t) data for different drop sizes on both Cu(001) and Cu(111); in the main panel, time axis data are scaled by T and x(t) data are scaled by $R_0$. The main panels in Figure 5-3 show that data scaling for spreading on Cu(001) is more satisfactory than for Cu(111); in addition, for both systems, the smallest drops simulated exhibit the largest deviation from a perfect collapse of data. This is the same discrepancy observed in Ref. [36] (discussed above). Furthermore, the largest drop sizes studied - on both surfaces - exhibit nearly ideal collapse of data upon scaling. The

smallest drops simulated here have $Re_c = 4$ so it is possible that viscous effects are the cause of observed deviations; however, as will be presented below, even the smallest drops here show good agreement with $R \sim t^{1/2}$ in accord with inertial wetting kinetics. We thus propose that a nanoscale size effect manifests for the smallest drop sizes studied here; because the magnitude of deviation for small drops is greater on Cu(111) than on Cu(001), it also appears that droplet size effects manifest differently on different solid surfaces. Given the direction of deviation for small drop data in Figure 5-3, one possibility is to consider a reduction in γ with decreasing $R_0$, driven by increasing surface curvature; the relevant length scale governing such effects is the Tolman length [85]. This approach was recently adopted to describe surface tension for simulations of nanometer scale bubbles [86]. Under such a treatment, surface tension for a drop with radius $R_0$ is described as

$$\gamma^* = \gamma \frac{R_0}{R_0 + 2\delta} \tag{5-1}$$

where γ is the surface tension for a planar liquid/vapor interface and δ is the Tolman length. For a liquid drop, δ is positive such that, for sufficiently small $R_0$, $\gamma^* < \gamma$. However, δ is related to the width of the liquid/vapor interface so it is expected that the Tolman length is of molecular scale, regardless of $R_0$. As such, for sufficiently large $R_0$, $\gamma^* \cong \gamma$. Here, δ is taken to be comparable to the liquid/vapor interface thickness as determined from radial density profiles on the largest drops simulated $\delta = 0.5$ nm; this is roughly equal to two times the Pb atomic diameter.

Using this δ for all $R_0$ simulated, time axis data are rescaled via $t_{s^*} = t/T^*$, where $T^* = \sqrt{\rho R_0^3/\gamma^*}$; the results are shown in the insets of Figure 5-3. Collapse for inertial spreading data on Cu(001) is now essentially ideal. Thus, a scaling factor derived from continuum considerations - once corrected for nanoscale variations in liquid/vapor surface tension - permits universal data collapse from macroscale drops down to drops that are only a few nanometers in radius. While collapse of data for inertial spreading on Cu(111) is now more satisfactory, deviations from universal collapse still exist and they show the persistent trend that the smallest drops exhibit the greatest deviation while data for the largest drops fall on a single curve. Thus, remaining deviations for Cu(111) data are driven by a size effect that is independent of curvature induced corrections to surface tension; mechanisms driving this additional size effect are explored below. Log-log presentations of spreading data reveal characteristic power law behavior $x \sim t^{\alpha}$ that persists over the inertial duration $t_i$. Beyond $t_i$, x(t) data in Figure 5-3 show a decrease in slope as evidence of transition from inertial spreading power law kinetics to some later time regime where other dissipation mechanisms dominate kinetics (e.g. as described in molecular-kinetic or hydrodynamic spreading theory). Figure 5-3 shows again what was observed above: inertial regime spreading involves very high contact line velocity in both systems; however, contact line velocities on the Cu(111) surface are higher than on the Cu(001) surface. For all $R_0$ on both Cu(001) and Cu(111), the duration of the inertial regime appears to be $t_i \sim 2T^*$.

Data in Figure 5-3 were analyzed by optimizing a fit of the form $x(t) = C_0 t^{\alpha}$ to data for $0.5T^* < t < 2T^*$. For Pb(l) drops on Cu(001), convincing evidence for

$x(t) \sim t^{1/2}$ is obtained: the average exponent from wetting simulations was $\alpha = 0.49 \pm 0.02$ (all ranges quoted and error bars presented here represent 95% confidence intervals). For Pb(l) spreading on Cu(111), simulations show a fairly consistent deviation from $x(t) \sim t^{1/2}$ in that $\alpha = 0.60 \pm 0.02$. It thus appears that Pb(l) drops spreading on the Cu(001) surface exhibit the widely observed low viscosity limit for inertial regime wetting wherein 'diffusive like' contact line motion is observed $x(t) = (Dt)^{1/2}$. For Pb(l) drops wetting the Cu(111) surface, however, a somewhat increased dependence upon time emerges. Prior work showed that a surface alloy phase forms between the layer of Pb(l) atoms closest to the Cu(001) free surface and the plane of Cu atoms at that free surface [41]. It is thus somewhat surprising that this system exhibits inertial regime spreading kinetics typical of non-reactive spreading systems. Closer examination, however, reveals that surface alloy phase formation rate is reduced by $\sim$ 75% during the inertial regime. This indicates that rapid, inertial regime spreading suppresses reaction kinetics, resulting in a system that behaves similarly to non-reactive systems. Note this relationship is essentially opposite to what was found for later time wetting kinetics in this system where prior studies showed that alloying acted to slow spreading kinetics during later stage wetting [41].

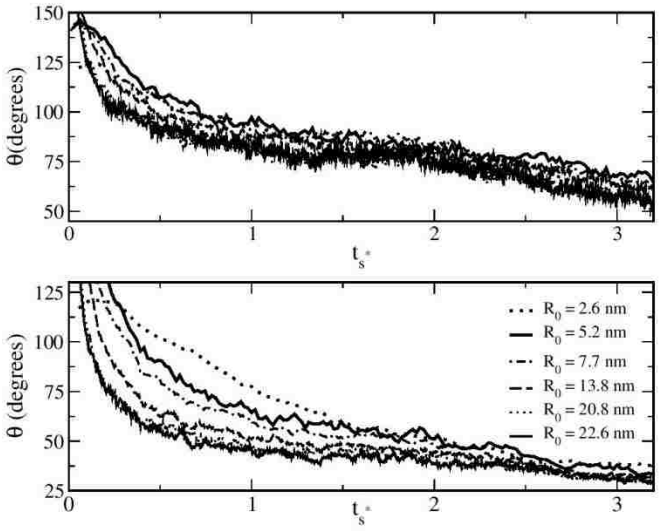


**Figure 5-4:** Contact angle versus time scaled by $\sqrt{\rho R_0^3/\gamma^*}$; data are presented for Pb(l) drops on (top) Cu(001) and (bottom) Cu(111). Data from simulations for varying $R_0$ are presented as given in the legend (the legend applies to both panels). Note that, for each panel, the extent shown in θ is the same but the bounds are different.

Figure 5-4 shows contact angle data plotted versus $t_{s^*}$ for varying $R_0$ on Cu(001) and Cu(111); time is scaled in a way that accounts for curvature driven changes to γ for very small drops. A general trend observed for both systems is that θ decreases during $0 < t_{s^*} < 1.4$; it does so relatively rapidly over the initial $\sim 0.4t_{s^*}$ and more slowly beyond that. After $\sim 1.4t_{s^*}$, θ stays roughly constant for the remainder of the inertial spreading regime; following the inertial regime, θ decreases further. Focusing on data for the larger drops sizes, inertial spreading on Cu(001) manifests larger advancing contact angle $\theta_{adv} \sim 80 - 90$ than is observed for Cu(111), $\theta_{adv} \sim 40 - 50$. On both surfaces, the apparent frequency in data fluctuations increases with $R_0$. However, this is an artifact produced by the time scaling; the actual frequency of statistical fluctuations in calculated

θ(t) showed no dependence on $R_0$. Distinct from the time scaling artifact, fluctuations in calculated θ for inertial spreading on Cu(001) are greater than for Cu(111). However, this is an artifact of how contact angle is computed; a linear fit is made to data for x(t) versus height above the surface and an arctan function converts the slope from the fit to an angle. The magnitudes of fluctuations in the slope data are similar for Cu(001) and Cu(111). Given the magnitude of fluctuations, $\theta(t_{s^*})$ data for inertial spreading on Cu(001) exhibit reasonably universal behavior across $R_0$. Alternatively, an obvious size effect is observed for inertial spreading on Cu(111) in that smaller drops exhibit increased θ(t) throughout much of the inertial regime. Furthermore, the size effect appears to be diminishing with increasing $R_0$ and nearly gone for the largest systems modeled here. This is related to the observation in Figure 5-3 that scaling time by $T^*$did not achieve universal scaling of x(t) data for Cu(111).

Results so far presented illustrate that, once curvature driven changes to surface tension are accounted for, all data for inertial spreading on Cu(001) are well described by continuum derived inertial wetting theory for low viscosity liquids, even down to drops with less than 3 nm radius. The same cannot be said for inertial spreading on Cu(111) where an additional size effect manifests. To understand its origin, it is first useful to elucidate why fits to data in Figure 5-3 for Pb(l) drops spreading on Cu(111) consistently give a power law with exponent greater than 1/2. As described above, for this system, $x(t) \sim t^{0.6}$ and this discrepancy is statistically significant. Inertial spreading on Cu(111) must therefore exhibit behavior unique from inertial spreading on Cu(001) that drives an increased dependence on time in the kinetic

power law. Since the additional size effect seen in x(t) and θ(t) data is also unique to inertial spreading on Cu(111), its origin may be related to phenomena causing a change in kinetic power law. Note that inertial regime spreading kinetics for low viscosity, non-spherical drops also exhibit $R \sim t^{\alpha}$ with $\alpha > 1/2$; specifically, for inertial spreading of conical drops, the power law exponent obtained was 2/3, rather than 1/2 [27]. Further, it was shown that the shape effect could be captured in the contact line equation of motion via an exponent parameter β,

$$x(t) \sim \left(\frac{\gamma R_0^{\beta-1}}{\rho}\right)^{1/(\beta+2)} t^{2/(\beta+2)} \tag{5-2}$$

The parameter β is essentially a description of curvature in the advancing liquid front such that, for spherical drops, β = 2, leading to $x(t) \sim t^{1/2}$. For conical drops, β = 1, leading to $x(t) \sim t^{2/3}$ [32]. The 2/3 power law has also been predicted by analytical treatments of inviscid flow into an advancing wedge shaped region [49]. Significant droplet distortion is shown in Figure 5-2 during inertial spreading on Cu(111). Starting very early in the inertial regime, $\theta_{adv}$ for this system is significantly less than 90°, characteristic of a wedge shaped advancing contact line region; Figure 5-4 further bears this out. Given this, it is possible that, for inertial spreading on Cu(111), $1 < \beta < 2$, leading to kinetic behavior observed here. However, it should be highlighted that droplet shapes in Ref. [32]were distorted from circular at the start of spreading and the distortion was achieved via ionic effects. Here, simulations are ideally absent of ionic effects and the starting droplet shape (in cross-section) is circular; thus, shape effects are dynamic in that they manifest during the earliest stages of inertial spreading.

Data obtained for the power law exponent show no dependence on $R_0$ in the range studied here; we thus predict that the change in exponent for the x(t) power law relationship for inertial spreading on Cu(111) is not a nanoscale effect. This is because the increased exponent is at least partly attributed to the wedge shape of the advancing contact line on this system. Even for macroscale drops, the structure of the contact line region is sensitive to behavior on molecular length scales; thus, it is expected that macroscale Pb(l) drops on Cu(111) will experience an advancing contact angle well below 90° during inertial spreading. In fact, data in Figure 5-4 show that the largest drops on Cu(111) reach the lowest values of $\theta_{adv}$ during the inertial regime and they do so most quickly. We therefore predict that inertial spreading kinetics for macroscale drops on Cu(111) are well described by Eq. (5-2) with $1 < \beta < 2$. Here again, kinetic expressions developed from continuum considerations are demonstrated to extend robustly across droplet size, down to the nanoscale regime. While we do not believe the change in exponent to be a nanoscale effect, it appears that the wedge shaped contact line associated with the higher power law exponent is the source of the additional size effect in this system.

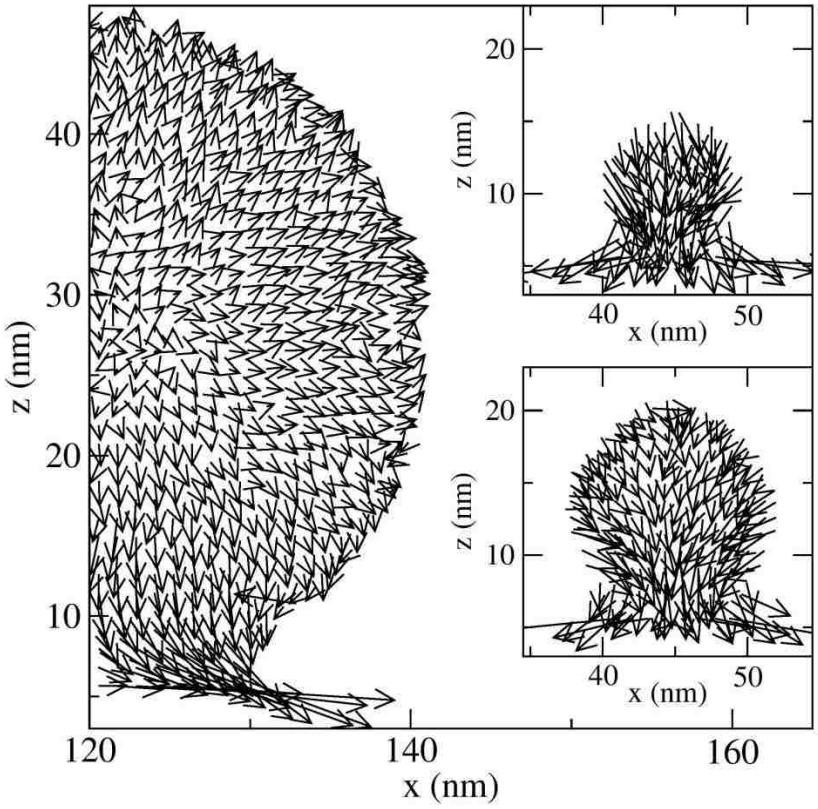


**Figure 5-5:** Flow velocity in the x/z plane inside Pb(l) drops during early stages of inertial spreading on Cu(111); the time shown in each case is t = 0.1 $T^*$. The insets show data from the entire drop; the top inset is for $R_0 = 5.2\ nm$ and the bottom is for $R_0 = 7.7\ nm$. The main panel shows data from one half the drop (in x) for $R_0 = 20.8\ nm$. All velocity vectors have been similarly normalized and the largest vectors shown correspond to velocity of order 130 m/s. Each vector represents an analysis volume that is 1.16 nm on edge in x/z and spans the simulation cell in y.

The low advancing contact angle and concomitant wedge shape for inertial spreading on Cu(111) are driven by the aggressive spreading kinetics for the precursor film in this system [41]. Figure 5-5 shows flow velocity for very early during the inertial regime on Cu(111) and for varying $R_0$. The point in (x,z) of initial droplet/substrate contact is (120 nm, 5 nm) for the main panel data and (45 nm,5 nm) for inset data. Data presented are from early in the inertial regime when contact line velocity is near its highest values observed. Results in Figure 5-5 help illustrate that the additional

nanoscale size effect for inertial wetting on Cu(111) is due to aggressive precursor film advancement. For the smallest drops studied here, the volume of material in the precursor film is a non-trivial fraction of the total droplet volume; as a consequence, flow of droplet material into the growing precursor film induces flow throughout the drop. This, in turn, involves a greater degree of liquid/vapor interfacial distortion, enhancing dissipation. For larger drops, the precursor film volume is small compared to the total drop volume and flow fields can be observed to interact with free surfaces less than for smaller drops. Flow fields in Figure 5-5 also explain the dependence of $\theta_{adv}$ on $R_0$ that was observed in Figure 5-4 for inertial spreading on Cu(111). For large drops on Cu(111) the precursor film acts to reduce $\theta_{adv}$ to less than $50°$; for the smallest drops simulated here, flow required to advance the precursor film and reduce $\theta_{adv}$ to the value observed for larger drops entails significant curvature gradients along a majority of the liquid/vapor interface. Thus, resistance is greater and so is the observed $\theta_{adv}$ for smaller drops. To estimate $R_0$ for which this size effect becomes negligible, we consider the relevant length scale; as an example, for curvature induced changes to surface tension, the relevant length scale was two times the Tolman length. This second size effect is due to curvature gradients manifesting over a majority of the liquid/vapor interface; thus, the relevant length scale is related to the extent of curvature gradients. This, in turn, is related to the thickness of the precursor film, 0.6 nm. Since this is comparable to the Tolman length, a conclusion can be advanced that, for $R_0 \geq 100\ nm$, all nanoscale size effects are negligible for inertial wetting of Pb(l) on Cu.

As previously mentioned, for all systems studied, $t_i \sim 2T^*$. A rigorous comparison of $t_i$ for varying $R_0$ shows that the duration of the inertial regime for Pb(l) drops is, within statistics, the same on Cu(001) and Cu(111). This is particularly notable because drops on these two surfaces exhibit different morphologies and contact angles throughout most of the inertial regime; they also exhibit a different power law exponent. Thus, for the system presented, the inertial regime duration $t_i$ appears to depend very little on the specifics of the spreading morphology or kinetics but instead seems to be dictated by properties intrinsic to the drop only; other authors have reached similar conclusions [18]. Some authors have advanced that $t_i$ can be understood in terms of the dispersion relation for pure capillary waves: $\omega^2 = \gamma k^3/\rho$, where ω is angular frequency and k is wave number. With k = 2π/λ ( λ is wavelength ) and ω = 2π/τ (τ is period), this gives $\tau^2 \sim \rho\lambda^3/\gamma$. In Ref. [87], it was assumed that the inertial regime duration scales directly with the longest capillary wave period $t_i \sim \tau_{max}$ and that the corresponding largest wavelength scales with the starting radius of the drops $\lambda_{max} \sim R_0$. This gives $t_i^2 \sim \rho R_0^3/\gamma$ or $t_i \sim T$. This rectifies a discrepancy mentioned earlier between the cylindrical drops studied here and what was previously referred to as a mass term in the numerator of $T^* = \sqrt{\rho R_0^3/\gamma^*}$. It is now seen that the relevant $T^*$ expression remains unchanged for cylindrical drops because this is reflective of the capillary wave dispersion relation. We highlight, however, an observation from Ref. [87]: in making the assumption that the largest wavelength scales with the starting radius of the drops, we disregard the fact that, during inertial spreading, the liquid/vapor interface is growing; thus, $\lambda_{max} \sim R_0$ may be too

simplistic an assumption. Factors dictating $t_i$ thus remain somewhat unclear but the most compelling observation is that $t_i$ is nearly identical for the two solid surfaces, despite fairly different inertial spreading behavior being exhibited on each surface. Given the high surface tension to viscosity ratio for the liquid modeled here, it is reasonable to suspect that capillary waves play a role in determining $t_i$.

It is satisfying that, once nanoscale size effects are properly accounted for, all results presented for inertial spreading of nanoscale droplets can be interpreted in terms of theory developed from continuum fluid mechanics. This provides great confidence that mechanisms of contact line advancement for simulated nanoscale droplets can be used to understand how contact lines advance for macroscale droplets; this seems particularly true for the largest drops simulated here. Flow illustrated in Figure 5-5 for inertial spreading on Cu(111) exhibits high lateral velocities for the lowest analysis volume bins (i.e. liquid moving, or slipping, along the substrate surface). It is this rapid surface transport of liquid that facilitates the very high contact line velocities associated with inertial spreading. In a recent investigation of inertial spreading, it was pointed out that the mechanisms by which such velocities manifest remain unknown [32]. It is well accepted that large capillary pressure in the liquid near the contact region is the driving force for rapid contact line advancement during inertial spreading. However, it is less clear how details of the solid/liquid interface abet the significant slip required to convert the driving force for inertial spreading into very high wetting velocities. Given an atomistic level of detail about the structure of the liquid film nearest the solid, simulations here can elucidate such mechanisms. Two questions, in particular,

seem pertinent: how is a liquid film undergoing a high rate of slip past a solid surface different from the same liquid in the bulk? Also, are observed characteristics for such a film in motion different from what is observed for a film of liquid adjacent to a solid surface but not undergoing slip?

Solid/liquid interfaces for this system were explored extensively in Ref. [81], albeit for equilibrium interfaces at $T = 625$ K, which is much closer to the melting point than $T = 700$ K explored here. Nonetheless, it is notable that prior work demonstrated a 'prefreezing' layer of Pb atoms forms in the layer directly adjacent to the Cu(111) surface. Density profile analysis showed the first layer of Pb atoms adopted a structure with peak number density approximately five times the bulk Pb(l) density, indicating significantly enhanced structural ordering for liquid atoms at the solid/liquid interface. Though unable to adopt to the substrate epitaxy, Pb atoms in the prefreezing layer were observed to adopt closer nearest neighbor bond lengths than were observed in the superheated Pb crystal at the same T . Furthermore, the layer adopted an ordered structure, $6 \times 6$ R6°, which indicates an in-plane hexagonal ordering of atoms that is slightly rotated with respect to the underlying Cu lattice [81]. Separate prior work examined later stage wetting for this system at $T = 700$ K; in that work, density profiles perpendicular to the solid/liquid interface demonstrated that the Pb(l) layer closest to the Cu(111) surface exhibited peak number density approximately four to five times the bulk Pb(l) density [41]. This was indicative of enhanced structural ordering for liquid atoms at the solid/liquid interface; thus, interfacial structure observed in Ref. [81] is to some degree stable for elevated T.

However, nothing was advanced about the structural order in the film at T = 700 K; in addition, interfacial structural analysis in that work was performed well after the relevant region of liquid had stopped spreading (i.e. for an essentially quiescent interface) [41]. Thus, it is of interest here to determine if interfacial structure is present in the liquid film when the contact line advances at its most rapid rate (i.e. early in the inertial regime). If such structure exists, does it show dependence upon rate of liquid slip past the solid surface?

From simulations here, density profile analysis perpendicular to the solid/liquid interface is performed but the region analyzed is restricted in x such that only material less than 2 nm from the advancing contact angle at $t = 0.2T^*$ is analyzed. This focused density analysis of the Pb(l) layer adjacent to the Cu(111) surface on that part of the layer moving at nearly the highest contact line velocity observed. Even for this rapidly moving layer, the peak density is approximately the same as is obtained for a quiescent interface at this T. Enhanced structural ordering in the layer associated with the observed density increase thus forms instantaneously when new solid/liquid interface is nucleated during inertial spreading. One difference, then, between rapidly slipping layers of liquid observed here and the bulk liquid is the former adopt increased in-plane structural ordering as indicated by a significant increase of in-plane density, relative to bulk liquid density.

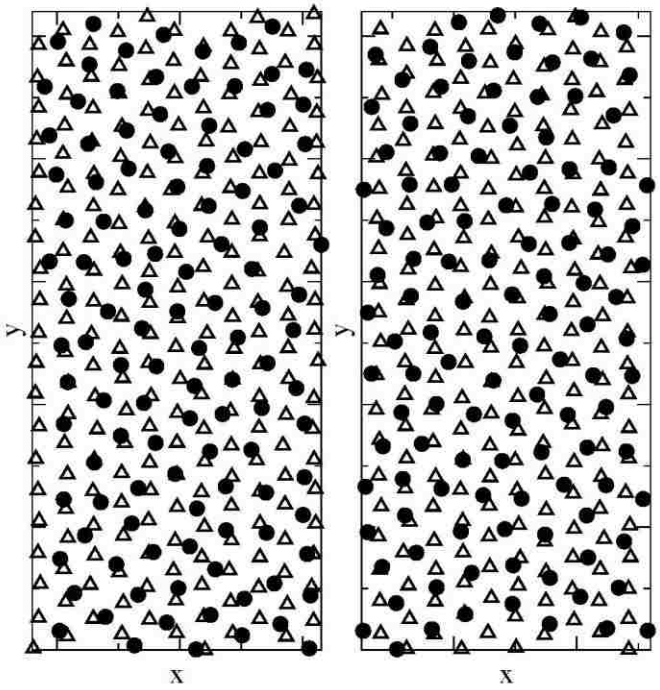


**Figure 5-6:** Atomic positions (circles) in the Pb(l) layer at the solid/liquid interface; each panel shows a span in x/y of 2.3 nm and 5.2 nm, respectively. Also shown are the positions that would be occupied for a layer in perfect epitaxy with the underlying crystal (triangles). The left panel shows data for $t = 0.5T^*$ and for a region of the layer farthest from the contact lines; the right panel shows data for $t = 0.2T^*$ and for a region of the layer that is between 1 nm and 3.3 nm from one of the advancing contact lines.

Figure 5-6 shows Pb atomic positions in the layer adjacent to the Cu(111) surface for the wetting geometry explored here. The dimensions shown in x and y for each panel are 2.3 nm and 5.2 nm, respectively. Also shown are the positions atoms would occupy if they were in perfect epitaxy with the underlying Cu lattice. The left panel shows atoms in the layer at $t = 5T^*$and for a region in the layer farthest from the contact line (i.e. at the point of initial solid/liquid contact); thus, the spreading velocity of atoms in this layer is zero and has been for multiple $T^*$. The right panel shows atoms in the layer at $t = 0.2T^*$ and for a region in the layer that is between 1 nm and

3.3 nm from the contact line; thus, the flow of atoms in this layer corresponds to a net velocity ~ 50 m/s (to the right in the image). Despite the very different kinetic state of these two groups of atoms, it is quite difficult to distinguish one from the other. In both, there appears to be a tendency toward hexagonal ordering; however, it is clearly defective in accord with T explored here. Because of this, other than the hexagonal tendency, there exists very little correspondence between Pb atom positions and perfect epitaxy; again, this appears the same for the two groups of atoms. To quantify this, the sum root mean squared distance between Pb(l) layer atomic positions and epitaxial positions is minimized for both layer regions shown in Figure 5-6; the results for the two groups of atoms differ by less than 3%. It thus appears there exists very little difference between the structure of the liquid film at the solid/liquid interface when the film is rapidly moving compared to when the film exhibits zero slip.

Atomic structure in the liquid film can be better analyzed by considering the probability distribution for atomic neighbor distances; this distribution (sometimes called g(r)) determines the likelihood that neighboring atoms are found at a distance r from a given atom in the film [68]. For example, for a crystalline material at finite T , all atoms experience a highly similar distribution of surrounding atoms; thus, all neighbor separation distances are well defined and the resulting g(r) exhibits well defined and discrete peaks. For liquids, atoms are randomly distributed, albeit typically with a well-defined nearest-neighbor separation distance; thus, the liquid state g(r) typically exhibits a well-defined first peak but, for larger r, the spectrum quickly loses evidence of peaks. For essentially 2D structures like the Pb(l) layer of atoms

explored here, an in-plane g(r) analysis can instead be performed to constrain structural analysis to only a single layer. Typically, when g(r) is computed, it is done so at equilibrium such that ensemble (i.e. time) averaging can be used to reduce statistical error in the calculation; however, for the systems explored here, it is of interest to obtain instantaneous measures of this property in order to probe layer structure at a given contact line advancement velocity. Recall that contact line velocity changes very rapidly during the earliest stages of inertial spreading, when velocities are the highest. Thus, in-plane g(r) were calculated here from single instants in time during simulations; while this increases statistical fluctuations in spectra so obtained, averaging over many atoms in any given region in the liquid film mitigates this.

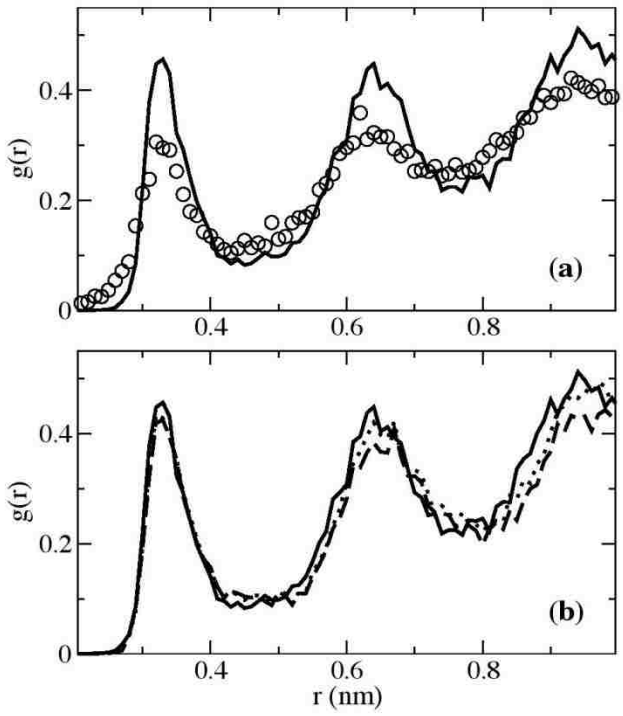


**Figure 5-7:** (a) In-plane g(r) data for a bulk liquid (circles) compared to g(r) data obtained instead from the Pb film nearest the solid/liquid interface (solid curve). Data for film atoms were obtained from a region of the film with zero spreading velocity and far from the contact line. (b) The same film

data from the top panel (i.e. far from the contact line, solid curve) are compared to in-plane g(r) data for film atoms that are between 1 nm and 3 nm from the contact line (dotted), and less than 1 nm from the contact line (dashed).

Figure 5-7(a) shows in-plane g(r) results obtained for an essentially quiescent liquid film as compared to the same analysis performed in a bulk liquid (i.e. from a simulation that employed 3D periodic boundary conditions). Liquid film data are obtained from the same group of atoms shown in the left panel of Figure 5-6. A similarly defined slab (i.e. 2.3 nm by 5.2 nm by 0.3 nm in x, y, and z, respectively) was used to gather data from the bulk liquid. Due to the significantly lower in-plane density in the bulk liquid, there are less atoms sampled and correspondingly increased statistical fluctuations. Nonetheless, data from both systems are fairly smooth and obvious differences exist between the two g(r) spectra. Despite calculation of an in-plane g(r), results for the bulk liquid are similar to what is obtained from a 3D calculation: there is a fairly well defined first peak followed by peaks with rapidly deteriorating definition; for separation distances larger than r = 1 nm, peaks are essentially absent in the bulk liquid spectrum.

Data for g(r) for liquid film atoms exhibit significantly enhanced structural definition, compared to bulk liquid: peaks are narrower and higher in magnitude, indicative of tighter bounds on observed atomic separation distances. However, data do not exhibit characteristics of a crystalline solid: peaks are broader than what is observed for crystals and greater peak overlap is seen in Figure 5-7(a), compared to g(r) for a typical crystalline structure. In-plane g(r) for liquid film atoms closest to the solid surface instead exhibit what is sometimes called medium range order, typical of an

amorphous solid, or glass. Coupled with observations of the solid/liquid interface at T = 625 K [81], observations here indicate there may exist a structural transition in the liquid film adjacent to the Cu(111) surface that is analogous to a glass transition. At minimum, this otherwise liquid layer of atoms possessing enhanced structural ordering is obviously stable across some range in T. Such an observation motivates consideration of recently advanced 'complexion' theory for describing ordered, atomically thick structures at solid/solid interfaces (i.e. grain boundaries) [88]. The notion of interfacially stabilized phases is not new [89]; however, recent experimental data supporting this notion have been advanced [90], [91]. Here, the relatively ordered layer of liquid atoms at the solid/liquid interface may represent a liquid phase complexion. Ordered liquid layers adjacent to solid surfaces have been observed for other systems both experimentally and via simulation [92]–[94]. Here, evidence is advanced that this ordered layer directly abets high slip velocity during inertial spreading.

To examine how in-plane structure depends on position in the liquid film or, more directly, slip velocity, data for the liquid film from Figure 5-7(a) are repeated in Figure 5-7(b) and compared to similar data obtained from a film during rapid slip. Specifically, in-plane g(r) is computed for the same group of atoms shown in the right panel of Figure 5-6. Note that, because this group of atoms was selected to be at least 1 nm away from the contact line, g(r) is computed out to 1 nm with equivalent neighbor statistics to what are obtained for atoms far from the contact line. If atoms closer to the contact line are sampled, their g(r) will necessarily probe the edge of the layer and thereby sample less neighbor statistics. Nonetheless, g(r) analysis is also performed on the

group of Pb(l) layer atoms that are less than 1 nm from the contact line at $t = 0.2T^*$ and the result is also shown in Figure 5-7(b). g(r) data for atoms at the quiescent solid/liquid interface differ only slightly from g(r) for atoms near the contact line. Data for all three groups of atoms analyzed show three peaks with similar peak definition. Peaks in g(r) calculated from the group of atoms closest to the contact line show a slight but characteristic increase in position. This is most obvious for peaks at larger r but a detectable increase occurs for the first peak as well. The same observations can be made for the group of atoms that are between 1 nm and 3.3 nm from the contact line, but to a lesser degree. There thus appears to exist a very slight in-plane expansion of atoms in the Pb(l) layer that are closest to the advancing contact line; this is reasonable given the significant capillary pressure acting on atoms in that region. Furthermore, there appears to exist a gradient in the strain induced in the layer such that atoms in the layer more than $\sim$ 4 nm from the contact line exhibit zero peak shift (i.e. zero strain); atoms increasingly closer to the contact line experience increasing in-plane tensile strain.

It is well accepted that atomic scale simulations are capable of revealing quantitative descriptions of liquid slip at solid surfaces [95]. However, results here indicate that in-plane strain in the layer of atoms directly adjacent to the solid surface and closest to the contact line may play a role in manifesting significant slip lengths during inertial wetting. Notions of structural order and strain certainly challenge the description of atoms in this region as liquid, particularly as incompressible fluid. It is likely necessary that a thorough description of thermodynamics and kinetics of such interface phases, what some call complexions for dopant phases at solid/solid interfaces

[88], will require enhanced theoretical understanding. What already seems clear is that interface structure, distinct from bulk liquid structure, plays a role in determining dynamical process rates during inertial wetting.

# 6 Self-pinning and Depinning of Nano-particle Suspension

Figure 6-1 shows time evolutions for spreading of $\phi = 0$ and $\phi = 8\%$ droplets on the Cu(001) surface; a similar comparison is given for spreading on the Cu(111) surface in Figure 6-2. To characterize wetting kinetics the extent of spread versus time (x(t)) is shown in Figure 6-3 for all systems studied; data were obtained from the edge of the drop, making certain to compute the edge position above the two-layer precursor film observed to form in these systems. Thus, kinetic data are indicative of droplet spreading and not precursor film advancement. For all cases explored herein, events at both contact lines for a given case were essentially identical; as such, $x(t)$ data for the two contact lines in each system were averaged to produce plots in Figure 6-3.

Spreading in the absence of suspended nano-particles is considered first. As has been previously observed for this system, it can be seen here that, during the earliest stages of spreading, $\theta_{adv}$~60° on Cu(111) was lower than $\theta_{adv}$~90° on Cu(001); furthermore, spreading kinetics for the lower $\theta_{adv}$ case were distinctly faster. It has been previously shown that this difference in contact line morphology manifests from the very onset of spreading in these two systems and that the decreased advancing contact angle

on Cu(111) stems from the propensity for rapid precursor film formation and advancement in this system [83]. Indeed, in Figure 6-2c for $\phi = 0$ the precursor film is already evident and has extended ~10 nm ahead of the droplet edge on Cu(111). As is commonly observed for low viscosity, high wettability liquids, wetting of Pb(l) on both Cu(001) and Cu(111) is initially characterized by an inertial wetting regime of very rapid spreading; this is followed by a slower spreading regime wherein dynamics are governed by viscous effects (hydrodynamic theory) and/or contact line phenomena (molecular-kinetic theory). It is during inertial wetting that different kinetics manifest on the different crystallographic surfaces. Contact line velocity following the inertial regime is similar for $\phi = 0$ drops on Cu(001) and Cu(111) [83]. For the $R_0 = 42$ nm drops studied here, the inertial/capillary time scale is $T \sim \sqrt{\rho R_0^3 / \gamma_{lg}} \sim 1.2$ ns, where $\rho$ is the liquid density; further, the inertial regime has been demonstrated to persist in time out to $\sim 2T$. Thus, images in Figure 6-1b and Figure 6-2b are from during inertial spreading while images in Figure 6-1c and Figure 6-2c are well after inertial spreading is complete.

Figure 6-1 and Figure 6-2 show that, for the earliest stages of spreading on both Cu(001) and Cu(111), there is little difference between the overall drop morphology for $\phi = 0$ versus $\phi = 8\%$ ($\theta_{adv}$ for $\phi = 8\%$ suspension droplets on both Cu(001) and Cu(111) were ~10° higher than observed for $\phi = 0$). Kinetic data in Figure 6-3further bear this out, showing that, for spreading on either Cu(001) or Cu(111), $x(t)$ is essentially independent of $\phi$ out to $t \sim 1$ ns for all $\phi$ studied here. For $\phi = 8\%$ cases on both Cu(001) and Cu(111), particles were entrained to both contact lines during early

stages of wetting. Flow rate to the advancing contact line at early time was sufficiently large in both cases to ensure particles were delivered there; as will be discussed below, this was also dependent on initial particle position in the drop. Focusing on the Cu(001) system in Figure 6-1, for $\phi = 8\%$, detachment occurred for both advancing contact lines sometime between $t$ = 1 ns and $t$ = 4 ns; in this case, no self-pinning was observed, despite the presence of entrained particles. In Figure 6-1c, the images at t = 4 ns for $\phi = 0$ and $\phi = 8\%$ on Cu(001) show that a small difference existed between the total extent of spread for the two systems, with the $\phi = 0$ case having advanced somewhat farther. Kinetic data if Figure 6-4 support this description; furthermore, the inflection in $x(t)$ for $\phi = 8\%$ that occurs over the time from $t = 1$ ns to $t = 3$ ns is indicative of de-pinning in this system. This will be described in greater detail below.

Examining results in Figure 6-2 for spreading on Cu(111), it can be seen that both advancing liquid fronts remained bound to particles for $\phi = 8\%$. Images at $t$ = 4 ns for $\phi = 0$ and $\phi = 8\%$ in Figure 6-2c show that, for $\phi = 0$, both contact lines advanced significantly farther than the pinned contact lines in the $\phi = 8\%$ case on Cu(111). This is corroborated by data in Figure 6-3 that shows $x(t)$ for $\phi = 8\%$ is flat after $t$ ~ 3 ns, illustrative of a pinned contact line. To emphasize pinning for the nanosuspension droplet on Cu(111), Figure 6-4a and Figure 6-4b compare the $\phi = 0$ case to the $\phi = 8\%$ case at t = 7 ns. In the absence of particles, the droplet continues to spread on Cu(111), albeit increasingly slowly as it approaches its equilibrium contact angle $\theta_0 = 20°$. However, for $\phi = 8\%$ on Cu(111), it can be seen that, once it becomes pinned, the contact line remains immobile throughout the remainder of the simulation. Considering a

cylindrical cap construction to the overall droplet morphology in the pinned case, the apparent pinned contact angle is $\theta_{pin} \sim 50°$. However, because of the self-pinning particle entrained to the contact line, it is important to more carefully examine structure near the contact line and this is discussed further below. Figure 6-4c shows the $\phi = 8\%$ case on Cu(001) at $t$ = 10 ns; though spreading on the Cu(001) surface is slower, this images bears out that the nanosuspension drop on Cu(001) eventually spreads to a greater extent than the pinned nanosuspension drop on Cu(111). Though the $\phi = 0$ case on Cu(001) is not shown in Figure 6-4, the small difference between spreading extent that existed after depinning persisted throughout the remainder of the simulations.

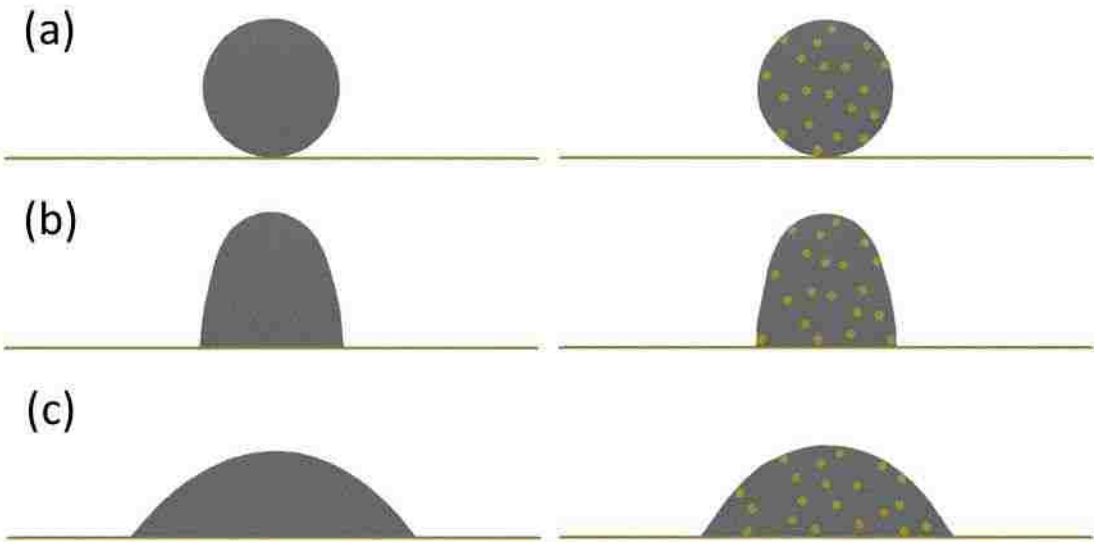


**Figure 6-1:** Comparison between simulations of (left) a pure Pb(l) drop ($\phi = 0$) and (right) a Pb(l) drop containing 20 particles ($\phi = 8\%$) wetting Cu(001) substrates: (a) $t = 0$; (b) $t = 1ns$; (c) $t = 4ns$. In all simulation renderings, light (dark) atoms are Pb (Cu) and only a portion of the substrate is shown; graphics are rendered using AtomEye [96].

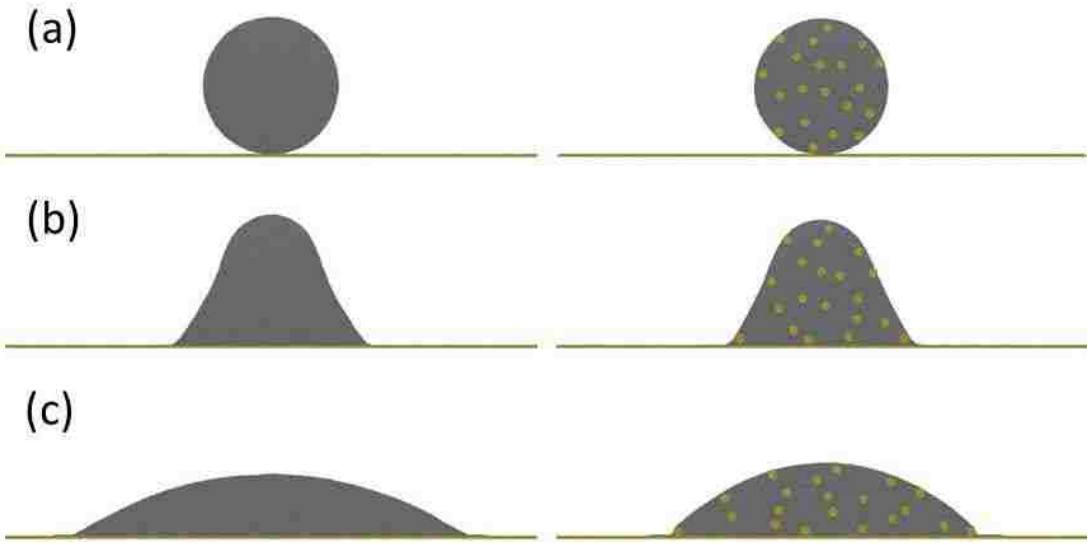


**Figure 6-2:** Comparison between simulations of (left) a pure Pb(l) drop ($\phi = 0$) and (right) a Pb(l) drop containing 20 particles ($\phi = 8\%$) wetting Cu(111) substrates: (a) $t = 0$; (b) $t = 1ns$; (c) $t = 4ns$.

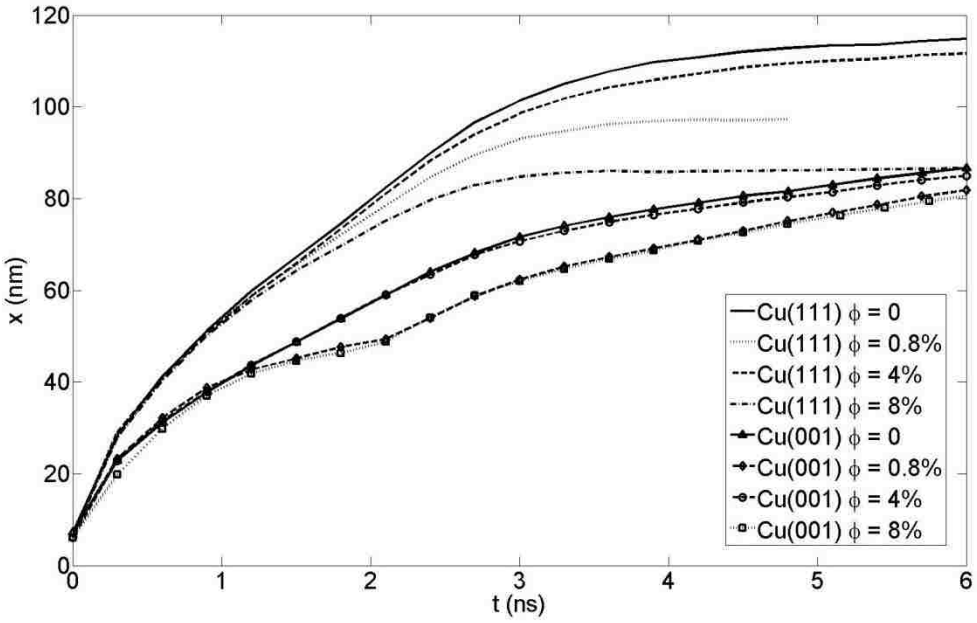


**Figure 6-3:** Extent of droplet spread in *x* versus time *t*. Data are presented for Pb droplets wetting Cu (001) and Cu(111) for varying particle loading: $\phi = 0,\ 0.8\%, 4\%,$ and $8\%$.

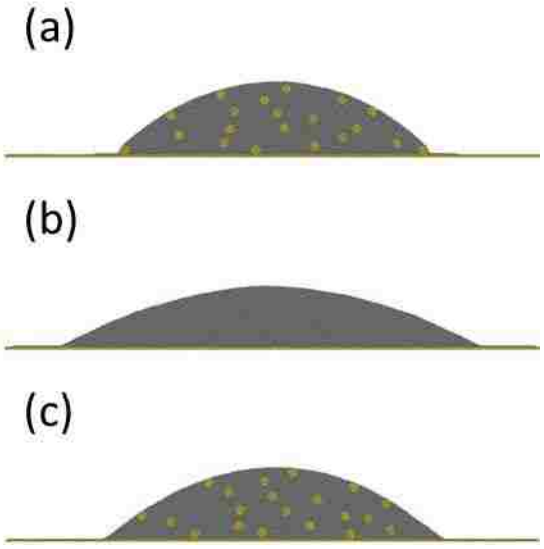


**Figure 6-4:** Simulation snapshots of systems at later times: (a) $\phi = 8\%$ droplet wetting Cu(111) ($t = 7ns$); (b) $\phi = 0$ droplet wetting Cu(111) ($t = 7ns$); (c) $\phi = 8\%$ droplet wetting Cu(001) ($t = 10ns$).

Figure 6-3 shows data for droplets with $\phi = 4\%$ wetting both Cu(001) and Cu(111); in those cases, due to the random positions selected upon inserting the particles, no particles were entrained to the advancing contact lines during spreading. Thus, $x(t)$ data for $\phi = 4\%$ on both Cu(001) and Cu(111) are very similar to what was observed for $\phi = 0$ on both of these surfaces. At later time after intertial spreading is complete, a small reduction in spreading kinetics can be observed for $\phi = 4\%$ compared to $\phi = 0$ on both Cu(001) and Cu(111); on Cu(001), this reduction is very small. Since this difference emerges as viscous dissipation becomes a more dominant driving force determining spreading kinetics, this indicates that particle inclusion at this low loading causes a small increase to the droplet's effective viscosity. Otherwise, particle inclusion

for $\phi = 4\%$ had little effect on spreading behavior because no particles were entrained into the advancing contact lines.

At particle loadings explored here, entrainment to the advancing contact line is a result of particles being in the correct region of the drop at time zero. To test this, simulations were repeated for wetting on both Cu(001) and Cu(111) but with only two particles inserted into each droplet ($\phi = 0.8\%$). The particles were inserted into the identical positions as those two particles that were entrained into the contact line for $\phi = 8\%$. Because of the symmetry in our simulations, two particle insertion represents the dilute limit of loading since there are no particle/particle interactions. As shown in Figure 6-3, results for the dilute limit on Cu(001) were essentially identical to what was observed for $\phi = 8\%$. The two particles inserted were again entrained into the contact line, began to slow the particle front around $t$ = 1 ns, and were subsequently left behind after the advancing liquid front detached from the entrained particles. On Cu(111) results for the dilute limit were the same in the sense that contact line pinning was observed like it was for the $\phi = 8\%$ case. However, during the latter half of inertial regime spreading, differences in spreading kinetics for $\phi = 0.8\%$ and $\phi = 8\%$ began to emerge with the dilute limit system spreading somewhat faster than the $\phi = 8\%$ system. This difference is again indicative of a greater effective viscosity for the higher loading system. Nonetheless, the primary result that pinning occurs on Cu(111) persists. The reason the difference is smaller between kinetics for the dilute limit and $\phi = 8\%$ on Cu(001) is because entrained particles in those systems attempt to pin the contact line earlier than on Cu(111); data in Figure 6-3 show that dramatic deceleration of the liquid front occurs

starting about half way through the inertial spreading regime on Cu(001). The de-pinning events dominate spreading kinetics from $t$ ~ 1 ns to $t$ ~ 3 ns; thus, viscous influences on spreading kinetics do not emerge until later in time. Indeed, at the latest time shown in Figure 6-3, spreading kinetics for the dilute limit droplet on Cu(001) are a very small amount faster than for the $\phi = 8\%$ droplet.

Other than repeating the two particle positions that led to entrainment for the $\phi = 8\%$ case, no further attempt was made to assess more rigorously the region in the drop where a particle can be inserted such that it will then be entrained into the contact line. By doing so, one could compute the corresponding volume (or area) fraction and use that to make arguments about the probability for particle entrainment to the contact line at varying loading levels. However, as loading increases, particle/particle interaction effects also become more pronounced such that more complex behavior should be expected. Further, given the treatment here of both wetting and pinning as effectively 2D processes, making quantitative connections between such an analysis and 3D spreading scenarios would be challenging. Thus, remaining focus here is on revealing more specifically behavior observed near the contact line for the pinning versus de-pinning cases.

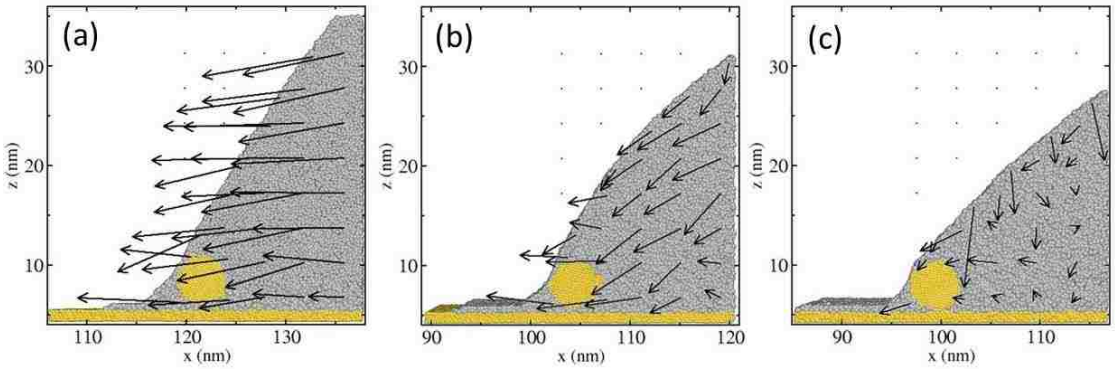


**Figure 6-5:** Contact line region images and fluid flow behavior for a pinning case on Cu(111). Data are shown at (a) $t = 1.5$ ns (early time of spreading), (b) $t = 2.5$ ns (right before pinning), and (c) $t = 3.2$ ns (when self-pinning is complete).

Figure 6-5 shows the contact line region for one of the advancing liquid fronts in a pinning case on Cu(111); as described in the procedure section, flow velocity plots have been created for the times shown and corresponding vectors are overlayed on the simulation snapshots. Though only one contact line is shown, events at the other three pinning contact lines were nearly identical to what is shown here. The largest velocity vector in Figure 6-5corresponds to $v$ = 79.08 m/s and all vectors are scaled accordingly. Significant spreading velocity exhibited on Cu(111) during inertial spreading is evident in Figure 6-5(a); it can further be seen that prior to pinning, a complete liquid film existed between the substrate and particle and this abetted the particle moving in concert with the liquid front. In Figure 6-5(b), an image is shown when the particle first began to experience interactions with the underlying substrate; because both particles and substrate were modeled as Cu, strong bonds could form between particle and substrate atoms. At

the later point in time shown in Figure 6-5(b), significant flow lateral to the substrate seen in Figure 6-5(a), has been replaced with more inclined flow that is oriented toward the contact line. Nonetheless, fairly fast flow velocities are still observed. Over the next 0.7 ns, flow velocities adjacent to the contact line are shown in Figure 6-5(c), to diminsh dramatically in accord with halting of the liquid front advancement. Careful examination of the particle/substrate interface shows that a sufficient number of Cu-Cu bonds have formed there to partially eliminate the liquid film between particle and substrate. This halts particle advancement, leading to contact line pinning.

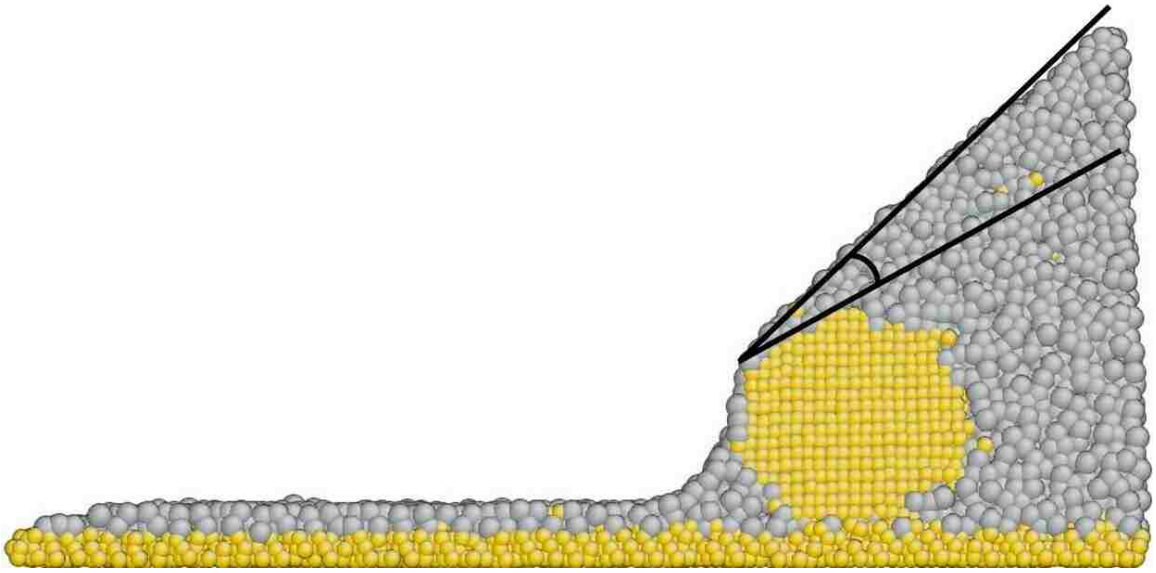

**Figure 6-6:** A plan view image of a magnified contact line region at late time ($t$ = 7 ns) for a pinning case on Cu(111).

Figure 6-6 shows a magnified image of the same contact line region shown in Figure 6-5 but for later in time. As was presented above, the apparent contact angle for

the $\phi = 8\%$ pinned cases is $\theta_{pin} \sim 50°$ (for the dilute limit case, the apparent contact angle at both contact lines was a little less $\theta_{pin} \sim 45°$). However, as shown in Figure 6-6, structure at the pinned contact line was more complex in that particle faceting manifested an inclined solid plane of atoms at the very edge of the liquid front. As indicated schematically in the figure, this implies that the contact angle of the liquid front on the particle is very near the equilibrium value for this system. Thus, the combination of a low advancing contact angle with faceted particles entrained into the contact lines means that, when the particles become bound to the underlying substrate, the liquid is able to adopt the equilibrium contact angle on the particle, reducing the local driving force for spreading to zero. The bilayer precursor film that has been previously studied for this wetting system is still observed in Figure 6-6 to advance across the Cu(111) surface. However, it can also be seen that, as liquid film atoms transport across one facet of the particle, they do so as a monolayer; thus, precursor film kinetics in pinned systems are significantly reduced from what is observed for droplets with no particles. One additional observation from Figure 6-6 is that, even at this later time, the interface between the particle and the underlying substrate is not pure Cu but instead contains some liquid atoms.

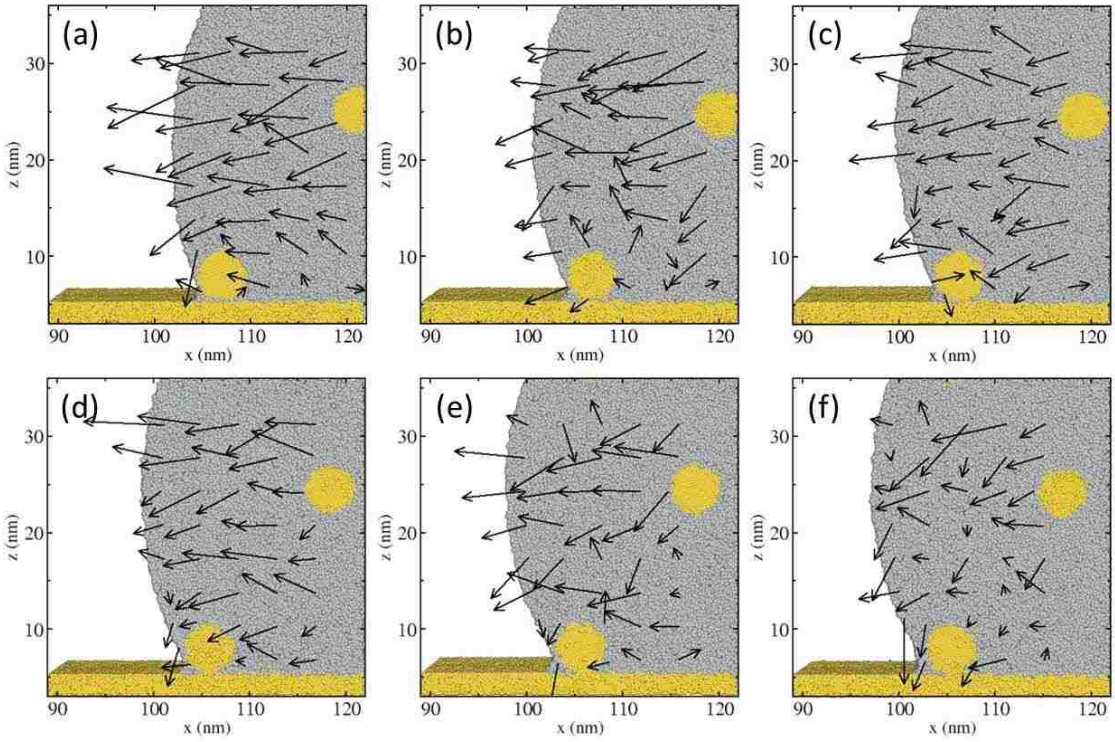


**Figure 6-7:** Contact line region images and fluid flow behavior for a de-pinning case on Cu(001). Images show the advancing liquid front as it starts detaching from the particle: (a) $t = 1.6$ ns, (b) $t = 1.7$ ns, (c) $t = 1.8$ ns, (d) $t = 1.9$ ns, (e) $t = 2.0$ ns, (f) $t = 2.1$ ns.

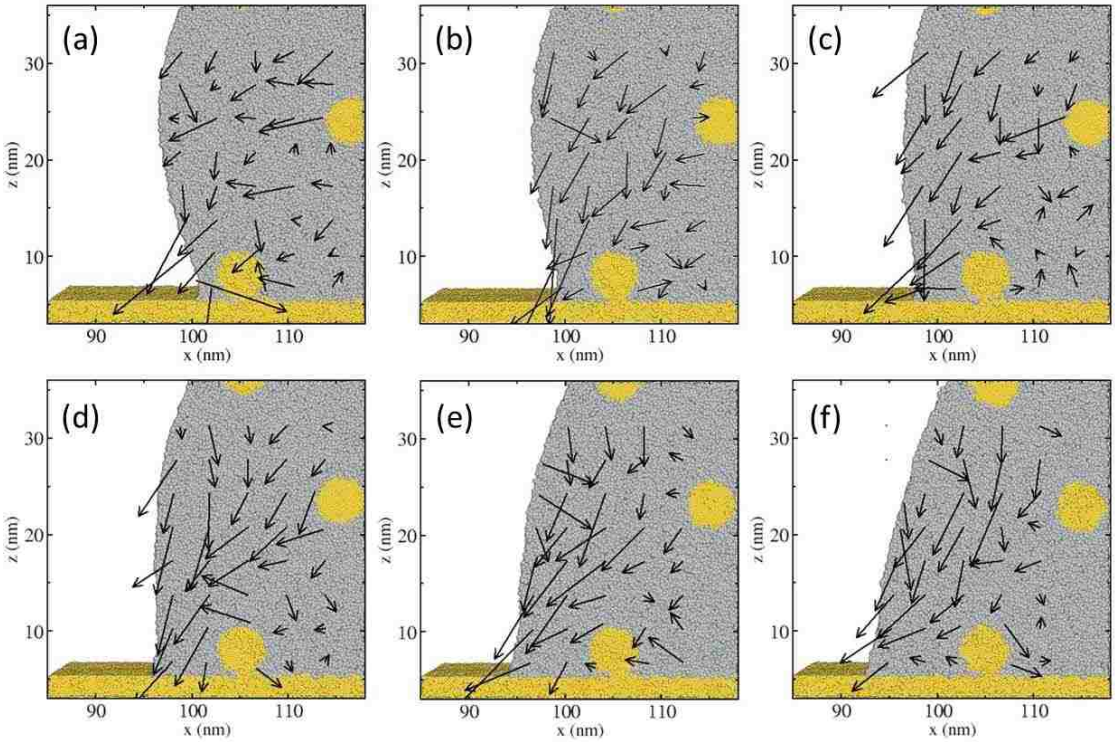


**Figure 6-8:** Data are continued from Figure 6-7 with images here showing when the advancing liquid front has detached from the particle and continued to spread forward: (a) $t = 2.2$ ns, (b) $t = 2.3$ ns, (c) $t = 2.4$ ns, (d) $t = 2.5$ ns, (e) $t = 2.6$ ns, (f) $t = 2.7$ ns.

Figure 6-7 and Figure 6-8 show similar data as to what were shown in Figure 6-5; however, now a de-pinning case on Cu(001) is explored. Again, behavior observed at the three other de-pinning contact lines were nearly identical to what is presented here. In Figure 6-7, contact line behavior leading up to the liquid front detaching from the particle is shown; for all but the last image in Figure 6-7, significant flow of liquid lateral to the substrate can be observed. During this time, the particle began forming bonds with the underlying substrate and becoming immobilized. As that happened, flow above the

particle caused the contact angle to increase; the largest apparent angle can be observed in Figure 6-7(e) and it is near $120°$; very shortly after this, as shown in Figure 6-7(f), the liquid front pulls free of the particle. Figure 6-8 shows that, after the liquid front detaches from the particle, the high contact angle drives very rapid advancement of the contact line across the surface; Figure 6-8(a) through Figure 6-8(d) correspond with the brief period of liquid front acceleration observed in Figure 6-3. Figure 6-8(e) shows the contact angle has again decreased below $90°$ and Figure 6-8(e) and Figure 6-8(f) correspond with the return to decreasing rate spreading kinetics observed for de-pinning systems at $t \geq 2.5$ ns in Figure 6-3.

In all cases explored here where particles were entrained into advancing contact lines, the ability for strong chemical bonds to form between particles and the substrate eventually emerged and, as this happened, particle advancement was halted. For wetting on Cu(111) the relatively low advancing contact angle in conjunction with faceting on the entrained particle made it so that, when the particle was halted by the underlying substrate, the liquid was able to adopt the equilibrium contact angle on the faceted particle surface. Since the particle and substrate were of identical chemistry, this is somewhat similar to pinning by a surface roughness feature. For wetting on Cu(001), the contact angle when the particle was halted by the underlying substrate was significantly higher than on Cu(111) such that flow opened up the contact angle further. When the apparent contact angle reached $\sim 120°$ binding between the liquid and the particle was sufficiently reduced for them to separate, leading to de-pinning. Notably, for all cases examined, particles bound to the underlying substrate did not form a clean interface with

the surface. The propensity for the liquid to form wetting layers on surfaces of this solid was emphasized by the intrusion of liquid into the interfaces between particles and substrates.

Liquid front behavior and associated flow observed adjacent to the particle during de-pinning in Figure 6-7 and Figure 6-8 indicate that non-trivial capillary and/or drag forces likely manifest on the particle. Regarding drag on the particle, an important finding was recently advanced for shear flow in a channel past suspended cylinders [97] using both analytical and simulation approaches. Authors of that work found that, when the cylinder was positioned directly adjacent to the channel wall, forces due to drag diminished significantly. Though our flow geometry is different here from the one studied in Ref. 35, sufficient similarity exists that we may expect drag forces to be small, despite the high flow rates observed in Figure 6-7 and Figure 6-8. This is because the cylindrical particles are attached to the substrate and, as described previously, proximity to the solid surface provides a shielding effect from drag forces.

Regarding capillary force on the particle, expressions advanced in prior studies for such forces involve the product of a relevant length scale (e.g. the pinning particle radius) and the liquid/vapor surface tension; there are typically also geometric factors accounting for contact angle and the shape of the particle [63]. If we simply consider $\gamma_{lg} = 0.574 \pm 0.038\, J/m^2$ for the $\phi = 0$ liquid here and multiply that by the particle radius, a force of order 1 nN is obtained. It could be argued that the relevant length scale here is the length of the particle along its cylindrical axis; in that case, the force is twice. While this coarse estimate does not account for contact angle, it provides an idea of the

upper bound expected for such forces on particle sizes considered here. Figure 6-3 permits an alternate interpretation in that one can instead consider the force on the liquid front necessary to cause the deceleration observed during de-pinning. Taking two numerical derivatives of kinetic data in Figure 6-3 gives contact line acceleration; comparing acceleration data for de-pinning cases to $\phi = 0$ cases allows extraction of the component of decelerating force associated with the capillary action of the entrained particles on the liquid front. To convert acceleration into force, however, some mass of liquid must be considered to be acted upon during de-pinning and this determination is not obvious. If the mass of liquid so considered is only comprised of those atoms in direct interaction with the particle, the peak capillary force so obtained is less than one-tenth of a nano-Newton (nN). This, though, does not seem physically correct when one considers the range of influence observed in the fluid, where flow velocity tens of nano-meters from the contact line is obviously retarded during de-pinning. If instead one heuristically asserts that 20% of droplet atoms are acted upon during contact line deceleration associated with capillary action, this corresponds to peak capillary force of order 1 nN, similar to force magnitudes discussed above.

To more directly assess forces manifesting during de-pinning, the collective force on the entrained particle shown in Figure 6-7 and Figure 6-8 was computed; furthermore, forces due to the surrounding liquid were distinguished from forces due to the underlying substrate. To better quantitatively assess such forces, the same calculations were done but for quiescent situations in which the average forces on the particle were zero. The situations considered were a Cu particle on a Cu substrate, a Cu particle immersed in a

Pb(l) at zero flow, and a Cu particle at an interface between a Cu substrate and Pb(l) but for zero flow geometry (see Figure 6-9). To compute force on the particle, all atomic forces on particle atoms were summed every 100 simulation steps to obtain a total force on the particle for that time sample. Again, forces due to liquid atoms were distinguished from those due to substrate atoms; furthermore, the *x* and *z* components of force were separately computed. To reduce fluctuations, 100 samples were averaged (taken over a consecutive 10000 simulation steps) to obtain a single value reported in force plots in Figure 6-9 and Figure 6-10. For the zero force situations explored in Figure 6-9, values obtained can indeed be seen to vary around zero; however, the largest fluctuations observed are of order 1 to 2 nN. If the analysis presented in Figure 6-9 is repeated but using 500 sample averaging (i.e. reporting force values computed over 50000 simulation steps), fluctuations are reduced to less than 0.5 nN. Thus, for dynamic wetting simulations, a challenge emerges to maintain high temporal resolution while using sufficient time averaging to reduce fluctuations observed. Given the magnitude of capillary force discussed in the preceding paragraph, fluctuations such as those observed in Figure 6-9 indicate it may be difficult to reveal capillary forces definitively from background noise.

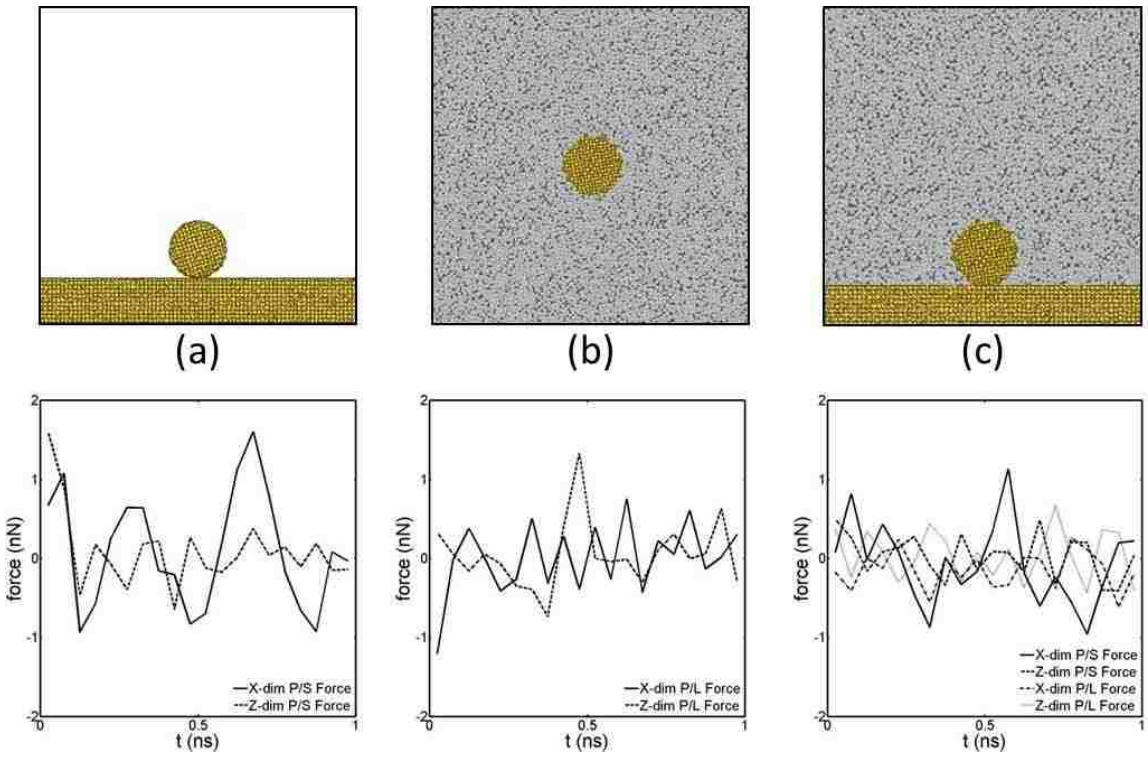


**Figure 6-9:** Force on a particle versus time for three zero force cases: (a) a Cu particle on a Cu substrate, (b) a Cu particle immersed in Pb(l) at zero flow, and (c) a Cu particle at a Cu(001)/Pb(l) interface for zero flow condition. Top images show simulation configurations; bottom images show force computed using 100 time sample averages (see text). In legends, P/S is particle/substrate and P/L is particle/liquid.

Using 100 time sample averaging, forces on the particle at the contact line shown in Figure 6-7 and Figure 6-8 were computed during the de-pinning event and results are shown in Figure 6-10. The x component forces due to both liquid and substrate remain near zero throughout the analysis, in agreement with drag forces due to liquid flow being relatively small. On the other hand, z component forces exhibited significant deviations from zero, starting at the same time that the droplet begins the de-pinning process. Near $t = 1.3$ ns, the liquid z-component force departed from zero such that the liquid had a net

effect of forcing the particle in a direction away from the substrate. Subsequently, for $t \geq 1.4$ ns, the solid z-component force departed from zero with a net effect of forcing the particle toward the substrate. Soon thereafter, for $t \geq 1.7$ ns, the solid and liquid can be seen to exert nearly equal and opposite z-component forces on the particle with magnitudes of order 10 nN and these forces persist after de-pinning is complete. These magnitude forces are clearly larger than fluctuations observed in Figure 6-9 so they are statistically significant; however, they are also larger than expected based on coarse estimates of capillary force.

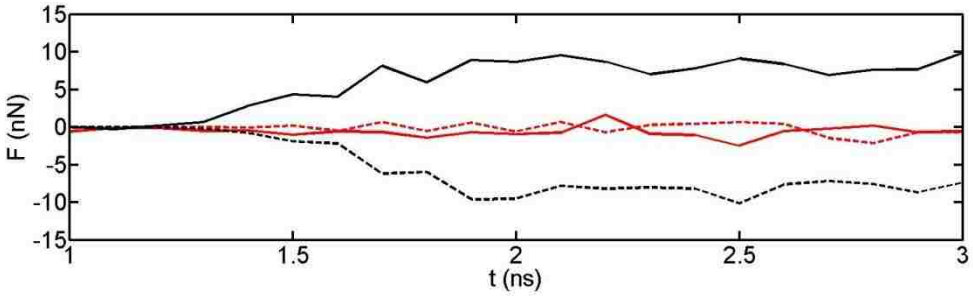


**Figure 6-10:** Force on the particle shown in Figure 6-7 and Figure 6-8. Force components in x (red) and z (black) are shown and force exerted on the particle by the liquid (solid curves) is distinguished from force exerted by the substrate (broken curves).

To understand forces computed on the particle during de-pinning, calculations to produce Figure 6-10 were repeated but only for the liquid force on the particle. Furthermore, the liquid contributions to force on the particle were distinguished based on geometric considerations. This is perhaps made more clearly by horizontal and vertical lines in images shown in Figure 6-11 and Figure 6-12. First, an even division of the

particle along the z direction was established such that one side could be considered closer to the de-pinning liquid front and the other side could be considered farther from the de-pinning front. Next an approximate division of the particle into thirds along the x direction was established such that one-third of particle atoms could be considered farthest from the substrate, one-third were intermediate distance from the substrate, and one-third were considered adjacent to the substrate. Again, the six regions so established are shown in Figure 6-11 and Figure 6-12. At the start of a 10000 step (100 sample) computation, liquid atoms were divided into groups based on which of the six geometric regions was occupied by a given atom. The force on the particle due to liquid atoms in each region was separately computed and is shown in Figure 6-11 and Figure 6-12 via vector plots. The largest force vector illustrated is 8.3 nN and all vectors are scaled using the same normalization.

As soon as bonds began forming between the particle and substrate, a relatively large force manifested on the region of the particle nearest to the substrate and closer to the detaching liquid front. Surprisingly, the large positive direction z-component force exerted on the particle by the liquid is primarily due to liquid atoms that become essentially trapped at the interface that forms between the particle and the substrate. As shown in Figure 6-10, the substrate pulls down on the particle as it attempts to form a clean Cu-Cu interface between particle and substrate. However, liquid atoms trapped at that interface push upward on the particle, producing most of the positive z-component force observed in Figure 6-10. For all images in Figure 6-11 and Figure 6-12, the force vector due to liquid in what can be thought of as the lower left region is the largest and it

possesses significant positive z-direction character. On the other hand, the force due to liquid in the lower right region, farther from the detaching front, is close to zero throughout the presented analysis. The reason for this is the bonded structure between the particle and the underlying substrate preferentially formed in the region farther from the advancing liquid front; this is apparent in the progression of images shown in Figure 6-11 and Figure 6-12. These observations demonstrate that, for the particle size explored here, forces manifesting on the particle during de-pinning (and afterwards) are dominated by interfacial effects. This is not a surprising result given the very small nano-particles modeled.

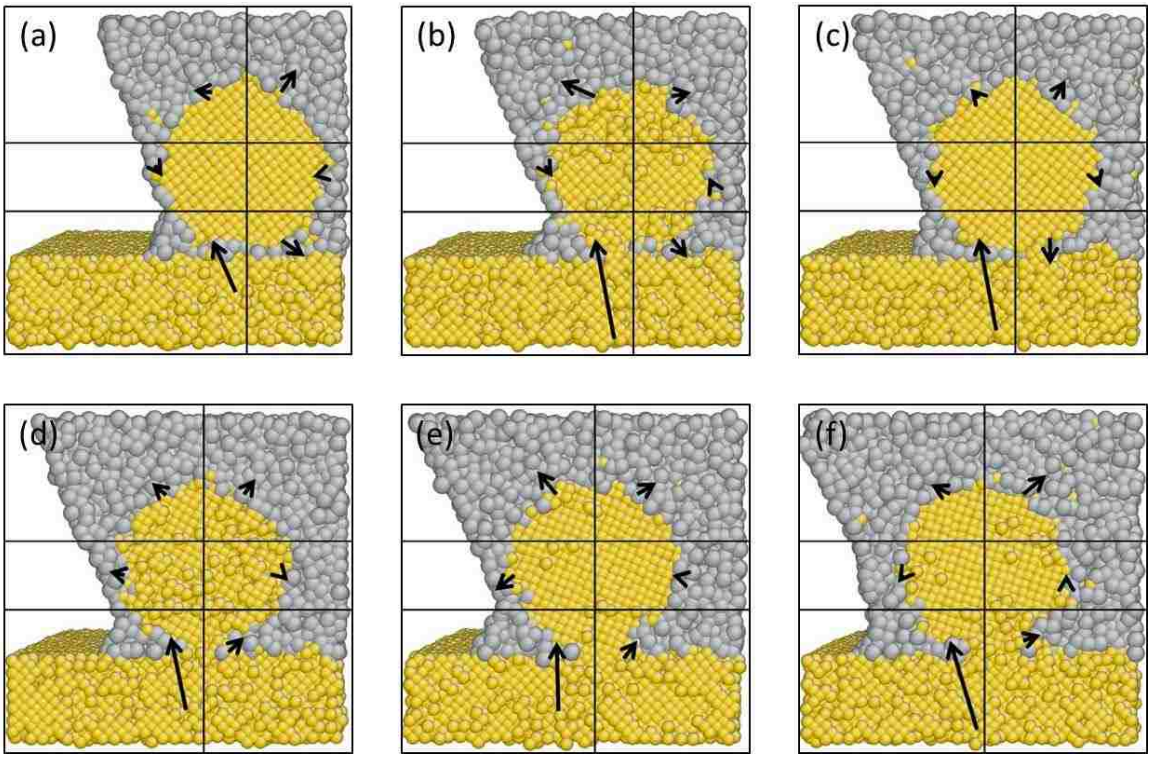


**Figure 6-11:** Force due to liquid atoms on the particle shown in Figure 6-7 (also for data in Figure 6-10). Force contributions are distinguished based on where in the system liquid atoms are located (as shown by horizontal and vertical dividing lines). The largest vector shown corresponds to 8.3 nN and all vectors are scaled the same. Times shown are the same as in Figure 6-7.

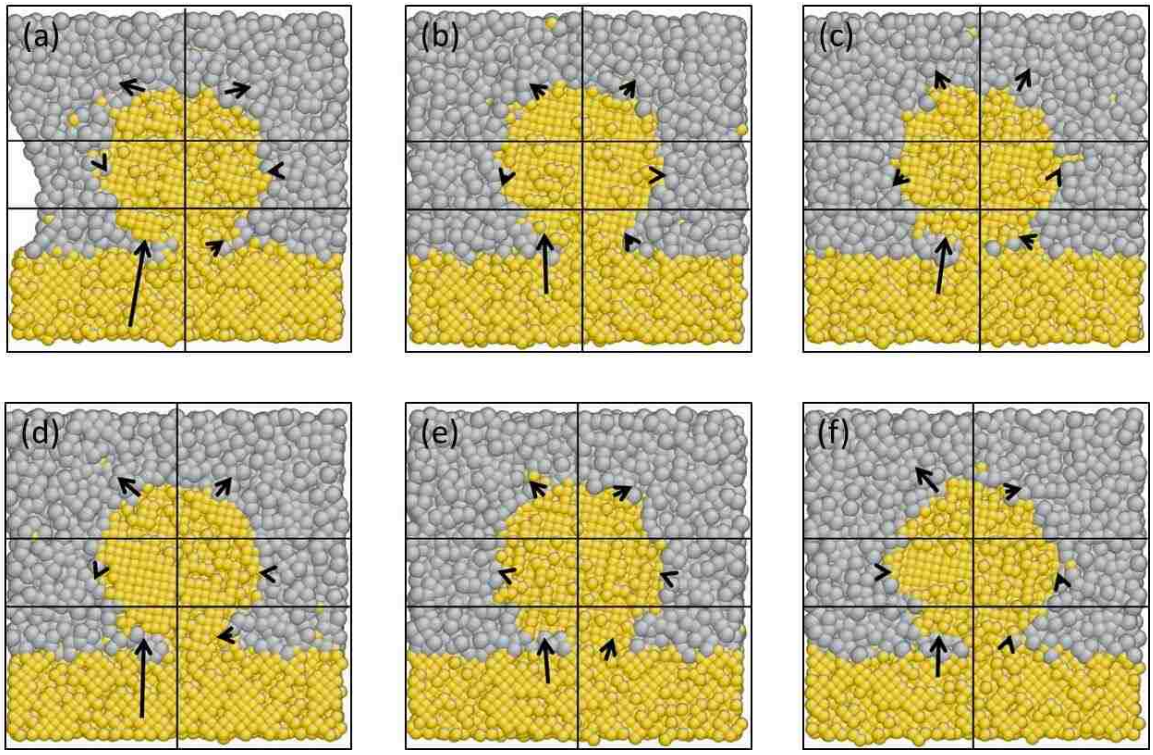


**Figure 6-12:** Force due to liquid atoms on the particle shown in Figure 6-8 (also for data in Figure 6-10). These images show a continuation from Figure 6-11; times shown are the same as in Figure 6-8.

Some remaining observations should be made about forces illustrated in Figure 6-11 and Figure 6-12. Though force on the particle is dominated by effects manifesting near the particle/substrate interface, forces due to liquid atoms in the region farthest from the substrate and closer to the advancing liquid front warrant some discussion. These are what can be called the upper left region forces and, in all images in Figure 6-11 and Figure 6-12, those force vectors exhibit a character indicative of lifting the particle away from the substrate and in the direction of liquid front advancement. Magnitudes observed are sufficiently small that drawing quantitative conclusions is not possible; nonetheless, it

qualitatively appears that those forces are reflective of either capillary or drag forces (or their combination). A similar argument can be made for forces due to liquid in the middle left region immediately prior to liquid front detachment from the particle. In Figure 6-11(d) and Figure 6-11(e), the force due to liquid in the middle left region is convincingly oriented in the direction of front detachment, which occurs between the times shown in Figure 6-11(e) and Figure 6-11(f). Though it is again not possible to make quantitative conclusions, these observations lend qualitative support that forces driving pinning and de-pinning can be directly computed in MD simulations. Furthermore, to suppress the dominance of interfacial effects such as observed here, larger particles should be studied.

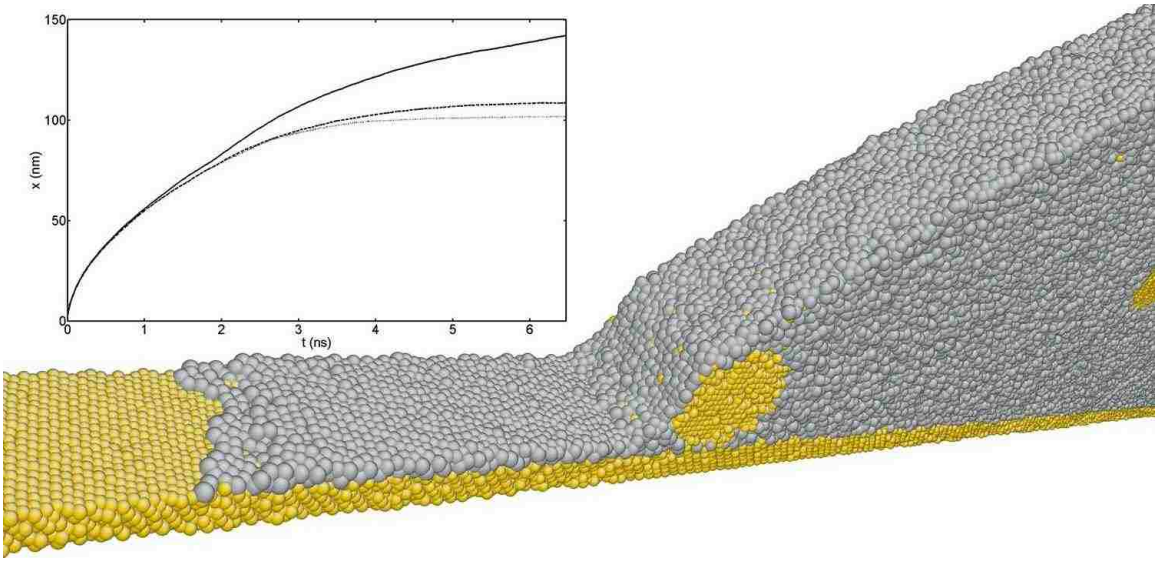


**Figure 6-13:** A close-up perspective view of the contact line region well after it self-pins (t=7 ns) for a $\emptyset$ ~ 8% droplet wetting Cu(111). The upper-left figure shows x versus t for precursor film layers spreading on Cu(111). Data are shown for a $\emptyset$ = 0 drop (solid), a $\emptyset$ ~ 8% drop with (001) particles (dot), and a $\emptyset$ ~ 8% drop with (111) particles (dash).

When simulations on the low $\theta_{adv}$ surface were repeated but with (111) particles suspended, the extent of droplet spread prior to pinning was somewhat larger (i.e. the

contact angle was somewhat lower) than for suspended (001) particles. The pinned (111) particle system is shown in the image inset to Figure 6-13. Because particle faceting was mixed on both particle types, the difference in wetting was small and best observed in $x(t)$ data for different systems. These data are also shown in Figure 6-13. where results are presented for three systems, $\emptyset = 0$, $\emptyset \sim 8\%$ with (111) particles, and $\emptyset \sim 8\%$ with (001) particles. For all three cases, data are shown for the precursor film (solid curves) and the bulk droplet (broken curves); note also that $x^2(t)$ is plotted versus t. During most of the inertial regime of spreading, very little difference existed in spreading kinetics and all six curves essentially overlap during this regime in Figure 6-13. In accord with a low viscosity and high wettability liquid, this system showed $x(t) \sim t^{1/2}$ during inertial spreading and the pre factor appeared constant across systems explored here. Near $t = 1.5$ns, differences emerged. The top two curves show data for $\emptyset = 0$ and it can be seen that a pre-cursor film advanced rapidly ahead of the drop after droplet spreading slowed; $t^{1/2}$ kinetics exhibited by the pre-cursor film at late time were distinct from kinetics exhibited during inertial regime spreading [83]. The bottom four curves are from suspension drops and both broken curves (for bulk droplet spreading) eventually flatten, showing that pinning occurred for both (001) and (111) particles. The upper broken curve is for (111) particles, demonstrating a somewhat greater degree of spread occurred in this system prior to pinning; this is in accord with a somewhat reduced contact angle on the pinning particle. Though the difference in total extent of spread is small, this is partly because facet inclination is also somewhat different for pinning particles in the (001) versus (111) particle cases. A close inspection of the pinning (111) particles shows the

angle between the liquid/vapor interface and the inclined facet was near to 20°, as expected.

Pinning greatly slowed pre-cursor film advance but did not halt it altogether. Figure 6-13 shows two solid curves for precursor film kinetic data in the $\emptyset \sim 8\%$ with (001) versus (111) particles. Like for bulk droplet spreading, the curve for the precursor film in the (111) particles case is above the (001) particles case, in accord with somewhat greater spread in the former system. Careful inspection of precursor film kinetic data for both pinned systems shows that the film continued to advance after pinning was complete. Kinetics are dramatically reduced and it is difficult to determine if $t^{1/2}$ behavior is still present. The main panel of Figure 6-13 shows a close-up of the region near the pinned contact line, well after pinning was complete. It can be seen that the precursor film is a bilayer, as was observed for this system previously [41]; however, as the precursor film advances over one facet of the pinning particle, it adopts a monolayer structure, partly explaining why precursor film advancement is so dramatically slowed. The monolayer structure may form because it is difficult to maintain a bilayer structure across the edge between two facets on the particle (i.e. an edge effect); alternatively, it could be driven by the crystallographic nature of the facet itself. Either way, this means that, for the edge of the precursor film to advance a given distance, effectively two times that distance worth of diffusion must occur for material in the monolayer film.

Results presented illustrate that, for a system with identical chemistry but varying $\theta_{adv}$ based on substrate crystallographic orientation, self-pinning occurs for low $\theta_{adv}$ but not for high $\theta_{adv}$. For high $\theta_{adv}$, an attempt to self-pin occurs but fails. Forces computed during both events show that liquid force on a pinned particle is well described via capillary effects; for the failed pinning (i.e. de-pinning) case, liquid force on particles at the contact line was predominantly due to flow into the contact line region as the contact angle increased. After the liquid front detached from the particle, flow continued as the front briefly accelerated and then resumed normal decelerating rate spreading kinetics. At late stages in the de-pinning case, forces on the particle returned to zero; alternatively, the pinning particle exhibited a state of tension with equal and opposite forces exerted by the liquid and the underlying substrate. In both cases, considerations typically invoked to interpret experimental data for macro scale suspension drops gave very good quantitative agreement with forces computed from atomic scale simulations of nanometer scale drops. The contact angle of the liquid on the particle was seen to influence the final pinned droplet morphology. Lastly, self-pinning dramatically slowed precursor film advancement because film transport across the pinning particles involved a stage where the film was forced to adopt a monolayer structure, rather than the bilayer structure exhibited on the planar substrate surface.

Previous work [97] and my computation of forces on liquid front indicate that those forces due to liquid flow are below resolution of force calculation. Further quiescent state force analysis illustrates our magnitude of capillary force fluctuations. Forces on the particle during de-pinning were computed and significant z direction force

was observed on the outermost particle which mainly came from the trapped Pb layer underneath. It was demonstrated that interfacial effects are dominated especially for the nano-scale particles cases. Recent work in the literature has shown the benefit of using atomic scale simulations to explore phenomena associated with both suspension droplet evaporation [58] as well as spreading [62]. Here, it is further demonstrated that such simulations can be used to directly compute forces on particles in such scenarios and connect those forces to observed behavior near the contact line. In advancing our knowledge on capillary forces on particles during depinning and pinning cases, future work will be emphasized on investigating the role of both particle loading (e.g. dilute limit case with no particle-particle interaction and high loading cases when particle-particle interactions become relevant) as well as how particle size affects spreading kinetics and how this connects to dynamic droplet morphology and relevant forces that exist nearby the contact line region.

Recent work in the literature has shown the benefit of using atomic scale simulations to explore phenomena associated with both suspension droplet evaporation [58] as well as spreading [62]. Here, it is further demonstrated that such simulations can be used to directly compute forces on particles in such scenarios and connect those forces to observed flow behavior. A power in simulations is the ability to alter, among other things, the underlying interactions so as to study the influence of thermodynamics in a controlled way. Future work will explore such effects and establish quantitative relations between the likelihood for pinning and underlying thermodynamics as represented in particle/liquid and particle/substrate interaction strength. The influence of particle size

will also be explored. Finally, to provide more meaningful information on the role of  in determining whether pinning occurs, spherical drops with spherical particles will be modeled.

# 7 Conclusion

The phenomenon of inertial spreading was studied here and further explored via atomic scale MD simulations. A counterintuitive result from both existing literature and results presented here is that, particularly for liquid metals, even nanometer scale drops accessible to atomic simulations exhibit a regime of wetting that is dictated by inertial effects. This implies that, for inertial wetting, mechanisms observed in atomic simulations may directly aid interpretation of observations on macroscale drops. Simulations presented here explored isothermal inertial regime spreading for nanometer scale Pb(l) droplets. To properly interpret observed data, it was necessary to account for nanoscale size effects on inertial spreading. Specifically, it was necessary to incorporate a Tolman length corrected surface tension to account for liquid/vapor interface curvature effects that manifest in small drops. In addition, for the very rapid inertial spreading observed on Cu(111), a second nanoscale effect was observed; it was unique to this surface and it was related to curvature gradients manifesting along a significant portion of the liquid/vapor interface, particularly for the smallest drops. After accounting for these effects, all results obtained were able to be interpreted in terms of inertial spreading theory developed from continuum fluid mechanics. This was true even for drops with radius of only a few nanometers. Furthermore, because the computed

Tolman length here is comparable to the precursor film thickness, it was possible to estimate a value of $R_0$ above which effects related to both of these length scales will be undetectable, $R_0 \geq 100\, nm$.

Another observation was that high contact line velocity (and associated high velocity of liquid slip past the solid surface) during inertial spreading are abetted by structural ordering of a liquid layer adjacent to the solid; tensile strain in this layer, most pronounced nearest to the contact line, may also play a role. In advancing these conclusions about the mechanisms of rapid contact line advancement, a question arises as to the generality of the observations for different solid/liquid combinations. The characteristic here that seemed to predominantly underpin observed behavior was the ordering of the liquid at the solid/liquid interface. Since ordering in liquid layers at solid/liquid interfaces has been observed for a number of different systems (e.g. oxide liquids, water, metal liquids), it is predicted that mechanisms observed here manifest in many other inertial spreading systems. However, an important caveat exists; it has been demonstrated previously that surface roughness can completely disrupt slip of the liquid near the solid, particularly when the roughness is on the same scale as the molecular structure of the liquid [36], [95]. Indeed, in Ref. [36], authors discuss that surface roughness can disrupt slip and the mechanism for doing so is likely related to disruption of order in liquid layers near the solid. Data presented here provide additional support for this notion.

# 8 REFERENCES


[1] P. G. De Gennes, “Wetting: Statics and Dynamics,” *Rev. Mod. Phys.*, 1985.

[2] D. Bonn, J. Eggers, J. Indekeu, and J. Meunier, “Wetting and spreading,” *Rev. Mod. Phys.*, vol. 81, no. 2, pp. 739–805, May 2009.

[3] J. F. Lancaster, *The metallurgy of welding, brazing and soldering*. New York: American Elsevier Pub. Co, 1965.

[4] R. Lofting, *Brazing and Soldering*. Ramsbury, United Kingdom: The Crowood Press Ltd, 2014.

[5] IAEA, “Thermophysical Properties of Materials for Nuclear Engineering: A Tutorial and Collection of Data,” *J. Chem. Inf. Model.*, vol. 53, p. 160, 1989.

[6] Nea, *Handbook on Lead-bismuth Eutectic Alloy and Lead Properties, Materials Compatibility, Thermal-hydraulics and Technologies*, no. 6195. 2007.

[7] V. P. Sobolev, P. Schuurmans, and G. Benamati, “Thermodynamic properties and equation of state of liquid lead and lead-bismuth eutectic,” *J. Nucl. Mater.*, vol. 376, no. 3, pp. 358–362, 2008.

[8] S. M. Foiles, M. I. Baskes, and M. S. Daw, “Embedded-atom-method functions for the fcc metals and their alloys,” *Phys. Rev. B*, 1986.

[9] J. H. Snoeijer and B. Andreotti, “Moving Contact Lines: Scales, Regimes, and

Dynamical Transitions," *Annu. Rev. Fluid Mech.*, vol. 45, no. 1, pp. 269–292, Jan. 2013.

[10] T. Young, "An essay on the cohesion of fluids," *Philos. Trans. R. Soc. London*, vol. 95, pp. 65–87, 1805.

[11] A.-L. Biance, C. Clanet, and D. Quéré, "First steps in the spreading of a liquid droplet.," *Phys. Rev. E. Stat. Nonlin. Soft Matter Phys.*, vol. 69, no. 1 Pt 2, p. 016301, Jan. 2004.

[12] J. Drelich and D. Chibowska, "Spreading kinetics of water drops on self-assembled monolayers of thiols: Significance of inertial effects," *Langmuir*, vol. 21, no. 17, pp. 7733–7738, 2005.

[13] J. C. Bird, S. Mandre, and H. a. Stone, "Short-time dynamics of partial wetting," *Phys. Rev. Lett.*, vol. 100, no. 23, p. 234501, Jun. 2008.

[14] J. Lopez, C. A. Miller, and E. Ruckenstein, "Spreading kinetics of liquid drops on solids," *Journal of Colloid and Interface Science*. 1976.

[15] E. B. Webb and G. S. Grest, "Molecular dynamics simulations of reactive wetting," *Scr. Mater.*, vol. 47, no. 6, pp. 393–398, 2002.

[16] A. Carlson, M. Do-Quang, and G. Amberg, "Modeling of dynamic wetting far from equilibrium," *Physics of Fluids*, vol. 21, no. 12. pp. 1–4, 2009.

[17] a. Carlson, M. Do-Quang, and G. Amberg, "Dissipation in rapid dynamic wetting," *J. Fluid Mech.*, vol. 682, pp. 213–240, 2011.

[18] K. G. Winkels, J. H. Weijs, A. Eddi, and J. H. Snoeijer, "Initial spreading of low-viscosity drops on partially wetting surfaces," *Phys. Rev. E - Stat. Nonlinear, Soft*

*Matter Phys.*, vol. 85, no. 5, p. 055301, May 2012.

[19] D. Legendre and M. Maglio, "Numerical simulation of spreading drops," *Colloids Surfaces A Physicochem. Eng. Asp.*, vol. 432, pp. 29–37, 2013.

[20] C. Huh and L. E. Scriven, "Hydrodynamic model of steady movement of a solid/liquid/fluid contact line," *J. Colloid Interface Sci.*, vol. 35, no. 1, pp. 85–101, 1971.

[21] O. V. Voinov, "Hydrodynamics of wetting," *Fluid Dyn.*, vol. 11, no. 5, pp. 714–721, 1976.

[22] L. H. Tanner, "The spreading of silicone oil drops on horizontal surfaces," *J. Phys. D. Appl. Phys.*, vol. 12, no. 9, pp. 1473–1484, 2001.

[23] E. B. Webb, G. S. Grest, D. R. Heine, and J. J. Hoyt, "Dissolutive wetting of Ag on Cu: A molecular dynamics simulation study," *Acta Mater.*, vol. 53, no. 11, pp. 3163–3177, 2005.

[24] E. Saiz, A. P. Tomsia, N. Rauch, C. Scheu, M. Ruehle, M. Benhassine, D. Seveno, J. De Coninck, and S. Lopez-Esteban, "Nonreactive spreading at high temperature: Molten metals and oxides on molybdenum," *Phys. Rev. E - Stat. Nonlinear, Soft Matter Phys.*, vol. 76, no. 4, 2007.

[25] T. J. Singler, S. Su, L. Yin, and B. T. Murray, "Modeling and experiments in dissolutive wetting: A review," in *Journal of Materials Science*, 2012, vol. 47, no. 24, pp. 8261–8274.

[26] L. Chen, E. Bonaccurso, and M. E. R. Shanahan, "Inertial to viscoelastic transition in early drop spreading on soft surfaces," *Langmuir*, vol. 29, no. 6, pp. 1893–1898,

2013.

[27] L. Courbin, J. C. Bird, M. Reyssat, and H. A. Stone, “Dynamics of wetting: from inertial spreading to viscous imbibition.,” *J. Phys. Condens. Matter*, vol. 21, no. 46, pp. 1–13, 2009.

[28] D. Qu é r é, H. Search, C. Journals, A. Contact, M. Iopscience, and I. P. Address, “Inertial capillarity,” *EPL (Europhysics Lett.*, vol. 39, no. 5, pp. 533–538, 1997.

[29] a. Carlson, G. Bellani, and G. Amberg, “Contact line dissipation in short-time dynamic wetting,” *EPL (Europhysics Letters)*, vol. 97, no. 4. p. 44004, 01-Feb-2012.

[30] A. Carlson, G. Bellani, and G. Amberg, “Universality in dynamic wetting dominated by contact-line friction,” *Phys. Rev. E - Stat. Nonlinear, Soft Matter Phys.*, vol. 85, no. 4, 2012.

[31] L. Chen, C. Li, N. F. A. Van Der Vegt, G. K. Auernhammer, and E. Bonaccurso, “Initial electrospreading of aqueous electrolyte drops,” *Phys. Rev. Lett.*, vol. 110, no. 2, 2013.

[32] a. Eddi, K. G. Winkels, and J. H. Snoeijer, “Short time dynamics of viscous drop spreading,” *Phys. Fluids*, vol. 25, no. 1, p. 013102, 2013.

[33] H. Ding and P. D. M. Spelt, “Inertial effects in droplet spreading: a comparison between diffuse-interface and level-set simulations,” *J. Fluid Mech.*, vol. 576, p. 287, 2007.

[34] C. Wu, T. Qian, and P. Sheng, “Droplet spreading driven by van der Waals force: a molecular dynamics study.,” *J. Phys. Condens. Matter*, vol. 22, no. 32, p. 325101,

2010.

[35] W. Ren and W. E, “Boundary conditions for the moving contact line problem,” *Phys. Fluids*, vol. 19, no. 2, p. 22101, 2007.

[36] Y. Nakamura, A. Carlson, G. Amberg, and J. Shiomi, “Dynamic wetting at the nanoscale,” *Phys. Rev. E - Stat. Nonlinear, Soft Matter Phys.*, vol. 88, no. 3, 2013.

[37] J. X. Yang, J. Koplik, and J. R. Banavar, “Molecular dynamics of drop spreading on a solid surface,” *Phys. Rev. Lett.*, vol. 67, no. 25, pp. 3539–3542, 1991.

[38] J. R. B. J. De Coninck, U. D’Ortona, J. Koplik, “Terraced Spreading of Chain Molecules via Molecular Dynamics,” *Phys. Rev. Lett.*, vol. 74, pp. 928–931, 1995.

[39] S. Bekink, S. Karaborni, G. Verbist, and K. Esselink, “Simulating the Spreading of a Drop in the Terraced Wetting Regime,” *Phys. Rev. Lett.*, vol. 76, pp. 3766–3769, 1996.

[40] P. van Remoortere, J. E. Mertz, L. E. Scriven, and H. T. Davis, “Wetting behavior of a Lennard-Jones system,” *J. Chem. Phys.*, vol. 110, no. 5, p. 2621, 1999.

[41] E. B. Webb, G. S. Grest, and D. R. Heine, “Precursor film controlled wetting of Pb on Cu.,” *Phys. Rev. Lett.*, vol. 91, no. 23, p. 236102, Dec. 2003.

[42] F. Heslot, N. Fraysse, and a. M. Cazabat, “Molecular layering in the spreading of wetting liquid drops,” *Nature*, vol. 338, no. 6217, pp. 640–642, 1989.

[43] F. Heslot, A. M. Cazabat, and P. Levinson, “Dynamics of wetting of tiny drops: Ellipsometric study of the late stages of spreading,” *Phys. Rev. Lett.*, vol. 62, no. 11, pp. 1286–1289, 1989.

[44] J. Moon, J. Lowekamp, P. Wynblatt, Stephen Garoff, and R. M. Suter, “Effects of

concentration dependent diffusivity on the growth of precursing films of Pb on Cu(1 1 1)," *Surf. Sci.*, vol. 488, no. 1–2, pp. 73–82, 2001.

[45] J. Eggers, J. R. Lister, and H. A. Stone, "Coalescence of Liquid Drops," *J. Fluid Mech.*, vol. 401, pp. 293–310, 1999.

[46] D. Quéré, "Fluid dynamics: impact on Everest.," *Nature*, vol. 435, no. June, pp. 1168–1169, 2005.

[47] A. Stein and R. C. Schroden, "Colloidal crystal templating of three-dimensionally ordered macroporous solids: Materials for photonics and beyond," *Curr. Opin. Solid State Mater. Sci.*, vol. 5, no. 6, pp. 553–564, 2001.

[48] S. Maenosono, T. Okubo, and Y. Yamaguchi, "Overview of nanoparticle array formation by wet coating," *Journal of Nanoparticle Research*, vol. 5, no. 1–2. pp. 5–15, 2003.

[49] L. Zhang, S. Maheshwari, H. C. Chang, and Y. Zhu, "Evaporative self-assembly from complex DNA-colloid suspensions," *Langmuir*, vol. 24, no. 8, pp. 3911–3917, 2008.

[50] J. Tang and E. H. Sargent, "Infrared colloidal quantum dots for photovoltaics: Fundamentals and recent progress," *Adv. Mater.*, vol. 23, no. 1, pp. 12–29, 2011.

[51] R. D. Deegan, O. Bakajin, T. F. Dupont, G. Huber, S. R. Nagel, and T. A. Witten, "Capillary flow as the cause of ring stains from dried liquid drops," *Nature*, vol. 389, no. 6653, pp. 827–829, 1997.

[52] R. Deegan, "Pattern formation in drying drops," *Phys. Rev. E*, vol. 61, no. 1, pp. 475–485, 2000.

[53] R. D. Deegan, O. Bakajin, T. F. Dupont, G. Huber, S. R. Nagel, and T. A. Witten, "Contact line deposits in an evaporating drop," *Phys. Rev. E - Stat. Physics, Plasmas, Fluids, Relat. Interdiscip. Top.*, vol. 62, no. 1 B, pp. 756–765, 2000.

[54] T. P. Bigioni, X.-M. Lin, T. T. Nguyen, E. I. Corwin, T. a Witten, and H. M. Jaeger, "Kinetically driven self assembly of highly ordered nanoparticle monolayers.," *Nat. Mater.*, vol. 5, no. 4, pp. 265–270, 2006.

[55] A.-M. Cazabat and G. Guéna, "Evaporation of macroscopic sessile droplets," *Soft Matter*, vol. 6, no. 12, p. 2591, 2010.

[56] H. S. Kim, S. S. Park, and F. Hagelberg, "Computational approach to drying a nanoparticle-suspended liquid droplet," *J. Nanoparticle Res.*, vol. 13, no. 1, pp. 59–68, Aug. 2011.

[57] K. L. Maki and S. Kumar, "Fast evaporation of spreading droplets of colloidal suspensions," *Langmuir*, vol. 27, no. 18, pp. 11347–11363, 2011.

[58] W. Chen, J. Koplik, and I. Kretzschmar, "Molecular dynamics simulations of the evaporation of particle-laden droplets," *Phys. Rev. E - Stat. Nonlinear, Soft Matter Phys.*, vol. 87, no. 5, p. 052404, May 2013.

[59] N. I. Lebovka, S. Khrapatiy, R. Melnyk, and M. Vygornitskii, "Effects of hydrodynamic retardation and interparticle interactions on the self-assembly in a drying droplet containing suspended solid particles," *Phys. Rev. E - Stat. Physics, Plasmas, Fluids, Relat. Interdiscip. Top.*, vol. 89, no. 052307, 2014.

[60] L. Zhang, Y. Nguyen, and W. Chen, "'Coffee ring' formation dynamics on molecularly smooth substrates with varying receding contact angles," *Colloids*

*Surfaces A Physicochem. Eng. Asp.*, vol. 449, no. 1, pp. 42–50, 2014.

[61] D. T. Wasan and A. D. Nikolov, "Spreading of nanofluids on solids.," *Nature*, vol. 423, no. 6936, pp. 156–159, 2003.

[62] G. Lu, H. Hu, Y. Duan, and Y. Sun, "Wetting kinetics of water nano-droplet containing non-surfactant nanoparticles: A molecular dynamics study," *Appl. Phys. Lett.*, vol. 103, no. 25, p. 253104, 2013.

[63] B. M. Weon and J. H. Je, "Self-pinning by colloids confined at a contact line," *Phys. Rev. Lett.*, vol. 110, no. 2, p. 028303, Jan. 2013.

[64] V. H. Chhasatia and Y. Sun, "Interaction of bi-dispersed particles with contact line in an evaporating colloidal drop," *Soft Matter*, vol. 7, no. 21, pp. 10135–10143, 2011.

[65] G. Lu, Y. Y. Duan, and X. D. Wang, "Surface tension, viscosity, and rheology of water-based nanofluids: a microscopic interpretation on the molecular level," *J. Nanoparticle Res.*, vol. 16, no. 9, 2014.

[66] S. Cheng and G. S. Grest, "Molecular dynamics simulations of evaporation-induced nanoparticle assembly," *J. Chem. Phys.*, vol. 138, no. 6, p. 064701, Feb. 2013.

[67] H. Goldstein, *Classical Mechanics*, vol. 278, no. September. 1980.

[68] M. P. Allen and D. J. Tildesley, "Computer Simulation of," *Liq. Oxford Univ. Press. New York*, vol. 18, no. 195, p. 385, 1987.

[69] E. S. Severin and D. J. Tildesley, "A methane molecule adsorbed on a graphite surface," *Mol. Phys.*, vol. 41, no. 6, pp. 1401–1418, 1980.

[70] L. Verlet, “Computer ‘experiments’ on classical fluids. I. Thermodynamical properties of Lennard-Jones molecules,” *Phys. Rev.*, vol. 159, no. 1, pp. 98–103, 1967.

[71] W. L. Jorgensen and J. TiradoRives, “Monte Carlo vs molecular dynamics for conformational sampling,” *J. Phys. Chem.*, vol. 100, no. 96, pp. 14508–14513, 1996.

[72] D. Frenkel and B. Smit, *Understanding molecular simulation: from algorithms to applications*, vol. New York,. 2002.

[73] C. W. Hirt and B. D. Nichols, “Volume of fluid (VOF) method for the dynamics of free boundaries,” *J. Comput. Phys.*, vol. 39, no. 1, pp. 201–225, 1981.

[74] W. E. Johnson, “Development and Application of Computer Programs Related to Hypervelocity Impact,” *Syst. Sci. Softw.*, vol. SSS-R-353, 1970.

[75] H.S. Lim, C.K. Ong, and F. Ercolessi, “Stability of face-centered cubic and icosahedral lead clusters,” *Surf. Sci.*, vol. 269–270, no. C, pp. 1109–1115, 1992.

[76] J. J. Hoyt, J. W. Garvin, E. B. Webb, and M. Asta, “An embedded atom method interatomic potential for the Cu Pb system,” *Modelling and Simulation in Materials Science and Engineering*. 2003.

[77] H. C. W. G. L. J. Bailey, “Surface tensions in the system solid copper-molten lead,” *Proc. Phys. Soc. London B*, vol. 63, pp. 350–358, 1950.

[78] C. Nagl, E. Platzgummer, O. Haller, M. Schmid, and P. Varga, “Surface alloying and superstructures of Pb on Cu(100),” *Surf. Sci.*, vol. 331–333, no. PART A, pp. 831–837, 1995.

[79] R. Plass, J. a Last, N. C. Bartelt, and G. L. Kellogg, "Nanostructures. Self-assembled domain patterns.," *Nature*, vol. 412, no. 6850, p. 875, 2001.

[80] S. Plimpton, "Fast Parallel Algorithms for Short-Range Molecular Dynamics," *J. Comput. Phys.*, vol. 117, no. 1, pp. 1–19, 1995.

[81] J. P. Palafox-Hernandez, B. B. Laird, and M. Asta, "Atomistic characterization of the Cu-Pb solid-liquid interface," *Acta Mater.*, vol. 59, no. 8, pp. 3137–3144, 2011.

[82] J. S. Rowlinson and B. Widom, *Molecular theory of capillarity*. New York: Oxford University Press, 1982.

[83] E. B. Webb and B. Shi, "Early stage spreading: Mechanisms of rapid contact line advance," *Current Opinion in Colloid and Interface Science*, vol. 19, no. 4. pp. 255–265, 2014.

[84] L. Rayleigh, "On the Capillary Phenomena of Jets," *Proc. R. Soc. London*, vol. 29, no. 196–199, pp. 71–97, 1879.

[85] R. C. Tolman, "The Effect of Droplet Size on Surface Tension," *J. Chem. Phys.*, 1949.

[86] I. a. Cosden and J. R. Lukes, "Effect of Cutoff Radius on the Surface Tension of Nanoscale Bubbles," *Journal of Heat Transfer*, vol. 133, no. 10. p. 101501, 2011.

[87] L. Chen, G. K. Auernhammer, and E. Bonaccurso, "Short time wetting dynamics on soft surfaces," *Soft Matter*, vol. 7, no. 19, p. 9084, 2011.

[88] M. P. Harmer, "The Phase Behavior of Interfaces," *Science (80-. ).*, vol. 332, no. 6026, pp. 182–183, 2011.

[89] J. W. Cahn, "Critical point wetting," *J. Chem. Phys.*, vol. 66, no. 8, p. 3667, 1977.

[90] M. Baram, D. Chatain, and W. D. Kaplan, “Nanometer-Thick Equilibrium Films: The Interface Between Thermodynamics and Atomistics,” *Science (80-. ).*, vol. 332, no. 6026, pp. 206–209, 2011.

[91] J. Luo, “Stabilization of Nanoscale Quasi-Liquid Interfacial Films in Inorganic Materials: A Review and Critical Assessment,” *Crit. Rev. Solid State Mater. Sci.*, vol. 32, no. October, pp. 67–109, 2007.

[92] S. H. Oh, Y. Kauffmann, C. Scheu, W. D. Kaplan, and M. Rühle, “Ordered liquid aluminum at the interface with sapphire.,” *Science*, vol. 310, no. 5748, pp. 661–663, 2005.

[93] M. Dijkstra, “Capillary freezing or complete wetting of hard spheres in a planar hard slit?,” *Phys. Rev. Lett.*, vol. 93, no. 10, 2004.

[94] B. B. Laird and R. L. Davidchack, “Wall-induced prefreezing in hard spheres: A thermodynamic perspective,” *J. Phys. Chem. C*, vol. 111, no. 43, pp. 15952–15956, 2007.

[95] N. V. PRIEZJEV and S. M. TROIAN, “Influence of periodic wall roughness on the slip behaviour at liquid/solid interfaces: molecular-scale simulations versus continuum predictions,” *J. Fluid Mech.*, vol. 554, no. -1, p. 25, 2006.

[96] J. Li, “AtomEye: an efficient atomistic configuration viewer,” *Model. Simul. Mater. Sci. Eng.*, vol. 11, no. 2, pp. 173–177, 2003.

[97] R. Cardinaels and H. A. Stone, “Lubrication analysis of interacting rigid cylindrical particles in confined shear flow,” *Phys. Fluids*, vol. 27, no. 7, 2015.

# Vita

I was born in Tianjin, a coastal city in the northeast of China in April, 1987. My father Haitao works in an ocean shipping agency and my mother Guizhen is a doctor. I'm the only child in my family.

I got my bachelor's degree in engineering mechanics at Tianjin University in 2009.

In order to pursue my research goal, I came to Lehigh University in 2009 for my PhD study in the Department of Mechanical Engineering under the supervision of Dr. Edmund Webb. My research focuses on computational modeling and simulations, especially for investigating the capillary fluid flow phenomenon by performing Molecular Dynamics Simulations on HPC super-computing resources here at Lehigh.

Meanwhile, during my study here, I have been fortunate to be a teaching assistant. I have supervised undergraduate and graduate students' homework, projects, essays, and exams in different subjects, including Solid Mechanics Lab, Engineering Vibration and Numerical Methods in Mechanical Engineering.